UNIVERSIDADE FEDERAL DE SANTA CATARINA
PROGRAMA DE PÓS-GRADUAÇÃO EM ENGENHARIA MECÂNICA

GUILHERME BEZ BATTI HÜBBE

ANÁLISE NUMÉRICA E EXPERIMENTAL DE UM AEROFÓLIO DE ALTA SUSTENTAÇÃO EM BAIXOS NÚMEROS DE REYNOLDS

Florianópolis
2017

Guilherme Bez Batti Hübbe

NUMERICAL AND EXPERIMENTAL ANALYSIS OF A HIGH LIFTING AIRFOIL AT LOW REYNOLDS NUMBER FLOWS

A thesis submitted to the faculty of the Federal University of Santa Catarina in partial fulfillment of the requirements for the degree of Master in Mechanical Engineering.
Advisor: Prof. Amir Antônio Martins de Oliveira Jr., Ph.D.

Florianópolis
2017

Ficha de identificação da obra elaborada pelo autor,
através do Programa de Geração Automática da Biblioteca Universitária da UFSC.

Hübbe, Guilherme Bez Batti
NUMERICAL AND EXPERIMENTAL ANALYSIS OF A HIGH LIFTING AIRFOIL AT LOW REYNOLDS NUMBER FLOWS / Guilherme Bez Batti Hübbe ; orientador, Amir Antônio Martins de Oliveira Jr., 2017.
172 p.

Dissertação (mestrado) - Universidade Federal de Santa Catarina, Centro Tecnológico, Programa de Pós Graduação em Engenharia Mecânica, Florianópolis, 2017.

Inclui referências.

1. Engenharia Mecânica. 2. Perfil S1223. 3. perfil de alta sustentação. 4. Asa em baixo número de Reynolds. 5. Aerodinâmica. I. Oliveira Jr., Amir Antônio Martins. II. Universidade Federal de Santa Catarina. Programa de Pós-Graduação em Engenharia Mecânica. III. Título.

Guilherme Bez Batti Hübbe

NUMERICAL AND EXPERIMENTAL ANALYSIS OF A HIGH LIFTING AIRFOIL AT LOW REYNOLDS NUMBER FLOWS

Esta Dissertação foi julgada adequada para obtenção do Título de "Mestre em Engenharia Mecânica" e aprovada em sua forma final pelo Programa de Pós-Graduação em Engenharia Mecânica.

Florianópolis, 30 de Junho de 2017.

_____

Prof. Jonny Carlos da Silva, Dr.
Coordenador do Curso

_____

Prof. Amir Antônio Martins de Oliveira Jr., Ph.D. – Orientador
Universidade Federal de Santa Catarina

Banca Examinadora:

_____

Prof. Amir Antônio Martins de Oliveira Jr., Ph.D. – Orientador
Universidade Federal de Santa Catarina

_____

Prof. César José Deschamps, Ph.D.
Universidade Federal de Santa Catarina

_____

Prof. José Antônio Bellini da Cunha Neto, Dr.
Universidade Federal de Santa Catarina

_____

Prof. Juan Pablo de Lima Costa Salazar, Ph.D.
Universidade Federal de Santa Catarina

Prof. Saulo Güths, Dr.
Universidade Federal de Santa Catarina

Dedication
To my family and friends

AKNOWLEDGEMENTS

I would like to thank my family and girlfriend for all the effort and love they have put in me.

I would like to express my gratitude to my advisor Professor Amir who has always been a constant source of encouragement and inspiration. Without his invaluable suggestions and ideas, this work would never have taken shape.

I also thank everyone who has contributed to this work, including Pedro and Thiago, PET members who initiated the development of the wing tunnel model used in this work.

RESUMO

A análise e desenvolvimento de perfis aerodinâmicos para operação em baixas velocidades têm ganhado importância recentemente devido à crescente utilização de VANTs (Veículos Aéreos Não Tripulados) e turbinas eólicas. Nessas aplicações, o número de Reynolds característico para o escoamento sobre a asa pode ser inferior a $3 \cdot 10^5$ e o escoamento pode sofrer separação na região laminar da camada limite, formando o que se conhece por bolhas de separação laminar. O principal objetivo deste trabalho é avaliar o comportamento das bolhas de separação laminar em um perfil aerodinâmico de alta sustentação por meio de simulações numéricas suportadas por medições em túnel de vento. Inicialmente, apresenta-se uma comparação entre os resultados previstos por quatro modelos de turbulência, sendo dois para escoamentos totalmente turbulentos (Spalart-Allmaras e SST k-ω), e dois para escoamentos de transição (γ-Re_θ e k-k_L-ω), usando o software FLUENT. Os modelos foram aplicados a um perfil Eppler 387, que foi escolhido por apresentar dados experimentais disponíveis e medidos em diferentes laboratórios, e a um perfil Selig 1223, por ser um perfil de alta sustentação e utilizado em aeronaves de baixa velocidade. Os resultados indicaram que, embora seja possível prever a evolução do coeficiente de sustentação para baixos ângulos de ataque usando qualquer um dos modelos, apenas os modelos de transição foram capazes de prever o surgimento da bolha de separação laminar, resultando em grandes diferenças no coeficiente de sustentação próximo ao ângulo de estol. Essas diferenças se tornaram particularmente relevantes para o perfil Selig 1223, que apresentou um ganho na sustentação máxima de 20 % movendo do Reynolds de $1 \cdot 10^5$ para $2 \cdot 10^5$. Em relação ao coeficiente de arrasto, os modelos de transição apresentaram uma diferença média de 10 % em relação às referências, enquanto que nos outros, essa diferença chegou a 40 % em alguns ângulos. Na sequência do trabalho, fabricou-se um perfil Selig 1223 instrumentado com tomadas de pressão em sua superfície, para medição do coeficiente de pressão ao longo de sua corda. Para visualizar o local da bolha de separação laminar, foi utilizado um óleo pigmentado. Os resultados mostraram boa concordância na previsão do coeficiente de pressão utilizando os modelos de transição e a observação com filme de óleo comprovou a posição e extensão da bolha de separação. Concluiu-se que a separação do escoamento na camada limite laminar foi a principal causa de estol no número de Reynolds de $1 \cdot 10^5$. Finalmente, estudou-se a possibilidade de eliminação da separação em regime laminar através da adição de um tubo de carbono à frente do bordo de ataque.

Experimentalmente, verificou-se que, com a aplicação dessa técnica, o ângulo de estol em número de Reynolds de $1 \cdot 10^5$ aumentou de 10° para 20°. A técnica da visualização com óleo mostrou que a bolha é eliminada com o emprego do gerador de turbulência. Os modelos de transição forneceram boa comparação com as medições, sendo recomendado o seu uso nessas aplicações.

Palavras-chave: Perfil S1223, perfil de alta sustentação, asa em baixo número de Reynolds, aerodinâmica.

ABSTRACT

The development and analysis of airfoils for low-speed operations have recently become important because of their vast use in UAVs (Unmanned Aerial Vehicle) and wind turbines. In these applications, the characteristic Reynolds number for the flow over the wing may be as low as $3 \cdot 10^5$ and separation may occur in the laminar region of the boundary layer, forming the so-called laminar separation bubbles (LSB). The main objective of this work is to evaluate the behavior of the LSBs in a high lifting airfoil by means of numerical simulations supported by measurements in wind tunnel. Primarily, a comparison of four turbulence models is given: two for fully-turbulent flows (Spalart-Allmaras e SST k-ω), and two for transitional flows (γ-Re_θ e k-k_L-ω), using FLUENT software. The models were initially used in an Eppler 387 airfoil, which was chosen due to the availability of experimental data obtained in different laboratories, and then in a Selig 1223, because it is a high lifting airfoil and used in low-speed aircrafts. Results indicated that, although it is possible to predict the development of the lift coefficient for low angles of attack using anyone of the models, only the transition-sensitive models were capable of predicting the LSBs, which resulted in large differences of the lift coefficient close to the region of stall. These differences became relevant for the S1223 airfoil, which presented a maximum lift coefficient difference of 20 % when comparing the Reynolds number cases of $1 \cdot 10^5$ and $2 \cdot 10^5$. Regarding drag coefficient in comparison to the references, transition-sensitive models showed an average difference of 10 %. Fully-turbulent models achieved maximum difference of 40 %. Following the work, a Selig 1223 wing was manufactured with pressure tapping holes on the surface to measure the pressure coefficient over it chord. In order to visualize the location of the laminar separation bubble, a pigmented oil was used. Results reported good agreement in predicting the pressure coefficient using the transition-sensitive models and the observations with oil film proved the position and extension of the LSBs. It was concluded that the separation in the laminar boundary layer was the main cause of stall in the Reynolds number of $1 \cdot 10^5$. Finally, it was considered the possibility of suppressing the laminar separation by installing a carbon fiber tube in front of the leading edge. Experimentally, it was verified that this technique provided an increase in the angle of stall from 10° to 20° at a Reynold number of $1 \cdot 10^5$. The oil visualization technique showed that the bubble is suppressed with the use of the turbulence generator. Altogether, transition-sensitive models provided results in better agreement with the experimental data. Their use is recommended in these applications.

Keywords: S1223 airfoil, high-lift airfoil, low Reynolds number wing, aerodynamics.

LIST OF FIGURES

LIST OF TABLES

LIST OF ABREVIATIONS

CAD	Computer Aided Design
CFD	Computational Fluid Dynamics
CNC	Computer Numerical Control
DNS	Direct Numerical Simulation
FVM	Finite Volume Method
LDV	Laser Doppler Velocimetry
LES	Large-Eddy Simulation
LS	Laminar Separation
LSB	Laminar Separation Bubble
LTPT	Langley's Low Turbulence Pressure Tunnel
MDF	Medium-Density Fiberboard
NACA	National Advisory Committee for Aeronautics
NASA	National Aeronautics and Space Administration
PIV	Particle Image Velocimetry
RANS	Reynolds-Averaged Navier-Stokes
SIMPLE	Semi-Implicit Method for Pressure Linked Equations
SST	Shear Stress Transport
TR	Turbulent Reattachment
UAV	Unmanned Aerial Vehicle
UIUC	University of Illinois Urbana-Champaign
VFD	Variable Frequency Drive

LIST OF SIMBOLS

Latin Alphabet

A_s	[m^2]	Test section area
c	[m]	Airfoil chord
(C_l/C_d)		Aerodynamic efficiency
C_d		Section drag coefficient
$C_{d,min}$		Minimum drag coefficient
$C_{d,u}$		Uncorrected drag coefficient
C_l		Section lift coefficient
$C_{l,max}$		Maximum lift coefficient
$C_{l,u}$		Uncorrected lift coefficient
C_m		Section moment coefficient
$C_{m,u}$		Uncorrected moment coefficient
C_f		Skin friction coefficient
C_p		Pressure coefficient
D	[N]	Drag force
D'	[N/m]	Drag force per unit span
$\overline{\overline{D}}$		Rate of strain tensor
D_{ij}		Rate of strain components
E		Empirical constant
f	[N/kg]	Body forces per unit mass acting on fluid particle
F_1	[N]	Force on strain gauge V1
F_2	[N]	Force on strain gauge V2
F_3	[N]	Force on strain gauge V3
h	[m]	Wind tunnel section height
K_{sb}		Solid blockage correction factor
K_1, K_2, K_3	[N/V]	Strain gauges calibration coefficients
L	[N/V]	Lift force
L'	[N/V]	Lift force per unit span
M'	[N·m/m]	Moment per unit span
Ma		Mach number
p	[Pa]	Pressure

p_∞	[Pa]	Pressure of the free stream
q_r	[kg/m·s^2]	Real dynamic pressure
q_t	[kg/m·s^2]	Theoretical dynamic pressure
q_∞	[kg/m·s^2]	Dynamic pressure
Re		Reynolds number
Re_u		Uncorrected Reynolds number
$\bar{\bar{T}}$		Stress tensor
$\vec{u}$	[m/s]	Velocity vector
u_i	[m/s]	Velocity component for the i direction
$\bar{u}_i$	[m/s]	Mean velocity component for the i direction
u_i'	[m/s]	Fluctuating velocity com for the i direction
u_t	[m/s]	Shear velocity
u^+		Dimensionless velocity
V	[m/s]	Air speed
V_a	[m/s]	Speed of sound
V_u	[m/s]	Uncorrected velocity
V_∞	[m/s]	Freestream velocity
y^+		Dimensionless distance

Greek Alphabet

α	[degree]	Angle of attack
α_0	[degree^{-1}]	Lift slope
$\alpha_{c_{l,max}}$	[degree]	Angle of attack at maximum lift
α_u	[degree]	Uncorrected angle of attack
Γ		Diffusion coefficient
$\Delta\alpha_{c_{l,max}}$	[degree]	Increase in angle of attack at maximum lift
$\Delta\alpha_{sc}$	[degree]	Variation of α (Streamline curvature correction)
$\Delta c_{d.min}$		Increase in minimum drag coefficient
$\Delta c_{l.max}$		Increase in maximum lift coefficient
$\Delta c_{l,sc}$		Variation of c_l (Streamline curvature correction)
$\Delta V1$	[V]	Voltage variation in gauge V1
$\Delta V2$	[V]	Voltage variation in gauge V2
$\Delta V3$	[V]	Voltage variation in gauge V3

ε_{sb}		Solid blockage coefficient
ε_{wb}		Wake blockage coefficient
κ		Empirical constant
λ	[Pa·s]	Volumetric Viscosity
μ	[Pa·s]	Viscosity of the fluid
μ_t	[m/s]	Turbulent viscosity
ρ	[kg/m^3]	Mass density of air
ρ_∞	[kg/m^3]	Freestream air density
σ		Correction constant
τ	[Pa]	Shear stress
τ_{ij}	[Pa]	Shear stress for the coordinates x_i and x_j
τ_w	[Pa]	Shear stress at wall
ϕ		Any scalar quantity

TABLE OF CONTENTS

1 INTRODUCTION

1.1 Motivation

During the last few years, unmanned aerial vehicles (UAVs) have become important in both civilian and military applications (SELIG *et al.*, 1995). The aerodynamics of these aircraft is characterized by the presence of low-speed airflows over the wings and control surfaces.

Typical values of air speed relative to the surface can vary from 0 to 20 m/s. The Reynolds number based on the chord length, i.e., the distance connecting the leading and trailing edges of the wing, typically varies from $1 \cdot 10^5$ to $3 \cdot 10^5$, being the last a common value for the cruise speed of a UAV. This flow regime on an airfoil is denominated as low-Reynolds number flow. In contrast to that, it can be noted that for commercial aircrafts, such as the Boeing 737-800, the Reynolds number can reach $3 \cdot 10^7$. The same scenario is common for the blades of horizontal and vertical axis wind turbines. While lift supports the aircraft weight, in the case of an UAV, it generates a torque on an axis, in the case of a wind turbine. The design of quiet and efficient wind turbines is strongly coupled to the adequate prediction of their aerodynamic characteristics.

Due to the applications mentioned above, much attention has been paid to low-Reynolds number flows over airfoils. In aircrafts flying in this regime, the flow on the leading edge and in a relevant part of the wing is laminar. The presence of adverse pressure gradient can lead to the separation of the laminar boundary layer. When separation is observed, transition occurs in the free-shear layer and the so-called laminar separation bubble (LSB) is formed when the turbulent flow reattaches the airfoil surface downstream of the transition (MAYLE, 1991; SELIG, 2003). This phenomenon induces an increase in body drag and an eventual decrease in lift. In some situations, the cyclical bubble formation and detachment may induce pressure pulses and consequent vibration and loss of stability. The use of turbulators, acoustic excitation or vibration excitation is shown to render airfoils free of LSBs (RICCI; MONTELPARE, 2005). However, the design of such structures is based on the understanding and ability of prediction of the formation and elimination of the LSB.

Much has been analyzed in this subject, using both numerical and experimental methods. Numerical simulations using CFD (Computational Fluid Dynamics) have the advantage of delivering results quickly.

In order to obtain accurate results, however, one should know how to select the adequate numerical model, especially when boundary layer transition is present.

Nowadays, modelling of turbulent flows is seen as an open field in engineering. Although there are methods that solve all turbulence scales accurately, named Direct Numerical Simulation, or DNS (SCHUMANN, 1974), (COLEMAN; SANDBERG, 2010), their high computational cost inhibits their use in industrial applications. Techniques that provide a not so high level of detail, but still capture the significant part of the turbulent flow, named Large Eddy Simulations, or LES, are also available (PIOMELLI, 1999), (SILVA FREIRE, *et al.*, 1998). However, in the great majority of industrial cases, the engineer's interest is focused in averaged values (for head loss, heat transfer rate, drag, lift, etc.) obtained quickly (limited by the computational power available). Thus, Reynolds-Averaged Navier-Stokes, or RANS, methods become a suitable choice and are widely used on different engineering fields, where relatively fast and low-cost predictions are required.

Many studies regarding turbulence modelling using RANS are available, but many of them are based on the assumption that the flow is fully-turbulent over the entire domain. However, even in flows that reach solid surfaces initially turbulent, there may be spots over the surface where the flow laminarizes over distances beyond what one would expect for the thickness of the viscous sublayer. This is the case of external flows such as the one shown in Figure 1.1, where a laminar boundary layer develops, even in a considerably high freestream turbulent environment, on the surface. This laminar region may be negligible in many cases, i.e., the length of the laminar region on the surface is much smaller than that of the turbulent region, but in others, it can be quite significant. In this second case, the use of classical turbulence models results in errors while predicting the mean variables of interest. Hence, the development of RANS turbulence models that accounts for laminar-to-turbulent transition still has great importance in many research fields.

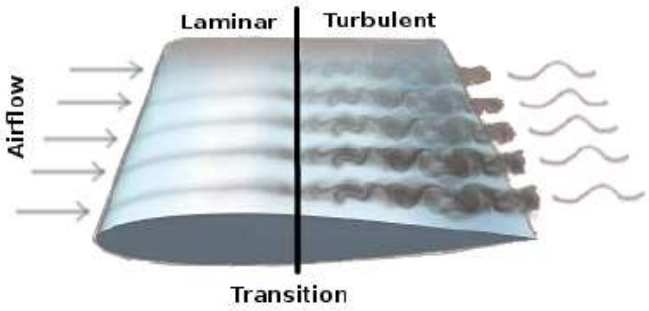

Figure 1.1 – Laminar and turbulent flow over a wing. (LOUREIRO *et al.*, 2015)

Regarding the experimental analysis, commonly performed in wind tunnels, it is known that the flow affected by the tunnel walls. The presence of the walls increases the measured lift, drag and pitching moment because of the increase in velocity at the model (BARLOW, *et al.*, 1999). Selig and McGranaham (2004) presented correlations to correct the measured quantities (angle of attack, aerodynamic coefficients, freestream velocity, etc.) taking into account the wind tunnel parameters. However, not much information about the overall applicability of these correlations, i.e. whether they are applicable or not to any type of wind tunnel, is available.

1.2 Objectives

The main objective of this work is to analyze the influence of laminar separation bubbles in the aerodynamic performance of a high lift wing. In addition to that, this work aims to propose a solution to eliminate the formation laminar separation bubbles, using numerical simulations supported by measurements in a wind tunnel.

Specifics objectives of this work are:

- To analyze the wind tunnel boundary corrections for the measured data provided by Selig and McGranaham (2004) by performing numerical simulations and experimental analysis of an airfoil placed inside the wind tunnel.
- To analyze and test the performance of the turbulence models used in flows over airfoils using measurements of the pressure over the airfoil to assess the accuracy of the numerical predictions.

- To evaluate the performance of a leading-edge device used to reduce or eliminate the LSB.

The software used in this work was the Ansys FLUENT and the wind tunnel is located at the Laboratory of Thermal Science (Lab-TERMO) at UFSC. This work continues and enlarges the project initiated by the author in his graduation thesis (HÜBBE, 2014).

1.3 Organization of the Text

Chapter 2 provides all fundamentals for the reader to understand what is accomplished on the following sections. A brief review of aerodynamics, fluid mechanics, CFD and wind tunnel tests are given in this chapter.

Chapters 3 and 4 present the numerical analysis. Chapter 3 describes the numerical approach, such as the airfoils selected, engineering software, meshes used, solver and how some of the parameters may affect the final solution. Chapter 4 gives the numerical results for both freestream and wind tunnel cases.

Chapters 5 and 6 present the experimental analysis. All wind tunnel tests are described in Chapter 5. Model construction, equipment used and measurement procedures are explained in this chapter. Chapter 6 shows the numerical results, comparing them with the numerical data when applicable. The use of leading-edge device is also shown in Chapter 6.

Finally, Chapter 7 presents the conclusions found in this work.

2 LITERATURE REVIEW

2.1 Aerodynamics

2.1.1 Airfoil Geometry

Surfaces that support the aircraft by means of dynamic reaction are called wings (ABBOTT; DOENHOFF, 1959). Any section of the wing cut perpendicular to the wingspan direction is called an airfoil (ANDERSON, 2001).

The National Advisory Committee for Aeronautics (NACA), presently NASA, established a standard nomenclature for the geometric characteristics of airfoils. Such nomenclature is presented in Figure 2.1.

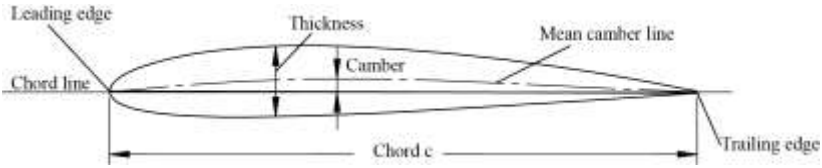

Figure 2.1 – Airfoil geometry (adapted from Anderson (2001)).

The mean camber line is the locus of points halfway between the upper and lower surfaces as measured perpendicular to the mean camber line itself (ANDERSON, 2001). The leading and trailing edge are defined as the forward and rearward extremities, respectively, of the mean camber line. The chord line of the airfoil is the straight line connecting the leading and trailing edges (ABBOTT; DOENHOFF, 1959). The camber is the maximum distance between the mean camber line and the chord line, measured perpendicular to the chord line. Thickness is the distance between the upper and lower surfaces, also measured perpendicular to the chord line (ANDERSON, 2001).

2.1.2 Aerodynamic Forces

The forces acting on the airfoil result from the pressure and shear stress distributions around its surfaces, which are dynamic reactions of the flow past the body. The net effect of these distributions integrated over the complete body surface is a resultant aerodynamic force R' and moment M' (ANDERSON, 2001).

The resultant force R' can be split into components, which are shown in Figure 2.2. The angle between the chord c and the relative wind V_∞ is defined as the angle of attack α. By definition, the lift force L' and

the drag force D' are the components of R' perpendicular and parallel, respectively, to the direction of V_∞. The superscript $'$ indicates that, for a two-dimensional body, the forces and moments are given per unit span (ANDERSON, 2001).

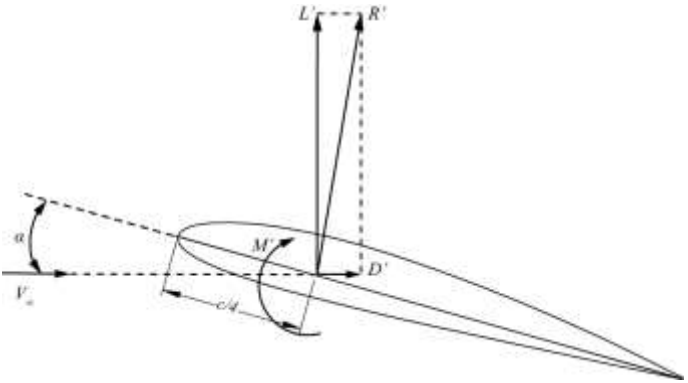

Figure 2.2 – Forces acting on the airfoil (adapted from Anderson (2001)).

Forces and moments acting on the airfoil are commonly expressed as dimensionless numbers. Basic dimensional analysis provides a set of characteristic pressure, force and length scales. The chord length c is used as the characteristic length scale. The free stream dynamic pressure q_∞ given by

$$q_\infty = \frac{1}{2}\rho_\infty V_\infty^2 \tag{2.1}$$

where ρ_∞ and V_∞ correspond to the density and velocity of the air in the free stream, far ahead of the body. Non-dimensional lift, drag and moment coefficients are defined, respectively, C_l, C_d and C_m as

$$C_l = \frac{L'}{q_\infty\, c} \tag{2.2}$$

$$C_d = \frac{D'}{q_\infty\, c} \tag{2.3}$$

$$C_m = \frac{M'}{q_\infty \, c^2} \tag{2.4}$$

The moment coefficient, often called pitching moment coefficient, is usually taken at quarter-chord length, as seen in Figure 2.2. At this location, the moment coefficient is approximately constant for a certain range of α (ABBOTT; DOENHOFF, 1959).

When an airfoil is placed in a moving stream of air, an aerodynamic force acting on the airfoil is created. Experimentally, this force depends on six variables: air velocity V_∞, air density ρ, characteristic length c, angle of attack α, coefficient of viscosity μ and speed of sound V_a. A dimensional analysis reveals that the forces, moments and coefficients for a given airfoil depend on the angle of attack α, Mach number M_∞ and Reynolds number Re (ROSKAM; LAN, 1997) which can be expressed in functional form as:

$$c_l, c_d, c_m = f(Re, M_\infty, \alpha) \tag{2.5}$$

$$M_\infty = \frac{V}{V_a} \tag{2.6}$$

$$Re = \frac{\rho \, V_\infty \, c}{\mu} \tag{2.7}$$

At low air speeds regimes ($Ma < 0.3$), i.e., essentially incompressible flows, the Mach number does not come into the picture. Thus, the aerodynamic coefficients for a fixed shape and at a fixed angle of attack are functions of just the Reynolds number and angle of attack

$$c_l, c_d, c_m = f(Re, \alpha) \tag{2.8}$$

In low-Reynolds aerodynamics, flows typically present Reynolds numbers ranging from 10^4 to 10^6. In this region, many complicated phenomena take place within the boundary layer. Separation, transition and reattachment can all occur within a short distance and can dramatically affect the performance of the airfoil. The laminar separation bubble, explained in section 2.2.5.3, that commonly forms in this region of Reynolds numbers plays an important role in determining the boundary layer behavior and the stalling characteristics of the airfoil. As shown in Figure

2.3, the maximum lift-to-drag ratio, which is used to measure the effectiveness of an airfoil, for smooth airfoils increases by two orders of magnitude in this regime (GAD-EL-HAK, 2001).

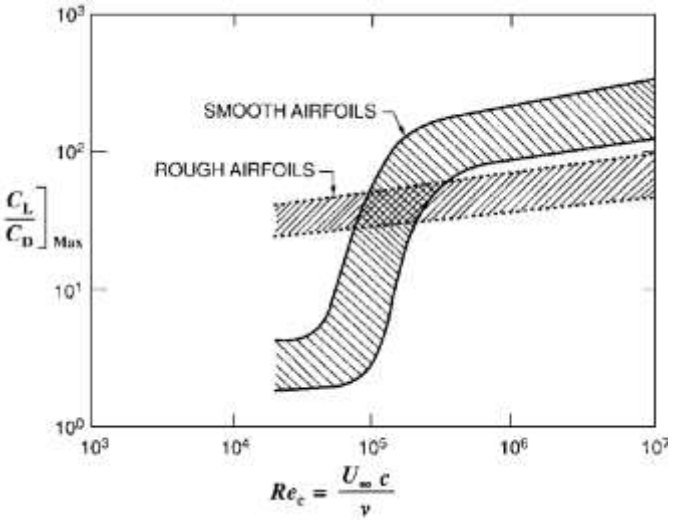

Figure 2.3 – Airfoil performance as a function of Reynolds number. (MCMASTERS; HENDERSON, 1980)

2.1.3 Pressure and Skin Friction Coefficient

Another two important dimensionless quantities of immediate use are the pressure coefficient C_p and the skin friction C_f, defined as:

$$C_p \equiv \frac{p - p_\infty}{q_\infty} \tag{2.9}$$

$$C_f \equiv \frac{\tau_w}{q_\infty} \tag{2.10}$$

where τ_w is the local wall shear stress along the surface of the airfoil.

Assuming the flow as steady state, incompressible, inviscid and with no body forces, C_p can be expressed in terms of velocity only. Consider the flow over an aerodynamic body with pressure p_∞ and velocity V_∞. Pick an arbitrary point in the flow where the pressure and velocity are p and V. From Bernoulli's equation,

$$p_\infty + \frac{1}{2}\rho_\infty V_\infty^2 = p + \frac{1}{2}\rho V^2 \tag{2.11}$$

or

$$p - p_\infty = \frac{1}{2}\rho(V_\infty^2 - V^2) \tag{2.12}$$

Substituting Equation (2.12) into (2.9)

$$C_p = \frac{p - p_\infty}{q_\infty} = \frac{\frac{1}{2}\rho(V_\infty^2 - V^2)}{\frac{1}{2}\rho_\infty V_\infty^2} \tag{2.13}$$

or

$$C_p = 1 - \left(\frac{V}{V_\infty}\right)^2 \tag{2.14}$$

It can be noted from Equation (2.14) that the pressure coefficient at a stagnation point ($V = 0$) in an incompressible flow is always equal to 1. This is the highest allowable value of C_p anywhere in the flow field. Also, in regions where $V > V_\infty$, C_p will assume negative values. (ANDERSON, 2001). Figure 2.4 shows an example of a curve of C_p along the length of the surface of the airfoil.

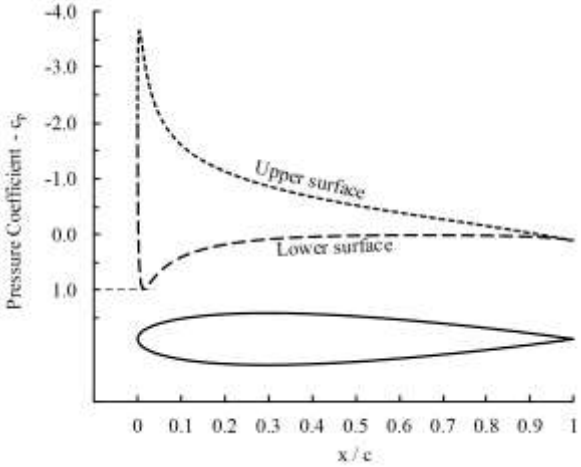

Figure 2.4 – Example of c_p curve for the NACA 0012 at α = 8º.

The pressure coefficient C_p is a dimensionless form of displaying the pressure field around the airfoil (ANDERSON, 2001).

2.1.4 Airfoil Characteristics Curves

In order to compare aerodynamic characteristics of different airfoil geometries as related to their applications in wings, it is common to analyze the variation of their aerodynamic coefficients with the angle of attack α. The generic lift curve versus angle of attack is sketched in Figure 2.5 (ANDERSON, 2001).

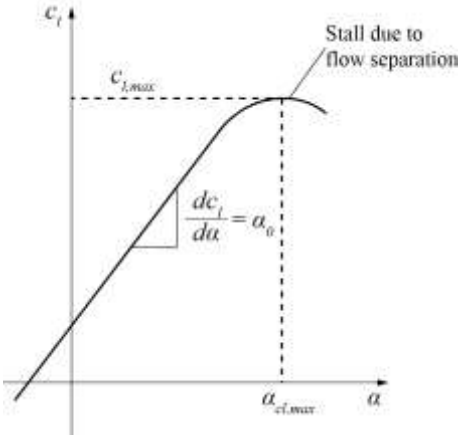

Figure 2.5 – Lift coefficient versus angle of attack (adapted from Anderson (2001)).

At low to moderate angles of attack, C_l varies with α in a linear pattern; the slope of this straight line is denoted by α_0 and is called the lift slope. In this region, the flow moves smoothly over the airfoil and is attached over most of the surface. However, as α becomes large, the flow tends to separate from the top surface of the airfoil. The consequence of that is a precipitous decrease in lift and a large increase in drag; under such conditions, the airfoil is said to be stalled. The maximum value of C_l which occurs just prior to the stall, is denoted by $C_{l.max}$; it is one of the most important aspects of airfoil performance, because it determines the stalling speed of an airplane. The higher the $C_{l.max}$, the lower is the stalling speed (ANDERSON, 2001).

It is also common to plot the lift coefficient as a function of the drag coefficient, often called drag polar, as shown in Figure 2.6.

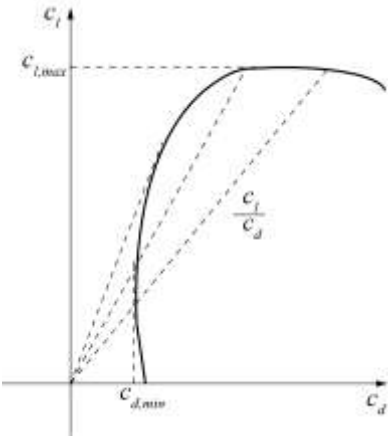

Figure 2.6 – Lift coefficient versus drag coefficient (adapted from Anderson (2001)).

The aerodynamic efficiency is represented in this curve as the lift-to-drag ratio or aerodynamic efficiency C_l/C_d. The maximum value of this parameter is obtained by drawing the tangent from the origin to the curve (ROSKAM; LAN, 1997).

When only drag as a function of the angle of attack is concerned, it is usual to use the C_d x α curve instead of the drag polar (Figure 2.7). Although Figure 2.7 shows the minimum drag occurring at α = 0, $C_{d.min}$ can often occur at non-zero values of α.

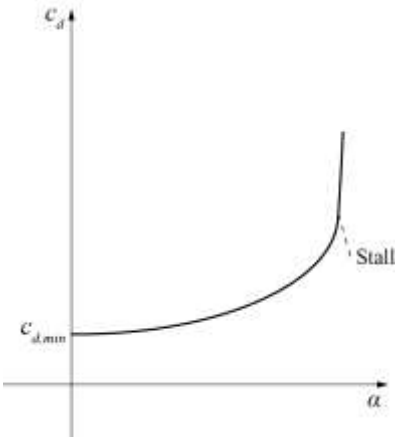

Figure 2.7 – Drag as a function of the angle of attack
(adapted from Anderson (2001)).

2.2 Fundamentals of Fluid Mechanics

In this section, a short review of the basic equations for the flows of incompressible, Newtonian fluids and their application to the understanding of boundary layer flows is presented. The focus is on the explanation and modelling of boundary layer flow separation, since this is the main topic of this work.

2.2.1 Continuity Equation

The continuity equation is a statement about the conservation of mass. It states that, per unit volume, the sum of all mass flowing in and out per unit time must be equal to the change in mass due to the change in density per unit time (SCHLICHTING; GERSTEN, 2017). For unsteady flows, this yields

$$\frac{D\rho}{Dt} + \rho\,\vec{\nabla}\cdot\vec{u} = 0 \tag{2.15}$$

where $\vec{u}$ is the velocity field and ρ the density. In conservation form,

$$\frac{\partial\rho}{\partial t} + \vec{\nabla}\cdot(\rho\vec{u}) = 0 \tag{2.16}$$

Here $D\rho/Dt$ is the substantial derivative of density with respect to time, given by the

$$\frac{D\rho}{Dt} = \frac{\partial \rho}{\partial t} + \vec{u} \cdot \vec{\nabla} \rho \, . \tag{2.17}$$

The total derivative is composed of a local part $\partial\rho/\partial t$ and a convective term $\vec{u} \cdot \vec{\nabla}\rho$.

For incompressible and uniform fluids, there is no change in density with respect to time and space. Hence the first term of Equation (2.15) vanishes, leading to

$$\vec{\nabla} \cdot \vec{u} = 0 \, . \tag{2.18}$$

Equation (2.18) represents the continuity equation for incompressible fluids.

2.2.2 Momentum Equation

The momentum equation is the basic law of mechanics which states that mass times acceleration is equal to sum of forces. Both body forces and surfaces forces (pressure and shear forces) acts on a fluid element.

For any fluid, the momentum equation can be given by

$$\rho \frac{D\vec{u}}{Dt} = \rho \vec{f} + \vec{\nabla} \cdot \bar{\bar{T}} \tag{2.19}$$

where $\vec{f}$ represents the body forces per unit mass acting on the fluid and $\bar{\bar{T}}$ is the stress tensor. The stress tensor $\bar{\bar{T}}$ is a second order tensor containing nine components T_{ij} that completely describe the state of stress at a point inside a material in the deformed state, placement or configuration.

2.2.3 Navier-Stokes Equations

Equation (2.19) is applicable for deformable matter. In order to particularize this equation for fluids, it is necessary to relate the stresses with the rate of strain of fluids. For Newtonian fluids, $\bar{\bar{T}}$ may be given by

$$\bar{\bar{T}} = -\left(p + \frac{2}{3}\mu \, \vec{\nabla} \cdot \vec{u}\right) \bar{\bar{I}} + 2\mu \bar{\bar{D}} \tag{2.20}$$

where p is the thermodynamic pressure, $\bar{\bar{I}}$ is the identity tensor, μ is the dynamic viscosity and $\bar{\bar{D}}$ is rate of strain tensor and its components given by

$$D_{ij} = \frac{1}{2}\left(\frac{\partial u_i}{\partial x_j} + \frac{\partial u_j}{\partial x_i}\right) \tag{2.21}$$

It is also common to denote the rate of strain tensor as $\bar{\bar{S}}$.
Equation (2.20) is actually a constitutive equation for Newtonian liquids, which follows Newton's law of viscosity for incompressible fluids.

Substituting Equation (2.20) into (2.19) and performing the appropriate simplifications, the so-called Navier-Stokes equation for Newtonian fluids in its general form is obtained,

$$\rho\frac{Du_i}{Dt} = -\frac{\partial p}{\partial x_i} + \frac{\partial}{\partial x_j}\left[2\mu D_{ij} - \frac{2}{3}\mu\left(\frac{\partial u_k}{\partial x_k}\right)\delta_{ij}\right] + \rho f_i\,. \tag{2.22}$$

For an incompressible fluid ($\frac{\partial u_k}{\partial x_k} = 0$), or isochoric flow, the conservation of linear momentum reduces to

$$\rho\frac{D\vec{u}}{Dt} = -\vec{\nabla}p + \mu\nabla^2\vec{u} + \rho\vec{f}\,. \tag{2.23}$$

2.2.4 Boundary Layer Concept

In many fluid dynamic flows, it is common to neglect the effect of viscosity to obtain a reasonable solution. However, neglecting viscosity implies that the no-slip condition is not satisfied, i.e. the velocities at the walls assume a finite value. Thus, friction drag and losses cannot be determined. The viscosity must be taken into account in order to satisfy the no-slip condition. At large Reynolds numbers there is a velocity transition which takes place in a thin layer close to the wall. Inside this layer, called by Prandtl as the boundary layer, the velocity assumes a zero value at the wall and a finite value at its boundary (SCHLICHTING; GERSTEN, 2017).

Within the boundary layer the type of flow can be either laminar or turbulent and is a function of the characteristic Reynolds number. The

Reynolds numbers chosen for this work present both laminar and turbulent boundary layers. The whole process of change from laminar to turbulent is termed transition (WHITE, 2005).

Figure 2.8 illustrates the boundary layer on an airfoil. A laminar boundary layer begins its development at the leading edge of the airfoil. After a distance x_{crit} along the contour, the laminar-turbulent transition takes place, so that the boundary layer becomes turbulent for $x > x_{\text{crit}}$.

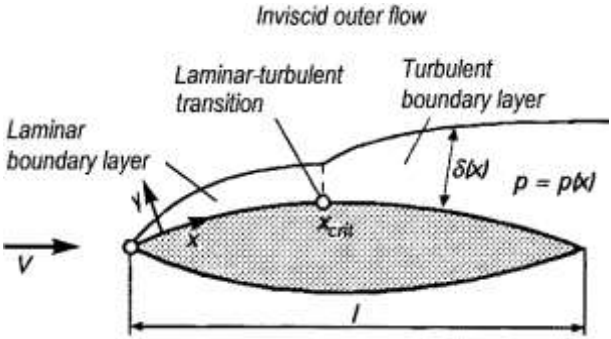

Figure 2.8 – Development of the boundary layer at an airfoil (SCHLICHTING; GERSTEN, 2017).

As the boundary layer moves along the airfoil, generally its thickness $\delta(x)$ increases and the wall shear stress τ_w decreases. This increase in the thickness downstream is greater in the case of turbulent boundary layer than in the laminar case. The pressure distribution imposed by the external flow is important in the formation of the boundary layer. For example, the position of the laminar-turbulent transition has a strong dependency on it. Plus, large adverse pressure gradients can even separate boundary layers from the wall (SCHLICHTING; GERSTEN, 2017).

2.2.5 Laminar-to-Turbulent Transition

Transition in the boundary layer is a complex process even in simple geometries and in a quiet stream. Many factors can influence the laminar boundary layer transition process (WHITE, 2005), such as:

- Freestream turbulence intensity;
- Pressure gradients;
- Wall roughness;
- Surface streamline curvature;

- Mach number;
- Wall suction or blowing;
- Wall heat transfer.

The boundary layer transition can be classified according to the major phenomenon which triggers the process (WHITE, 2005). Mayle (1991) classified the modes of transition in:

2.2.5.1 Natural Transition

A complete description of this process may be found in Schlichting and Gersten (2017). Natural transition is the process which occurs when the freestream turbulence intensity is low (<1%) and walls are smooth. Therefore, this mode is common in external flows, such as those of interest in aerodynamics. Basically, the flow changes from Tollmien–Schlichting waves to three-dimensional waves to vortex breakdown to turbulent spots and to fully turbulent flow. The different stages of this process on a flat plate are shown in Figure 2.9.

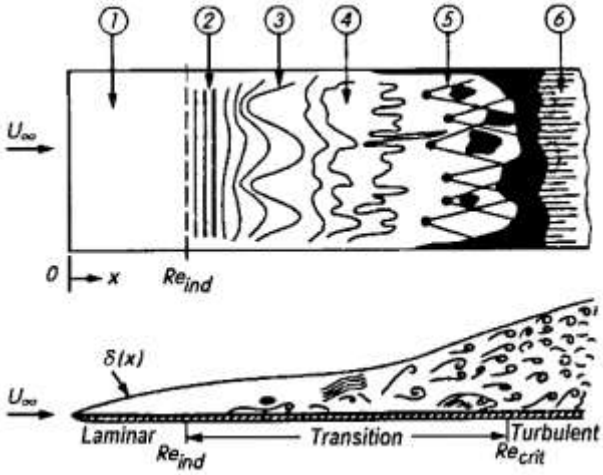

Figure 2.9 – Sketch of laminar-turbulent natural transition in the boundary layer on a flat plate (WHITE, 2005).

In Figure 2.9, the numbered circles indicate the following stages of the natural transition process:

1. Stable laminar flow
2. Unstable Tollmien-Schlichting waves

3. Development of unstable waves and hairpin eddies
4. High localized shear causes vortex breakdown
5. Formation of turbulent spots
6. Fully turbulent flow

2.2.5.2 Bypass Transition

This type occurs at high freestream turbulence levels (>1%). In bypass transition, the first stage of the natural transition, i.e. formation of Tollmien-Schlichting waves, and possibly the second stage, i.e. development of three-dimensional instabilities, are completely bypassed. Thus, turbulent spots are directly produced within the boundary layer by the influence of the freestream disturbances. Figure 2.10 shows a sketch of this mode of transition.

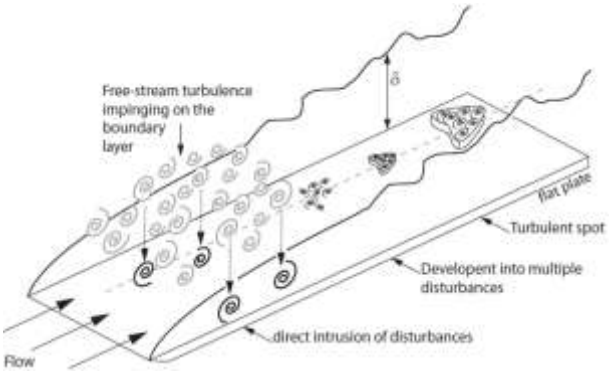

Figure 2.10 – Sketch of the bypass transition process over a flat plate (GHASEMI, *et al*., 2014).

- Wake Induced Transition

Mentioned in Langtry (2006) as an additional mode of transition, this mode occurs by the incidence of a wake produced by an upstream body on the boundary layer. This wake carries a high turbulence intensity which makes the boundary layer bypass the first stages of the transitional process. Although the modeling of this mode results in different equations, it is considered here as a variation of the bypass transition mode.

2.2.5.3 Separated-Flow Transition

When separation occurs in a laminar boundary layer, transition may take place in the shear layer of the separated flow as a result of the

inviscid instability mechanism. In this case, due to the high mixing level caused by the turbulent flow, the shear layer may reattach to the surface. This reattachment forms a laminar-separation / turbulent-reattachment bubble on the surface and may occur as a result of separation due to strong adverse pressure gradient (MAYLE, 1991).

In general, the bubble length depends on the transition process within the shear layer and may involve all of the stages in natural transition. Because of this, it is generally accepted that the freestream turbulence level is important in determining the length of the separation bubble. Traditionally, separation bubbles have been classified as long or short based on their effect on the pressure distribution around an airfoil (MAYLE, 1991). Short bubbles reattach shortly after separation and only have a local effect on the pressure distribution. Long bubbles can completely modify the pressure distribution around an airfoil. Their effects can be compared in Figure 2.11.

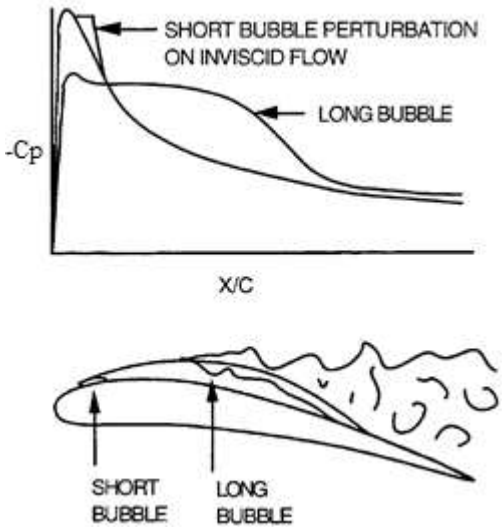

Figure 2.11 – Separation bubble effects on suction side velocity distribution (MALKIEL; MAYLE, 1996).

According to Mayle (1991), long bubbles should be avoided due to the large production of losses and deviations in exit flow angles. Short bubbles on the other hand, can be used to trip the boundary layer and thus allow larger adverse pressure gradients downstream of the reattachment

point. One of the major difficulties lies in determining whether a separation bubble will be long or short. This is aggravated since small changes in either Reynolds number or angle of attack of an airfoil can cause a huge impact on bubble length (MAYLE; SCHULZ, 1997). The sudden change in its length can be called as bursting and can result in a dramatic loss of lift or even cause the airfoil to stall if the bubble fails to reattach the surface (LANGTRY, 2006).

Separation induced transition can also occur around the leading edge of an airfoil if its radius is small enough. According to Walraevens and Cumpsty (1993), the bubble size is a strong function of the freestream turbulence intensity, the leading-edge geometry, the angle of attack and also the Reynolds number. Tain and Cumpsty (2000) found that the size of the leading-edge bubble had a profound effect on the downstream boundary layer. They concluded that the larger the separation, the thicker the downstream boundary layer.

Figure 2.12 shows a schematic of a transition separation bubble. The forward portion of the bubble is a region of constant pressure. It is comprised of an unstable laminar shear layer due to the inflection point in the velocity profile and the large distance away from the region where the presence of the wall damps the velocity fluctuations. The inflection point causes the growth of disturbances which will eventually break down into turbulence at the location marked x_t. Usually, the transition process completes before the shear layer reattaches the surface (LANGTRY, 2006).

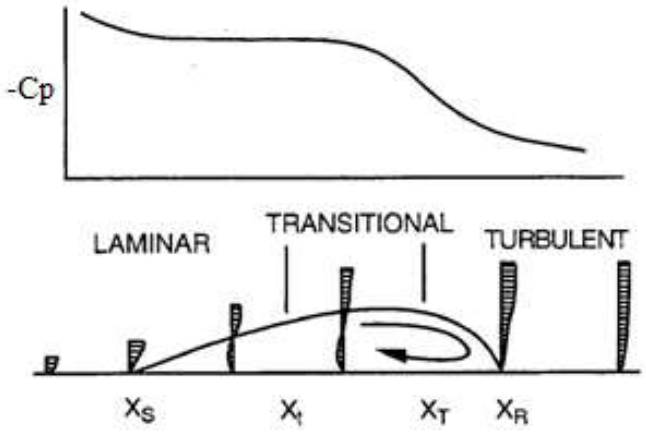

Figure 2.12 – Velocity distribution over a separation bubble (MALKIEL; MAYLE, 1996).

The presence of laminar separation bubble on airfoils can also be identified by analyzing the shear distribution over the airfoil. Negative C_f values indicate that the flow was reversed, and hence, separated. The exact location where C_f changes signs can be used to determine bubble length.

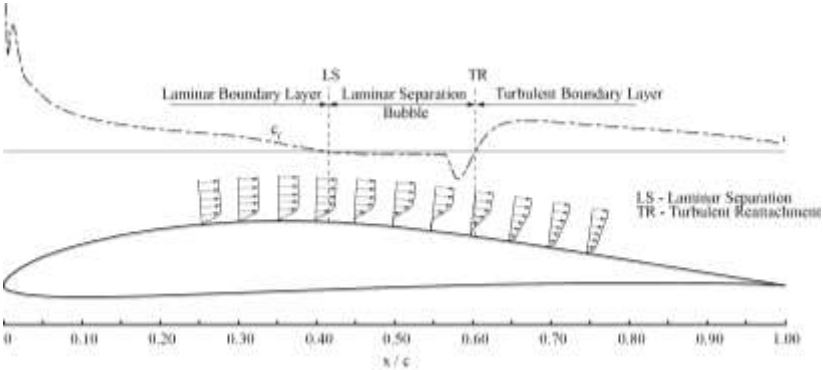

Figure 2.13 – Top surface skin friction distribution of a low-Reynolds airfoil.

2.2.5.4 Reverse Transition

Transition from turbulent to laminar flow is possible if the flow is strongly accelerated. This is often named as "reverse" transition or "relaminarization". The flow acceleration on the pressure side near the trailing edge of most airfoils may be large enough to cause reverse transition (MAYLE, 1991). There is not a lot of experimental data on reverse transition but it is known to occur when the acceleration parameter K, defined as

$$K = \frac{\nu}{U^2}\left(\frac{dU}{dx}\right) \tag{2.24}$$

is greater than about $3 \cdot 10^{-6}$ (MAYLE, 1991). In addition, it is possible for a relaminarized boundary layer to transition back to turbulent flow if the acceleration parameter becomes smaller than $3 \cdot 10^{-6}$.

2.2.6 Turbulent Boundary Layers

One important aspect of predicting turbulent flows is the turbulent boundary layer adjacent to a solid surface. The turbulent boundary layer is composed of two main regions:

- The inner region (10 to 20% of the total boundary layer thickness) where the shear stress is almost constant and equal to the shear stress on the wall τ_w. Within this region, there are three zones; in order of increasing distance from the wall:
    - the viscous sub-layer, where viscous stresses dominate;
    - the buffer layer, where viscous and turbulent effects are of similar magnitude;
    - the log-law layer, where turbulent stresses dominate.
- The outer region, where inertia dominates flow far from the wall and is free from direct viscous stresses.

To better define the thickness and velocity for each region in the boundary layer, the dimensionless distance y^+ and the shear velocity u^* are defined.

$$u^* = \sqrt{\frac{\tau_w}{\rho}} \tag{2.25}$$

$$y^+ = \frac{\rho u^* y}{\mu} \tag{2.26}$$

On a boundary layer over a flat plate, the viscous sub-layer occurs for $y^+ \leq 5$. In this region, $U/u^* = y^+$. The logarithmic region occurs for $30 < y^+ < 500$ and U/u^* is a logarithmic function of y^+

$$\frac{U}{u^*} = \frac{1}{\kappa} ln(y^+) + a \tag{2.27}$$

where $\kappa = 0{,}41$ and $a = 5{,}2$.

Figure 2.14 illustrates the three zones of the inner region.

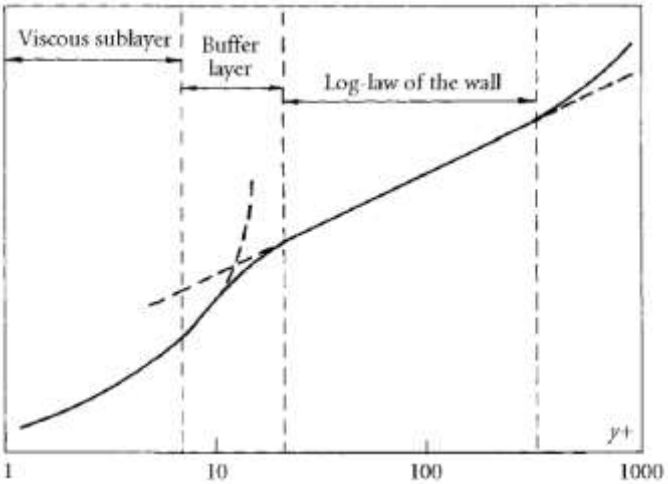

Figure 2.14 – A plot of U/u^* versus y^+ showing the inner region of a turbulent boundary layer. (DAVIDSON, 2004)

2.3 Modelling and Simulation

Simulations of turbulent flows can be performed through the use of different approaches. In direct numerical simulation (DNS), the Navier-Stokes equations are solved to determine the velocity field. Since all lengthscales and timescales need to be resolved, DNS is computationally expensive. In large-eddy simulation (LES), equations are solved for a filtered velocity field $\overline{U}(x,t)$, which is capable of solving the larger-scale turbulent motions. The equations include a model to include the influence of the smaller-scale motions eddies which are not directly represented (POPE, 2000).

The Reynolds-Averaged Navier Stokes (RANS) approach solves the Reynolds equations to determine the mean velocity field $\overline{U}$. Reynolds stresses can be calculated from a turbulent-viscosity model, which can be obtained from an algebraic relation (e.g. mixing-length model) or it can be obtained from turbulence quantities such as k and ε for which modelled transport equations are solved (POPE, 2000). RANS approach is better explained in section 2.3.1. and, due to its simplicity and low computational cost, will be used in this work.

In order to solve the RANS equations, it is common to discretize them using the Finite Volume Method (FVM). In this method, flow variables are calculated at each boundary of each control volume by surface integrals. As a result, FVM is called conservative. One advantage is that it can be easily formulated for uses in unstructured meshes (MALISKA, 2004). Plus, it is implemented in Fluent, a powerful and widely used CFD software tool used in this work.

Fluent contains a variety of RANS models to predict turbulent flows. These are called turbulence models and each of them is more appropriate to a certain type of flow. Sections 2.3.2 and 2.3.3 provide a brief description of the Spalart-Allmaras and SST k-ω fully-turbulent models, respectively, and sections 2.3.4 and 2.3.5 briefly describe the transition-sensitive γ-Re_θ and k-k_L-ω models.

2.3.1 Reynolds-Averaged Navier-Stokes (RANS) Equations

Turbulent flows exhibit transient and chaotic pressure and velocity fields. The velocity fields fluctuate intensively, changing both flow direction and magnitude in spatial and time scales that span many orders of magnitude. The detailed solution for the velocity field in all temporal and spatial scales is computationally intensive and not really applicable for the simulation of relatively large domains common in engineering applications. The time averaging of the pointwise flow equations allows to circumvent this need, by solving only for the average velocity and pressure fields. This is the essence of the Reynolds-Averaged Navier-Stokes equations (RANS). As a drawback of this treatment, closure assumptions are needed in order to model the extra terms that arise from the averaging of the Navier-Stokes equations. The different forms of modeling of these terms give rise to the different turbulence models. Several references review the basic concepts and mathematical foundations of modeling of turbulence as, for example, POPE (2000). Here, only a few basic concepts are reviewed.

In the basic Reynolds averaging, the instantaneous variables in the (exact) Navier-Stokes equations are decomposed into the mean and fluctuating components. For the velocity components:

$$u_i = \overline{U}_i + u_i' \tag{2.28}$$

where $\overline{U}_i$ and u_i' are the mean and fluctuating velocity components.

Likewise, for pressure and any other scalar quantity:

$$\phi_i = \bar{\Phi}_i + \phi_i' \tag{2.29}$$

where ϕ denotes a scalar such as pressure, energy or species concentrations.

Substituting expressions of this form for the flow variables into the instantaneous continuity and momentum equations (Eqs. (2.15) and (2.19)) and taking $U_i = \bar{U}_i$, it can be shown that

$$\frac{\partial U_i}{\partial t} + U_j \frac{\partial U_i}{\partial x_j} = \frac{1}{\rho}\frac{\partial}{\partial x_j}\left[-P\delta_{ij} + \mu\left(\frac{\partial U_i}{\partial x_j} + \frac{\partial U_j}{\partial x_i}\right) - \rho\overline{u_i u_j}\right] \tag{2.30}$$

which is known as the RANS equations. They have the same general form as the instantaneous Navier-Stokes equations, with the velocities and scalars now representing averaged values. The Reynolds stress tensor, $-\rho\overline{u_i u_j}$, now appears.

In order to solve Equation (2.30), the Reynolds stresses must be evaluated. To obtain equations containing only the mean velocity and pressure, one need to close the RANS equations by modeling the Reynolds stresses as a function of the mean flow. This is known as the closure problem.

Boussinesq proposed relating the turbulence stresses to the mean flow by introducing a proportionality constant known as the eddy viscosity ν_t. This term relates the Reynolds stresses with the mean flow and may be given, in a general form, as

$$-\overline{u_i u_j} = \nu_t\left(\frac{\partial U_i}{\partial x_j} + \frac{\partial U_j}{\partial x_i}\right) - \frac{2}{3}\left(k + \nu_t\frac{\partial u_k}{\partial x_k}\right)\delta_{ij} \tag{2.31}$$

where k is the turbulent kinetic energy given by

$$k = \frac{\overline{u_i u_i}}{2} \tag{2.32}$$

The Boussinesq hypothesis is used in a variety of turbulence models. The advantage of this approach is the relatively low computational cost associated with the computation of the turbulent viscosity ν_t. In the case of the Spalart-Allmaras model, only one additional transport equation (representing the turbulent viscosity) is solved. In the case of the

SST k-ω, two additional transport equations (one for the turbulent kinetic energy k and one for the specific dissipation rate ω) are solved, and ν_t is calculated as a function of k and ω.

The following sections describe a few turbulence models which make use of the Boussinesq hypothesis.

2.3.2 Spalart-Allmaras Model

The Spalart-Allmaras model is a one-equation model, that solves a modeled transport for the kinematic eddy viscosity. It was designed for aerospace applications that involves wall-bounded flows subjected to adverse pressure gradients (SPALART; ALLMARAS, 1992).

According to Spalart and Allmaras (1992), the model has been calibrated on 2D mixing layers, wakes and flat plate boundary layers, yielding good predictions of boundary layers subjected to adverse pressure gradients.

The transported variable in the Spalart-Allmaras model is $\tilde{\nu}$. It is identical to the turbulent kinematic viscosity except in the near-wall region. The one-equation model is given by,

$$\frac{\partial}{\partial t}(\rho\tilde{\nu}) + \frac{\partial}{\partial x_i}(\rho U_i\tilde{\nu}) = P_\nu + \frac{1}{\sigma_{\tilde{\nu}}}\left[\frac{\partial}{\partial x_j}\left((\mu + \rho\tilde{\nu})\frac{\partial\tilde{\nu}}{\partial x_j}\right) + C_{b2}\rho\left(\frac{\partial\tilde{\nu}}{\partial x_j}\right)^2\right] - Y_\nu \tag{2.33}$$

P_ν is the production term and Y_ν is the destruction of turbulent viscosity. $\sigma_{\tilde{\nu}}$ and C_{b2} are constants and ν is the molecular kinematic viscosity.

Details regarding the development of the model equations can be found in Spalart and Allmaras (1992) listed in the references.

2.3.3 SST k-ω

The strictly empirical basis shear-stress transport (SST) k-ω model was presented by Menter (1994). Its goal was to blend the robust and accurate formulation of the k-ω model in the near-wall region with the freestream independence of the k-ε model in the far field. This would result in a model which has good prediction of skin friction drag and less sensible to freestream turbulence. To achieve this, both models are multiplied by a blending function and then added together.

According to Menter (1994), the SST model represents a good choice for aerodynamic applications since it improves the performance of flows involving adverse pressure gradients. The pressure-induced separation has been accurately predicted by this model.

The new set of equations for the SST k-ω are

$$\frac{\partial(\rho k)}{\partial t}+\frac{\partial}{\partial x_i}(\rho U_i k)=P_k-Y_k+\frac{\partial}{\partial x_i}\left[\left(\mu+\frac{\mu_t}{\sigma_k}\right)\frac{\partial k}{\partial x_i}\right] \quad (2.34)$$

$$\frac{\partial(\rho \omega)}{\partial t}+\frac{\partial}{\partial x_i}(\rho U_i \omega)=P_\omega-Y_\omega+D_\omega+\frac{\partial}{\partial x_i}\left[\left(\mu+\frac{\mu_t}{\sigma_\omega}\right)\frac{\partial \omega}{\partial x_i}\right] \quad (2.35)$$

Details of the development of the model can be found in Menter (1994).

2.3.4 γ-Re$_\theta$ Transition Model

According to Langtry (2002), a transition model for CFD applications should meet the following requirements:

- It must be sensitive to the physics that affect transition.
- It must be computationally inexpensive.
- It should be easy to incorporate into existing CFD codes and should be compatible with one or more widely accepted turbulence models.
- It should be compatible with unstructured grids.

Also, another requirement for the development of the transition model is that only local variables and gradients, as well as the wall distance could be used in the equations. The γ-Re$_\theta$ model meets all of these requirements (MENTER, *et al.*, 2006).

This model is based on the SST model and solves two additional transport equations. The first is for the intermittency γ. This variable is responsible for triggering the transition process by turning on the production term of the turbulent kinetic energy. The formulation for γ has also included the rapid onset of transition caused by separation of laminar boundary layer. Plus, the γ equation can be fully calibrated with transition onset and transition length empirical correlations (MENTER, *et al.*, 2006). The intermittency equation is formulated as follows:

$$\frac{\partial(\rho \gamma)}{\partial t}+\frac{\partial(\rho U_j \gamma)}{\partial x_j}=P_{\gamma 1}-E_{\gamma 1}+P_{\gamma 2}-E_{\gamma 2}+\frac{\partial}{\partial x_j}\left[\left(\mu+\frac{\mu_t}{\sigma_f}\right)\frac{\partial \gamma}{\partial x_j}\right] \quad (2.36)$$

In addition to the transport equation for the intermittency, the other equation is solved in terms of the transition onset momentum-thickness Reynolds number ($\tilde{R}e_{\theta t}$). The need of this is to capture the nonlocal influence of the turbulence intensity, which changes due to the decay of the turbulent kinetic energy in the freestream and due to changes in the freestream velocity outside the boundary layer. This equation is an essential part of the model as it links the empirical correlation to the onset criteria in the intermittency equation (MENTER, *et al.*, 2006). The transport equation for the transition momentum thickness Reynolds number $\tilde{R}e_{\theta t}$ is defined as follows:

$$\frac{\partial(\rho\tilde{R}e_{\theta t})}{\partial t}+\frac{\partial(\rho U_j\tilde{R}e_{\theta t})}{\partial x_j}=P_{\theta t}+\frac{\partial}{\partial x_j}\left[\sigma_{\theta t}(\mu+\mu_t)\frac{\partial\tilde{R}e_{\theta t}}{\partial x_j}\right] \qquad (2.37)$$

The interaction between the γ-Re$_\theta$ with the SST model is mainly performed in the production of turbulent kinetic energy term. In addition, the term regarding the destruction of turbulence and one other function of the SST model are modified. Equation (2.38) shows the modified version of the transport equation for k. Apparently, this equation is the same as in the SST model, however, the terms for production and destruction of turbulence are altered to $\tilde{P}_k$ and $\tilde{Y}_k$.

$$\frac{\partial(\rho k)}{\partial t}+\frac{\partial}{\partial x_i}(\rho U_i k)=\tilde{P}_k-\tilde{Y}_k+\frac{\partial}{\partial x_i}\left[\left(\mu+\frac{\mu_t}{\sigma_k}\right)\frac{\partial k}{\partial x_i}\right] \qquad (2.38)$$

where

$$\tilde{P}_k=\gamma_{eff}\,P_k \qquad (2.39)$$

$$\tilde{Y}_k=min[max(\gamma_{eff};0{,}1);1]\,Y_k \qquad (2.40)$$

In regions of laminar boundary layer, $\gamma_{eff}=0$, which turns off the production term. In cases of natural transition, bypass transition, or even transition induced by wake, γ_{eff} varies between $0\leq\gamma_{eff}\leq 1$. Hence, the production term gradually increases until it reaches the regular value of the SST model. In cases of separation induced transition, γ_{eff} varies between $0\leq\gamma_{eff}\leq 2$. This amplifies the production term to account for the rapid transition that occurs in the free shear layer of the separated boundary layer (MENTER, *et al.*, 2006).

Figure 2.15 illustrates how the intermittency γ affects the turbulent kinetic energy k. By observing the contour of γ in the boundary layer region, at the end of the transition process, its value rapidly changes from 0 to 1. Now, if one analyzes contours of k at the spot, it is seen that this is the exact location where values of k start to increase. This is a result of the turning on and off process of the production term dictated by the intermittency γ.

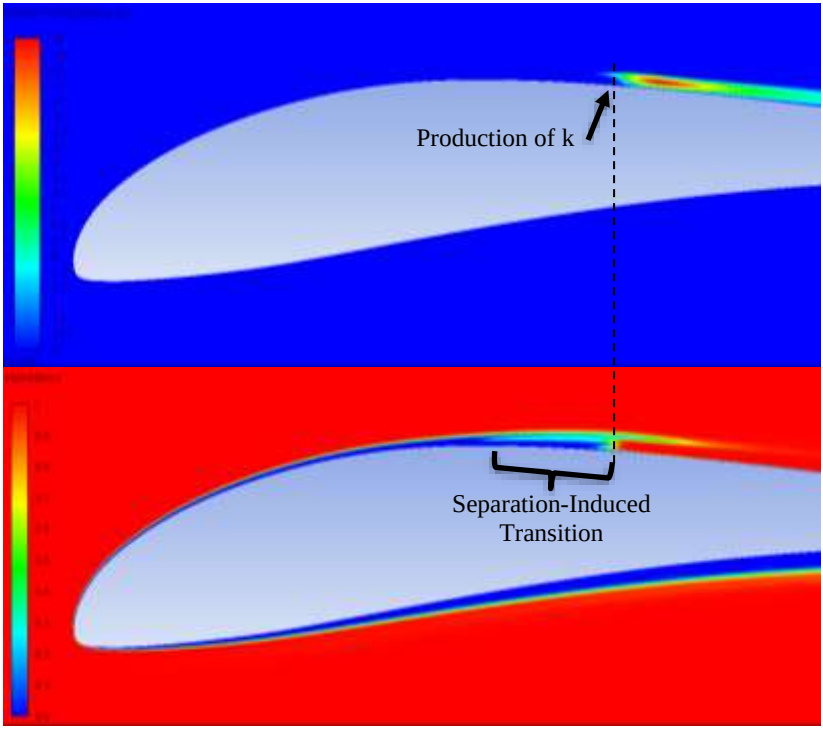

Figure 2.15 – Contours of turbulent kinetic energy k (top) and intermittency γ (bottom) of an airfoil.

More information about the development of the γ-Re_θ model can be found in Menter, *et al.* (2006).

2.3.5 k-k_L-ω Transition Model

The k-k_L-ω model is based on the k-ω framework and is stated as a great progress to transition-sensitive models used in CFD. The main

difference from the other empirical models is that it avoids the use of empirical correlations to experimental data. Instead, it includes a phenomenological approach to represent the pretransitional fluctuations in laminar attached or separated boundary layers. Since the physics of transition is not entirely understood, some authors have argued that correlation-based models are more appropriate for candidates for consistent RANS-based transition prediction than physics-based counterparts. Still, recent analytical, numerical and experimental investigations have helped to highlight some of the relevant physical mechanisms and also the universal characteristics of boundary layer flows, both transition and turbulent (WALTERS; COKLJAT, 2008).

In the k-k_L-ω model, three additional model transport equations are solved for the turbulent kinetic energy (k_T), the laminar kinetic energy (k_L), and the scale-determining variable (ω), defined here as $\omega = \varepsilon/k_T$. The transport equations are

$$\frac{Dk_T}{Dt} = P_{k_T} + R_{BP} + R_{NAT} - \omega k_T - D_T + \frac{\partial}{\partial x_j}\left[\left(\nu + \frac{\alpha_T}{\sigma_k}\right)\frac{\partial k_T}{\partial x_j}\right] \tag{2.41}$$

$$\frac{Dk_L}{Dt} = P_{k_L} - R_{BP} - R_{NAT} - D_L + \frac{\partial}{\partial x_j}\left[\nu\frac{\partial k_L}{\partial x_j}\right] \tag{2.42}$$

$$\begin{aligned}\frac{D\omega}{Dt} = C_{\omega 1}\frac{\omega}{k_T}P_{k_T} + \left(\frac{C_{\omega R}}{f_W} - 1\right)\frac{\omega}{k_T}(R_{BP} + R_{NAT}) - C_{\omega 2}\omega^2 \\ + C_{\omega 3} f_\omega \alpha_T f_W^2 \frac{\sqrt{k_T}}{d^3} + \frac{\partial}{\partial x_j}\left[\left(\nu + \frac{\alpha_T}{\sigma_\omega}\right)\frac{\partial \omega}{\partial x_j}\right]\end{aligned} \tag{2.43}$$

The k_L equation is included to predict the magnitude of the low-frequency velocity fluctuations in the pre-transitional boundary layer. The actual transition process is represented in the model by a transfer of energy from the laminar kinetic energy k_L to the turbulent kinetic energy k_T (WALTERS; COKLJAT, 2008).

Walters and Cokljat (2008) have tested this model in airfoil flow cases. They stated that the model presented great improvements compared to fully-turbulent models without the need for empirical correlations.

More detailed information about the development of the model can be encountered in Walters and Cokljat (2008).

2.4 Wind Tunnel Testing

The flow conditions in a wind tunnel are not completely the same as in an unbounded airstream or in freestream in the case of an aircraft. There is no difference traceable to having the model at rest and the air moving relative to the local earth reference. However, the distances of some stream boundaries from the article under test are usually less than the corresponding distances for actual operations. This is the most fundamental of the effects that must be evaluated (BARLOW, *et al.*, 1999).

2.4.1 Boundary Corrections

2.4.1.1 Solid Blockage

The presence of the tunnel walls confining the flow around a model reduces the area through which the air must flow as compared to freestream conditions and hence, by continuity and Bernoulli's equation, increase the velocity of the air as it flows in the vicinity of the model. This increase of velocity is called solid blockage. Its effect is a function of model thickness, thickness distribution and model size.

A simple form of the solid blockage correction for two-dimensional tunnels has been given by Thom (1943) and was used by Selig and McGranaham (2004) in their work. Thom's solid blockage correction is

$$\varepsilon_{sb} = \frac{K_{sb} V_m}{A_s^{3/2}} \tag{2.44}$$

where K_{sb} equals 0,74 for a wing spanning the tunnel width, V_m is the airfoil model volume and A_s is the tunnel test-section area. If greater accuracy is desired, the term A_s may be taken as the geometric area less the boundary layer displacement thickness taken around the perimeter (BARLOW, *et al.*, 1999).

2.4.1.2 Wake Blockage

Any real body will generate a wake that has a mean velocity lower than the freestream. According to the law of continuity, the velocity outside the wake in a closed tunnel must be higher than the freestream in order that a constant volume of fluid may pass through each cross section. This increase in velocity may be seen in Figure 2.16.

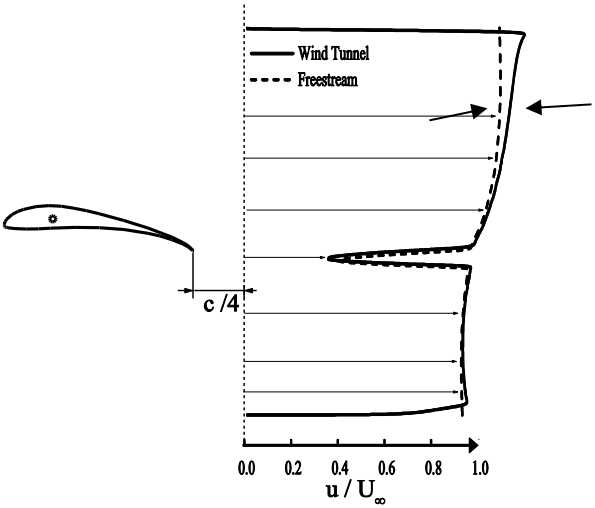

Figure 2.16 – Example of increase in velocity outside the wake in a wind tunnel.

The higher velocity in the main stream has a lowered pressure, and this lowered pressure, arising as the boundary layer grows on the model, puts the model in a pressure gradient, and results in a velocity increment at the model (BARLOW, *et al.*, 1999).

Maskell (1965) has examined the effect of the flow outside the wake and how its higher speed results in a reduced pressure over the rearward portion of the model. He suggests that the wake blockage correction be

$$\varepsilon_{wb} = \frac{c/h}{2} C_{d,u} \tag{2.45}$$

where c is the model chord length, h is the test section height and $C_{d,u}$ is the uncorrected drag coefficient.

Wake blockage may be neglected for the rare case of a two-dimensional test section with open top and bottom (BARLOW, *et al.*, 1999).

2.4.1.3 Streamline Curvature

Due to the physical constraints of the tunnel boundaries, the normal curvature of the free air as it passes over a lifting body (such as an airfoil) is altered, increasing the airfoil effective camber as the streamlines are "squeezed" together, as seen in Figure 2.17.

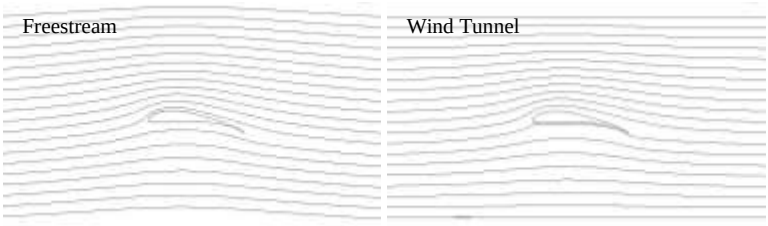

Figure 2.17 – Streamline curvature in freestream and wind tunnel cases.

In closed wind-tunnel sections, the increase in camber results in an increase in lift, pitching moment about the quarter-chord point, and angle of attack; the drag is unaffected (SELIG; MCGRANAHAM, 2004). The variation in lift coefficient and angle of attack are given by

$$\Delta C_{l,sc} = -\sigma C_{l,u} \tag{2.46}$$

$$\Delta \alpha_{sc} = \frac{57.3\sigma}{2\pi}(C_{l,u} + 4C_{m,u}) \tag{2.47}$$

where $C_{l,u}$ and $C_{m,u}$ are the uncorrected lift and pitching moment coefficients. The constant σ is defined by

$$\sigma = \frac{\pi^2}{48}\left(\frac{c}{h}\right)^2 \tag{2.48}$$

2.4.2 Correction to Measured Quantities

The measured quantities that must be corrected can be subdivided into two categories: stream and model quantities. The most important stream quantity is the velocity at the model. This velocity was obtained from the free stream velocity measurements and by applying the proper corrections to account for solid and wake blockage as well as boundary layer growth on the tunnel walls (SELIG; MCGRANAHAN, 2004). The corrections for velocity and Reynolds number are displayed below

$$V = V_u(1 + \varepsilon_{sb} + \varepsilon_{wb}) \tag{2.49}$$

$$Re = Re_u(1 + \varepsilon_{sb} + \varepsilon_{wb}) \tag{2.50}$$

where V is the corrected velocity; V_u is the uncorrected velocity; Re is the corrected Reynolds number; Re_u is the uncorrected Reynolds number.

The model quantities of interest are the lift, drag and angle of attack, which were corrected in their non-dimensional form to account for solid and wake blockage as well as streamline curvature and dynamic pressure corrections. These corrections are expressed as

$$C_l = C_{l,u} \frac{1 - \sigma}{(1 + \varepsilon_{sb} + \varepsilon_{wb})^2} \tag{2.51}$$

$$C_d = C_{d,u} \frac{1 - \varepsilon_{sb}}{(1 + \varepsilon_{sb} + \varepsilon_{wb})^2} \tag{2.52}$$

$$\alpha = \alpha_u + \frac{57.3\ \sigma}{2\pi} \cdot (C_l + 4\ C_{m,u}) \tag{2.53}$$

where C_l is the corrected lift coefficient; C_d is the corrected drag coefficient; and α is the corrected angle of attack.

2.4.3 Surface Oil Flow Visualization

Information about the flow on the surface of an object being studied is extremely important in some cases. Many times, the flow away from the body is of interest primarily in order to understand the flow features on the surface. Key aspects that may be investigated using visualization techniques include stagnation point location, separation line, location of boundary layer transition and extent of separation zones (BARLOW, *et al.*, 1999).

Oil and other viscous fluids can many times be used to reveal the surface flow. The selected material is usually spread on the areas of interest with a paint brush. It will then flow under the action of shear forces from the air stream and gravity. In low air speeds or high viscous oil mixtures, the oil may fail to flow on the surface and reveal flow pattern. Thus, the viscosity of the mixture should be properly calibrated (BARLOW, *et al.*, 1999).

Barlow, *et al.*, (1999) states that the most common material for oil flow is petroleum lubricating oils, but they may be messy to clean up afterward. The color of the oil needs to contrast with the color of the model surface. A widely used method is to add a fluorescent dye to the oil and illuminate it with ultraviolet lights.

In order to avoid the need of fluorescent dye and special lights, oil can be made white by adding titanium dioxide. This mixture contrasts well with black surfaces. Genç, *et al.*, (2012) used kerosene, titanium dioxide and a very small amount of oleic acid, which helps to see the pigment deposit on the oiled surface.

Selig and McGranaham (2004) used a mixture of a light household-grade mineral oil with a fluorescent pigment (Kent-Moore 28431-1). The mixture was sprayed onto the surface of the model using a Paasche Model VL airbrush. The model was then subjected to 20-45 min of continuous wind tunnel run time at a fixed speed and angle of attack. As a result, discernible regions of the flow could be identified, as shows Figure 2.18.

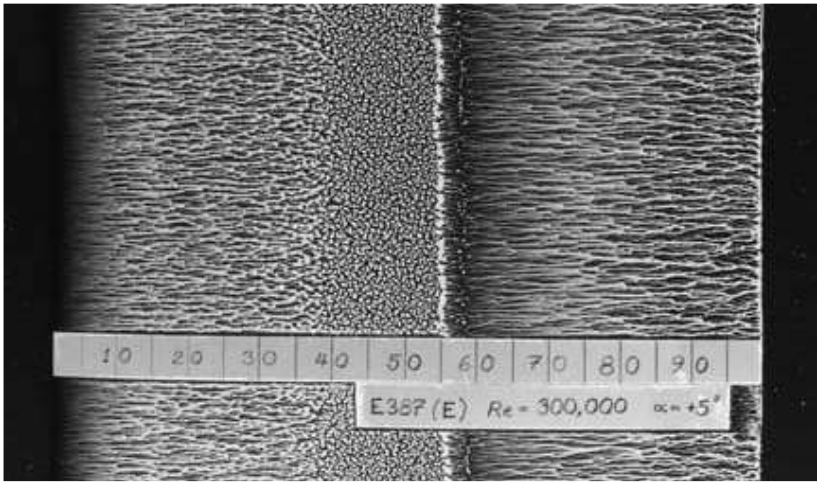

Figure 2.18 – Representative upper-surface oil flow visualization on the E387 airfoil. (SELIG; MCGRANAHAM, 2004)

Figure 2.19 illustrates the connection between the salient surface oil flow features and the skin friction distribution. According to Selig and McGranaham (2004), the skin friction distribution, though conceptual, is consistent with the results of many computational studies. However, the unique shape of the C_f distribution, in particular the strong negative C_f spike, has yet to be experimentally verified.

Several important flow features can be identified and related to the underlying skin friction and surface tension forces. In Figure 2.18, laminar flow is seen to exist from the leading edge to approximately x/c =

40%. The oil streaks are characteristically smooth in this region until laminar separation, which has been identified in Figure 2.19 as the point where $C_f = 0$. (Note again that the flow shown in Figure 2.19 is conceptual, and it is not intended to match Figure 2.18 in detail.) Downstream of the point of laminar separation, the original airbrushed "orange-peel" texture that existed before running the tunnel test still exists, indicating that the flow is stagnant in this region. This stagnant flow is consistent with the known behavior of the interior leading-edge region of a laminar separation bubble. As sketched, the magnitude of the C_f in this region is quite small because of the low flow speed and negative in sign because of reverse flow at the surface. As seen in Figure 2.19, the reattachment line is less distinct because the bulk of the oil has been pushed away, revealing the black airfoil surface. In Figure 2.18, the reattachment line at x/c = 58% is even harder to see (SELIG; MCGRANAHAM, 2004).

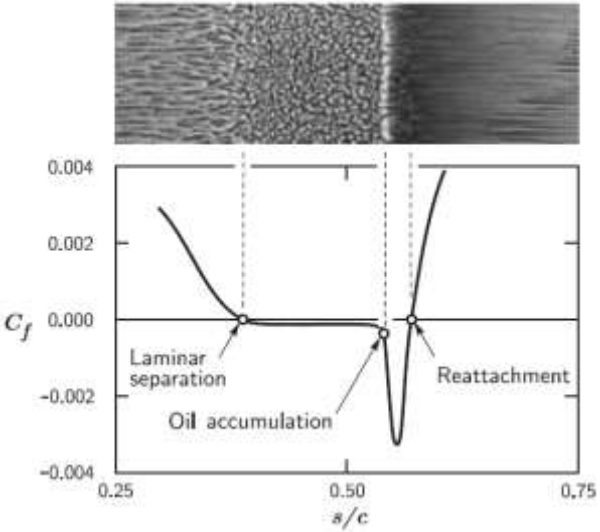

Figure 2.19 – Conceptual illustration of the relationship between the surface oil flow features and skin friction distribution in the region of a laminar separation bubble. (SELIG; MCGRANAHAM, 2004)

The upper-surface flow features, identified in Figure 2.19, can be obtained for different angles of attack and Reynolds numbers, and then plotted in charts, as shows Figure 2.20. The distance from the separation point to the reattachment point is actually the bubble length.

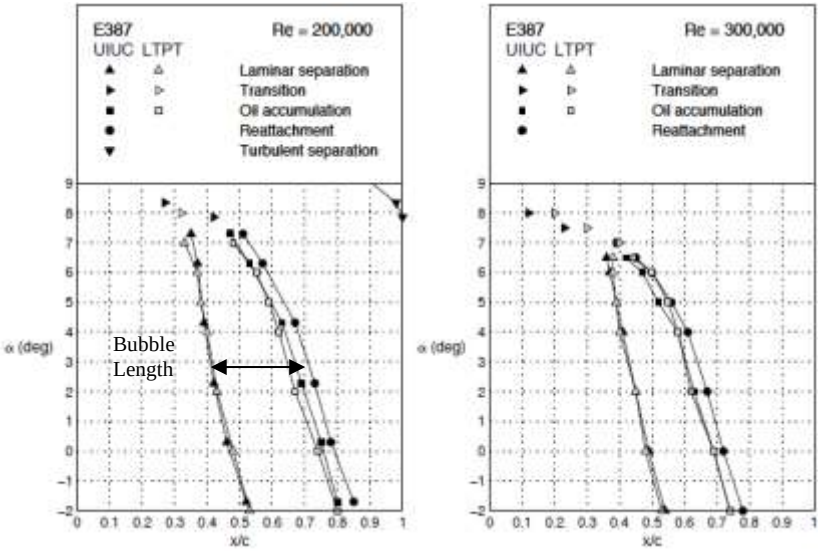

Figure 2.20 – Comparison of major Eppler 387 upper-surface flow features between UIUC and LTPT. (SELIG; MCGRANAHAM, 2004)

3 METHODOLOGY – NUMERICAL ANALYSIS

This work aims to investigate the performance of different turbulence models in airfoils. The airfoils chosen were the Eppler 387, since it is a common low-Reynolds airfoil and has reliable wind tunnel data available, and the Selig 1223, because of its high-lift capability and usability in low-speed aircrafts. The airfoils are first simulated in a freestream environment and then placed in a wind tunnel domain.

3.1 Software

In this thesis, Ansys CFD tools and Pointwise were used. Ansys is a simulation package software for many engineering fields. The modules used were:

- Pointwise – grid generation;
- Ansys Fluent – case setup and solver;
- Ansys CFD Post – Post-processing.

Pointwise is a computer software that can be employed to produce models in two and three dimensions, using structured or unstructured meshes, which can consist of a variety of elements, such as quadrilateral, triangular or tetrahedral elements. In this work, due to the low computational cost, all meshes were generated in a 2D C-domain.

3.2 Domain and Boundary Conditions – Freestream

The domain chosen is represented in Figure 3.1. It is a C-type grid topology, widely used in numerical simulations of airfoils.

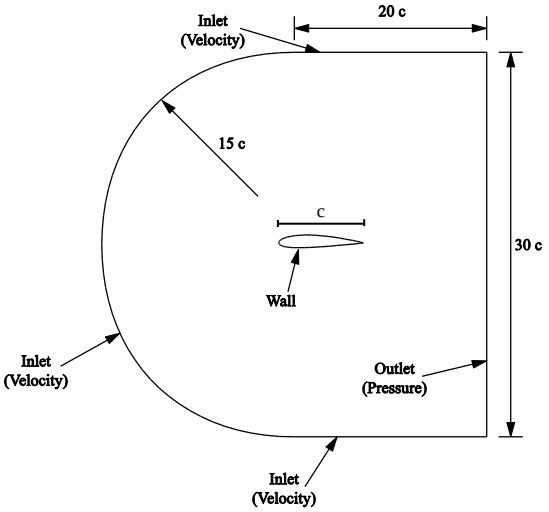

Figure 3.1 – Computational domain for freestream cases.

An important issue in the grid is how far the inlet boundary condition is placed from the leading edge of the airfoil. For Ma = 0.15 and Re = $6 \cdot 10^6$ the lift coefficient predicted when the inlet boundary condition is at 30 c (30 times the chord length) is only 0,17 % smaller than the lift coefficient predicted at 500 c. The drag coefficient is predicted with 4,36 % deviation (NASA, 2014). The need for larger domains increases as the Ma and Re number increase. For low Reynolds numbers, however, grid size shows lower influence in lift and drag coefficients. Thomas and Salas (1986) develop a method that increases the accuracy of predictions for sub-sonic and transonic flows, by using a correction in the boundary condition when Euler´s equation is solved for the far field in computation domains smaller than 50 c. Kaynak *et al*. (2012) used 14 c for an airfoil at Re from $2 \cdot 10^5$ to $5 \cdot 10^5$ and Ma from 0,6 to 0,7, achieving good comparison with measurements for a NACA64A006 airfoil. Here, the domain height was set to 30 chord lengths. It extends from 15 chord lengths upstream to 20 chord lengths downstream.

At the inlet, the components of the air velocity are specified. For all cases, only the x component was set to a non-zero value and different angles of attack were achieved by rotating the whole domain.

Spalart and Rumsey (2007) presented equations to help the user set the correct values for the turbulence boundary conditions. For Re = $1 \cdot 10^5$, they suggest 0,1 % for the freestream turbulence intensity and 0,02 viscosity ratio (ν_t/ν) at the inlet. These values were used in the freestream

cases and can be converted to values of k and ω (or $\tilde{\nu}$ in the case of the Spalart-Allmaras) through the use of some relations specified in Fluent. An analysis of the influence of the freestream turbulence intensity in the flow is described section 3.6.

All surfaces of the airfoil were set as stationary walls. At the outlet, the static pressure is equal to zero.

3.3 Discretization of the Domain

For both freestream and wind tunnel test cases the geometry domain was discretized using structured (quadrilateral) and unstructured (triangular) cells. In order to achieve a grid-independent solution the height of the first cell adjacent to the airfoil and the total number of elements of the fluid region were varied resulting in seven different grids. The growth rate of the elements height was set to 1,1. These cases were run at a Reynolds number of $2 \cdot 10^5$ and angle of attack of 0°, 6° and 10°. The transition model chosen was γ-Re_θ.

Figure 3.2 shows the influence of the first cell height, in terms of y+, in lift and drag values of the S1223. For y+ values lower than unity, practically no difference was reported in the aerodynamic coefficients. This might be a good indicative that the flow was properly resolved within the boundary layer. However, domains with y+ values too small (< 0,1) required many more iterations to converge to a solution, increasing the computational cost. Thus, a domain with y+ ranging from 0,1 to 1 shall be a proper choice.

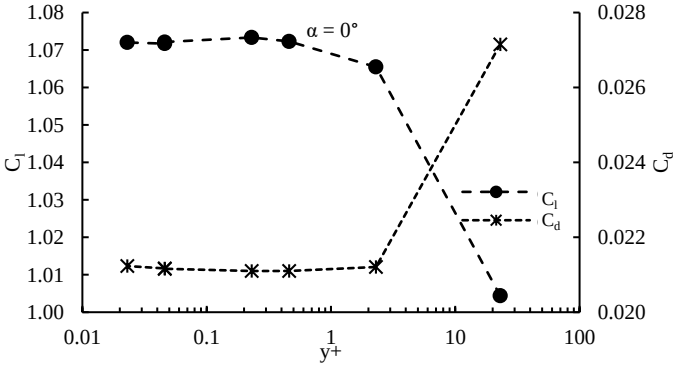

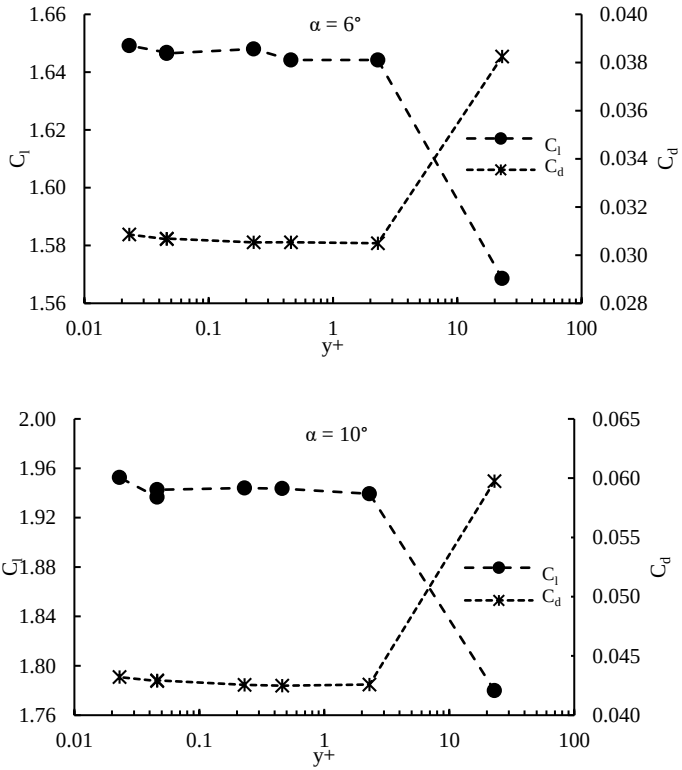

Figure 3.2 – y+ influence in lift and drag coefficient of the S1223. ($Re = 2 \cdot 10^5$)

It is also common to plot grid influence as function of the total number of cells, as seen in Figure 3.3. For each grid, the height of the first cell adjacent to the airfoil wall was also refined as the total cell count increased. For grids with a total number of cells higher than 200 000, little changes were observed in the aerodynamic coefficients.

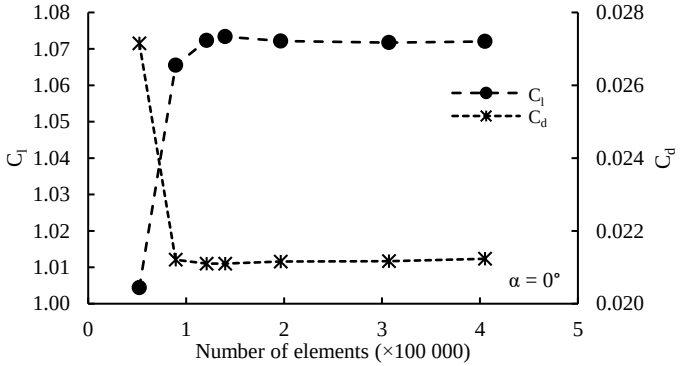

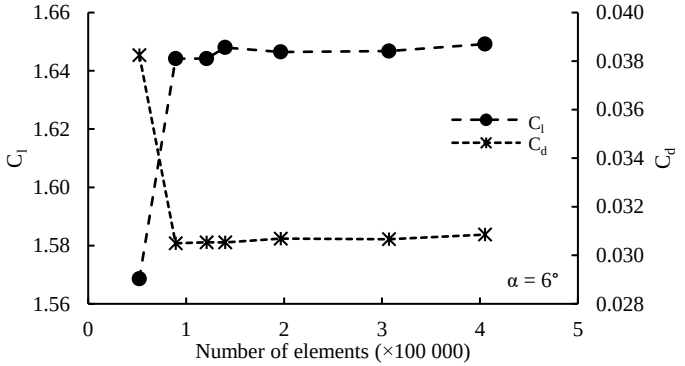

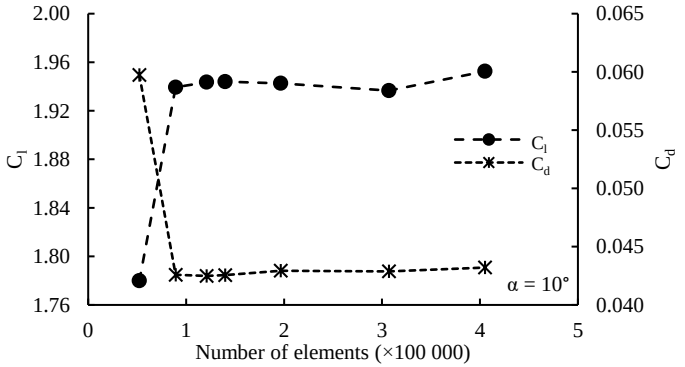

Figure 3.3 – Grid influence in lift and drag coefficients of the S1223. ($Re = 2 \cdot 10^5$)

This analysis was also performed for the cases containing the Eppler 387 airfoil and similar results were achieved.

These results made the grid choice possible. Thus, the grids chosen in this work have over 200 000 elements, the height of the first adjacent to the airfoil was set to $2 \cdot 10^{-5}$ chord length and a growth factor of 1,1. This resulted in a y+ value lesser than 1. Figure 3.4 to Figure 3.6 illustrate the meshes for S1223 and E387 freestream cases.

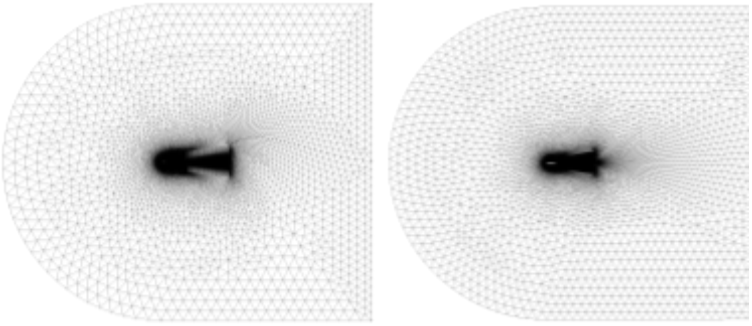

Figure 3.4 – Freestream mesh of the S1223 (left) and E387 (right).

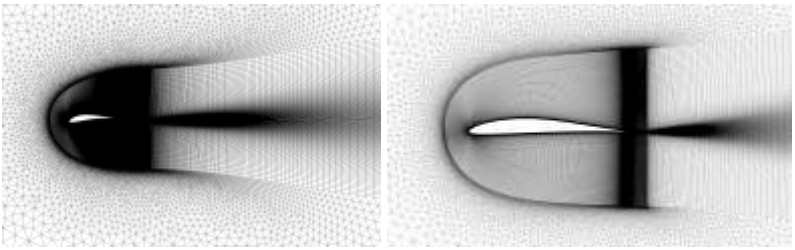

Figure 3.5 – Detail of transition from structured to unstructured grid. S1223 (left) and E387 (right).

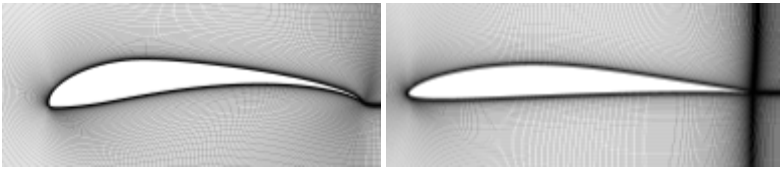

Figure 3.6 – Detail of the mesh around the airfoil. S1223 (left) and E387 (right).

3.4 Wind Tunnel Domain

The wind tunnel used in this work is located at the Laboratory of Thermal Science (LabTERMO) at UFSC. Its geometry was reproduced in a CAD software to allow the mesh generation. The domain and boundary conditions are shown in Figure 3.7.

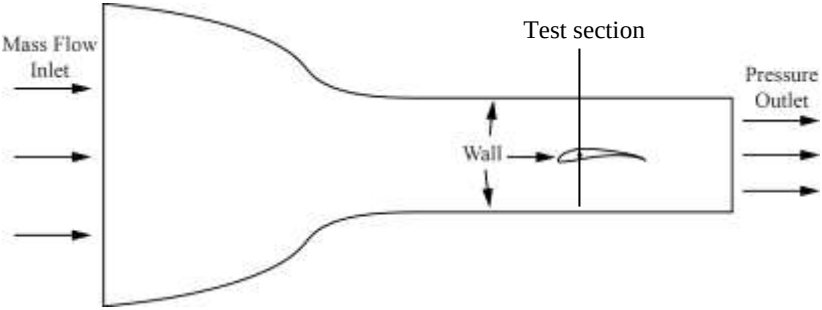

Figure 3.7 – Wind tunnel domain and boundary conditions.

A mass flow condition was set on the inlet. Its value is chosen so that the desired velocity is achieved in the test section. The outlet was set to a zero static pressure. All other surfaces were set to walls.

First, a structured mesh with no airfoil inside (Figure 3.8) was generated in the tunnel. The purpose of that is to evaluate the velocity profile at the test section, as shown in Figure 3.9. The results show that the velocity profile is not perfectly constant throughout the test section. However, in the middle region (where the airfoil will be located) the velocity difference is less than 2 %, which makes this domain suitable for the wind tunnel simulation analysis.

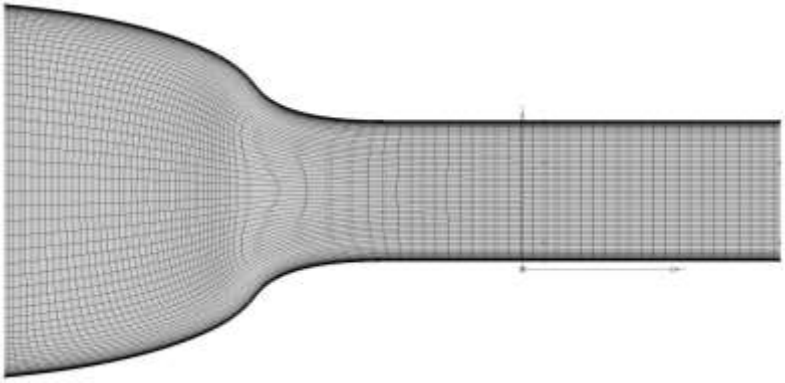

Figure 3.8 – Wind tunnel mesh with no airfoil inside.

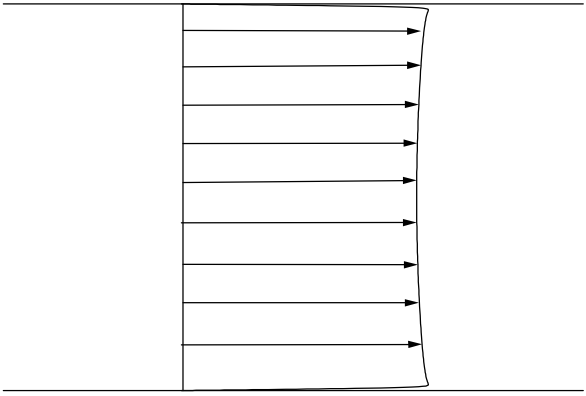

Figure 3.9 – Example of velocity profile at the test section.

In order to keep the same y^+ value and mesh characteristics of the freestream cases, the same structured mesh in the region close to the airfoil was blended in the wind tunnel mesh. An unstructured region was added to make the transition between the meshes of the airfoil and wind tunnel. In contrast to freestream cases, a single mesh had to be generated for each angle of attack of the airfoil. Figure 3.10 and Figure 3.11 illustrate an example of wind tunnel mesh for the Eppler 387. The same process was used in the S1223 cases.

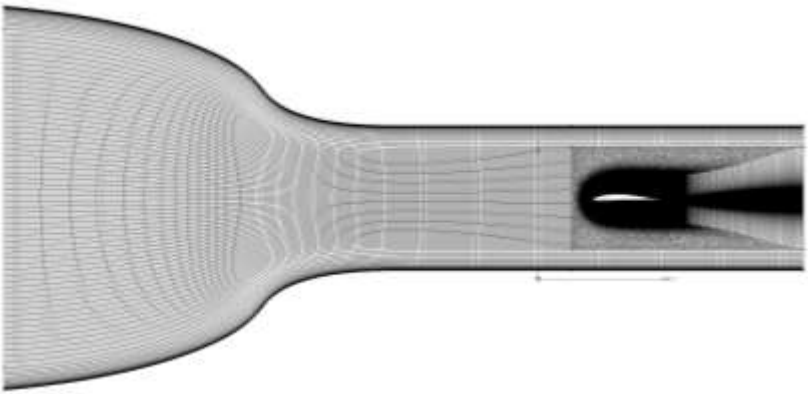

Figure 3.10 – Wind tunnel mesh for the Eppler 387. ($\alpha = 0°$)

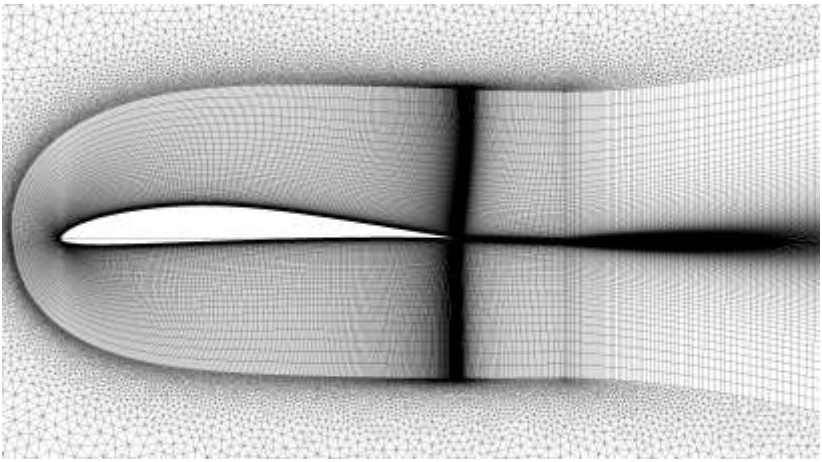

Figure 3.11 – Detail of the mesh around the Eppler 387. ($\alpha = 0°$)

3.5 Flow Solver and Convergence Criteria

The commercial RANS-based code Fluent was used in this study. Each simulation starts the running process using first order upwind discretization in space and the segregated pressure-velocity coupling SIMPLE scheme. This configuration runs for 300 iterations. Then, the SIMPLE scheme is replaced by a coupled pressure based algorithm and the case runs for more 2000 iterations. Finally, all spatial discretization

schemes are switched for the second order upwind, which is more accurate, and the running process continues for more 6000 iterations or until all scaled residuals reach a value of 10^{-6} or less. Figure 3.12 gives an example of the convergence history for the scaled residuals and Figure 3.13 for the lift and drag coefficient.

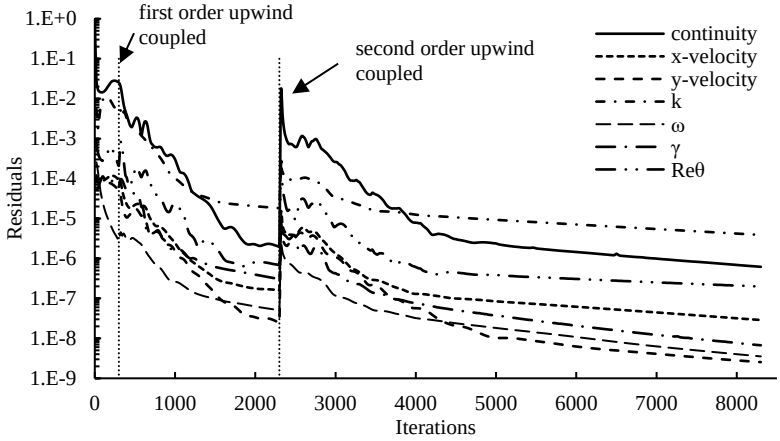

Figure 3.12 – Example of the convergence history for the scaled residuals. (S1223, γ-Reθ model, α = 6°, Re = $2 \cdot 10^5$)

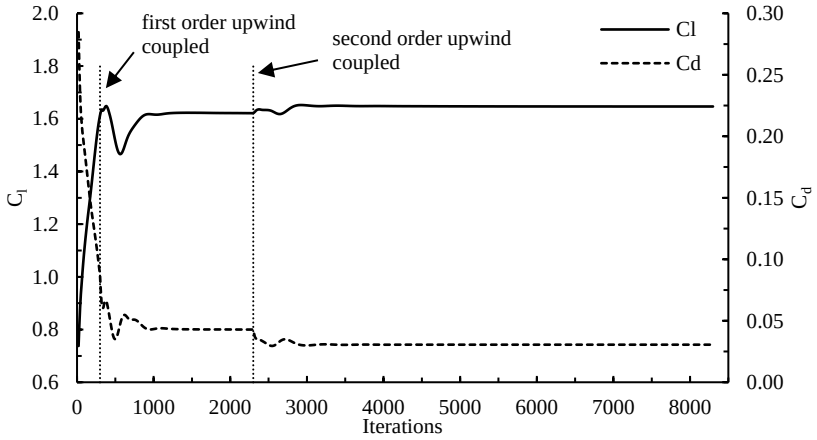

Figure 3.13 – Lift and drag coefficient during convergence process. (S1223, γ-Reθ model, α = 6°, Re = $2 \cdot 10^5$)

As seen in Figure 3.13, lift and drag coefficient have already converged at residuals of 10^{-6}.

3.6 Influence of Freestream Turbulence Intensity

When setting boundary conditions for the simulated cases, it is important to analyze the influence of freestream turbulence intensity on case results. Therefore, test cases were run for different values of turbulence intensity Tu. The transition model chosen for this analysis was the transition SST. All cases were run for an angle of attack of 0° and Reynolds number of $3 \cdot 10^5$.

Figure 3.14 shows lift and drag coefficients the tested cases. Although lift and drag presented changes in their values, C_d was more affected. C_l reported a maximum relative difference in their values of 2% while C_d reported 32%. The results below suggest that friction drag may be strongly influenced by freestream turbulence levels.

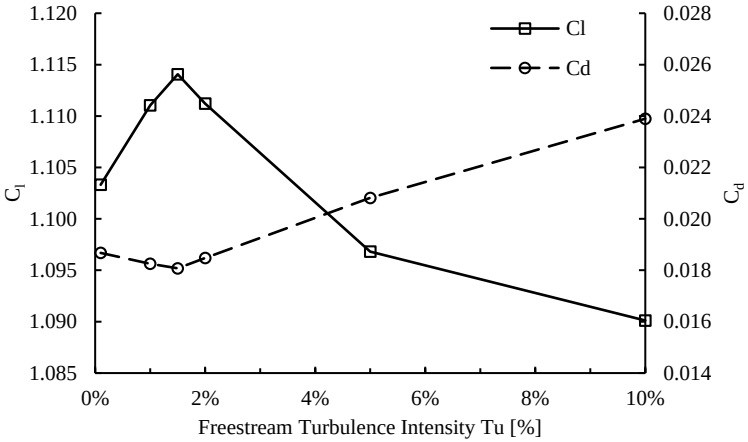

Figure 3.14 – Lift and drag coefficients for different levels of Tu. ($Re = 3 \cdot 10^5$, $\alpha = 0°$)

Pressure coefficients for different levels of turbulence intensity are shown in Figure 3.15. It can be seen on the C_p curves that the laminar separation bubble was attenuated as turbulence level increased. This behavior was mentioned by Walraevens and Cumpsty (1993). For a turbulence intensity of 5%, the pressure coefficient curve showed practically no evidence of the presence of LSB.

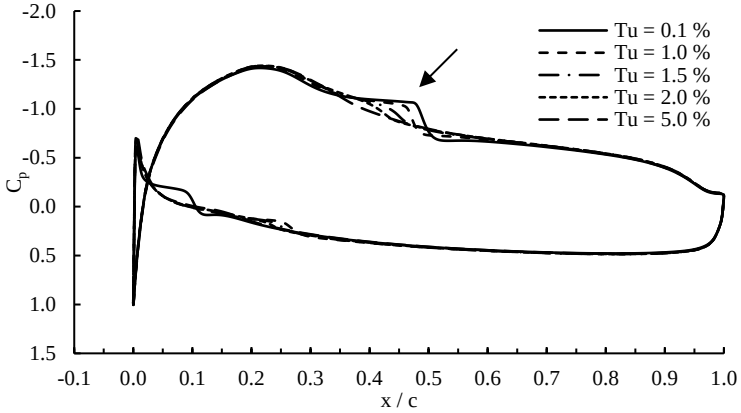

Figure 3.15 – Pressure coefficient for different levels of Tu. ($Re = 3 \cdot 10^5$, $\alpha = 0°$)

Figure 3.16 presents skin friction coefficients for different levels of turbulence intensity. As turbulence increased, the range of negative values decreased which means that bubble length also shortened. For Tu = 5%, the absence of negative C_f indicates that no separated flow transition occurred, i.e. no bubble was formed and transition might have occurred through the natural or bypass process.

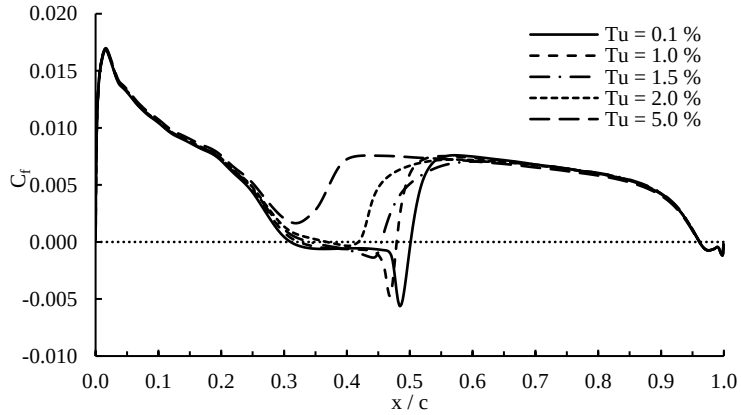

Figure 3.16 – Skin friction coefficient on the suction surface of the S1223. ($Re = 3 \cdot 10^5$, $\alpha = 0°$)

In order to complete the analysis, Figure 3.17 shows velocity profiles on the suction surface at x/c = 0,45. At this location, negative velocity values are reported for turbulence intensities of 0,1% and 1,0%. For Tu = 1,5%, no negative values were detected but the velocity gradient in y-direction is still small. For turbulence levels of 2,0% and 5,0%, the velocity profile seems to be fully turbulent.

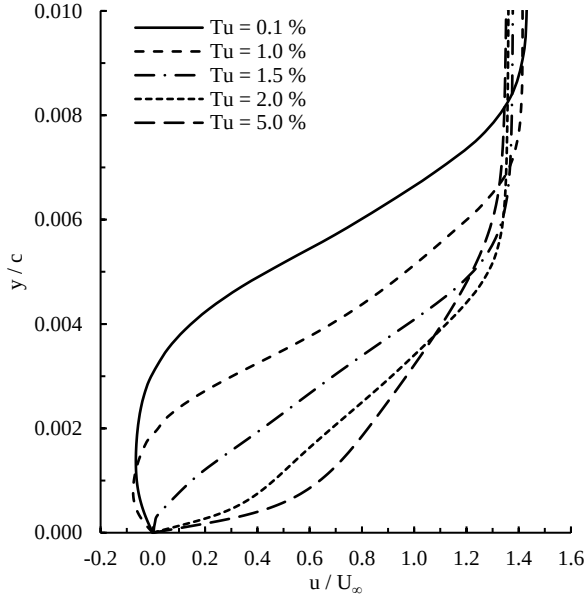

Figure 3.17 – Velocity profiles on the suction surface of the S1223 at x/c = 0,45. ($Re = 3 \cdot 10^5$, $\alpha = 0°$)

Results reported above indicated that freestream turbulence intensity has in fact a great effect on solution. Spalart and Rumsey (2007) suggest the use of a turbulence intensity value as close as 0,1%. Since the references used in this work provided aerodynamic data obtained from wind tunnels with turbulence levels close to 1%, in the following cases, unless stated, freestream turbulence intensity at the inlet boundary condition will be set to 1,0%.

4 NUMERICAL RESULTS

4.1 Freestream

4.1.1 Eppler 387

Experimental data from the Langley Low-Turbulence Pressure Tunnel (LTPT) (McGhee et al. 1988) and University of Illinois at Urbana-Champaign (UIUC) (Selig et al. 1995) were used for comparison purposes. Figure 4.1 and Figure 4.2 show lift and drag coefficients for Re = $2 \cdot 10^5$ and Re = $3 \cdot 10^5$.

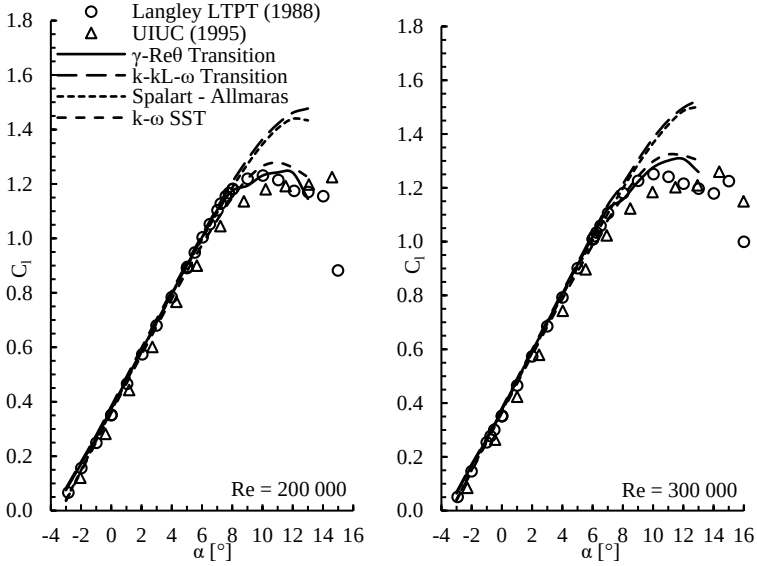

Figure 4.1 – Numerical and experimental lift values for the Eppler 387.

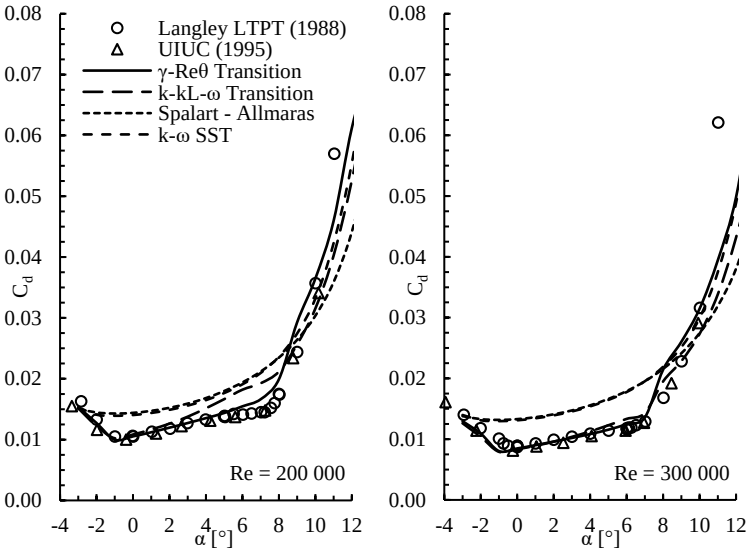

Figure 4.2 – Numerical and experimental drag values for the Eppler 387.

All models closely matched the experimental reference in the linear region of the lift coefficient curve. The k-ω SST and γ-Re_θ presented minor discrepancies but reasonably predicted stall behavior while the Spalart-Allmaras and the k-k_L-ω yielded higher values for both lift and stall angle. Slightly higher maximum lift values were achieved for the Reynolds number of $3 \cdot 10^5$. Nevertheless, one should emphasize that convergence became poorer as the angles of attack got closer to the stall region. Regarding the drag coefficient, the poor capability of the fully turbulent models in predicting laminar-to-turbulent transition became evident. Large differences in C_d values were observed at angles of attack from -1º to 8º. These differences were accentuated as the Reynolds increased to $3 \cdot 10^5$. The better agreement reported by transition-sensitive models can be explained by the presence of laminar boundary layers over a considerable region of the wing which decreases friction drag. At angles higher than 8º, turbulent boundary layer prevails and all models presented similar trends. Overall, due to the better agreement to the LTPT data, the γ-Re_θ transition-sensitive model seems to perform better than the others when both lift and drag are concerned.

Figure 4.3 and Figure 4.4 show the pressure coefficient distributions for all models in comparison with the Langley LTPT results. At $\alpha = 0°$ and $\alpha = 4°$ one can see a hump in the portion between x/c = 0.4

to x/c = 0.8 predicted only by the transition-sensitive models. This hump is compounded of a flat portion followed by a sudden jump on C_p values of the suction surface which is an indicative of a separation bubble. With the increase of the Reynolds number, this portion shrinked. For $\alpha = 8°$, fully turbulent models resulted in better agreement with the experimental data. At this angle, both the γ-Re_θ and the k-k_L-ω forced a laminar-to-turbulent transition near the leading edge but the reference seems to indicate that the boundary layer is already turbulent. For this case, the k-ω SST and the Spalart-Allmaras agreed more closely to the experimental points. It should be noted that this forced transition may have occurred since the numerical case constitutes an ideal flow condition with perfect smooth walls, which is hardly achieved in experimental analysis.

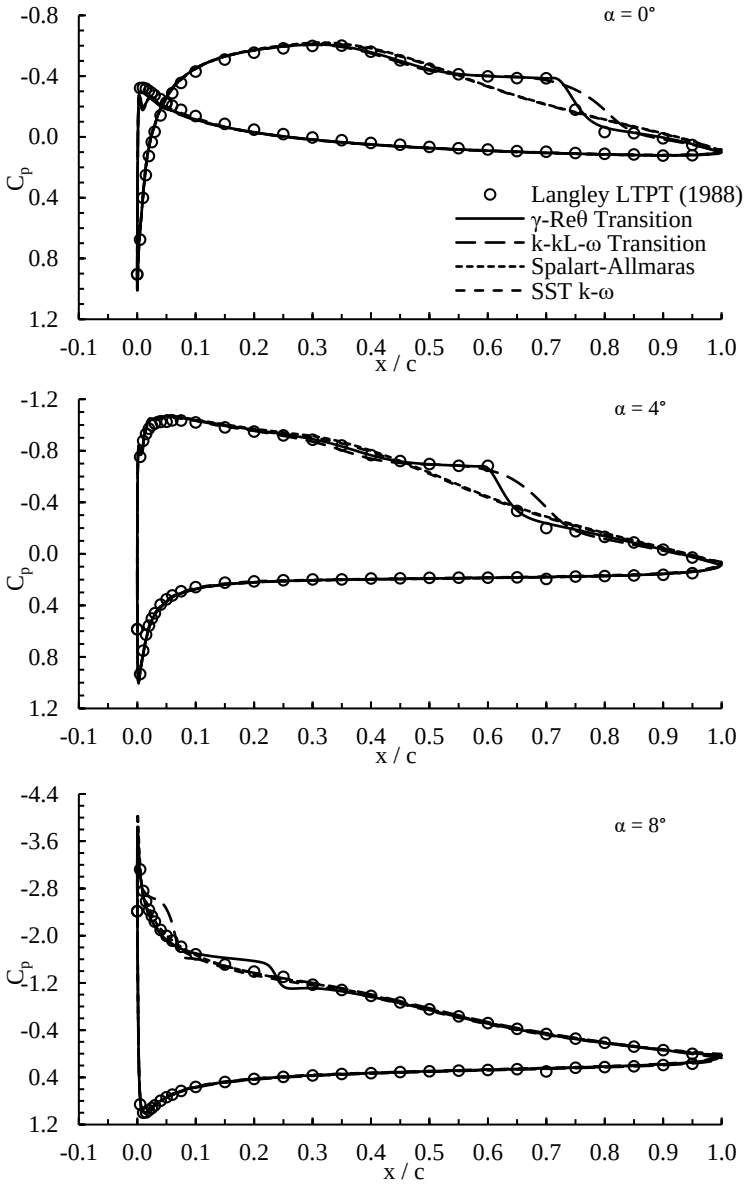

Figure 4.3 – Numerical and experimental pressure distribution over the Eppler 387 ($Re = 2 \cdot 10^5$).

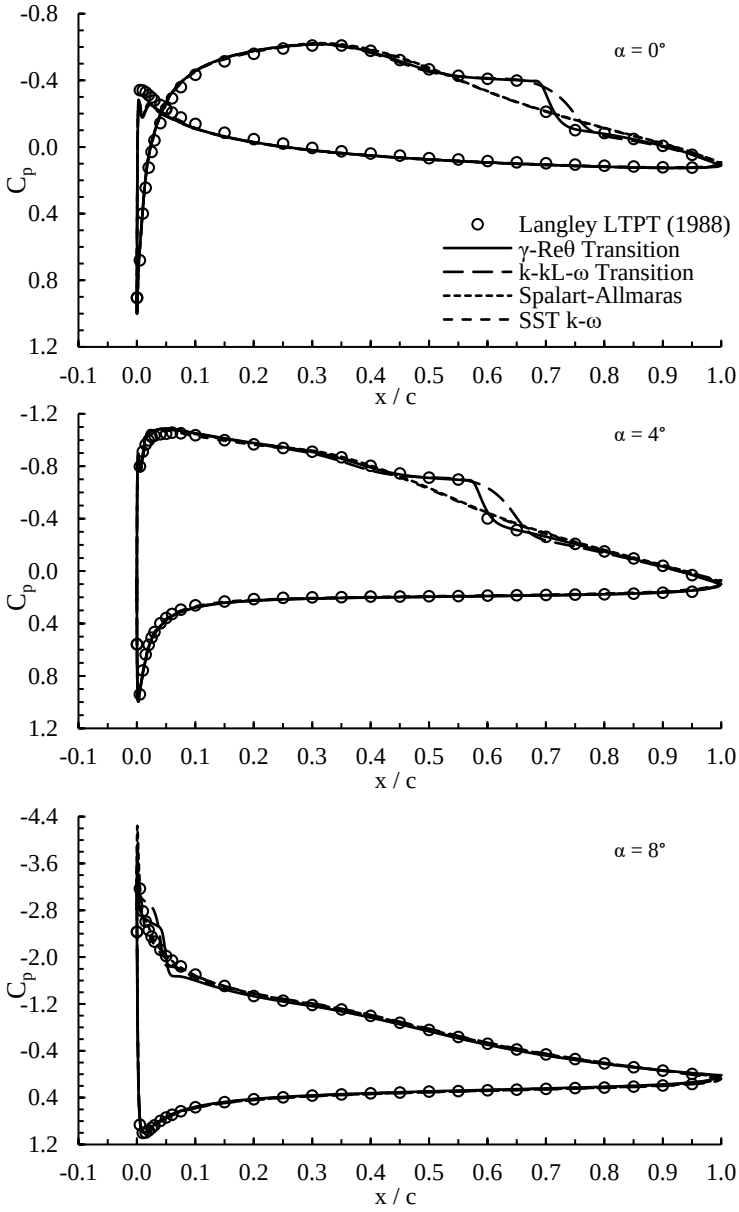

Figure 4.4 – Numerical and experimental pressure distribution over the Eppler 387 ($Re = 3 \cdot 10^5$).

Numerical skin friction results on the suction surface at $\alpha = 4°$ are given in Figure 4.5. Negative C_f values point out the separation, location and extent of the separation bubble. As expected, transition-sensitive models presented lower C_f values in the first portion of the airfoil indicating the presence of laminar boundary layer. The k-k_L-ω predicted a larger separation bubble.

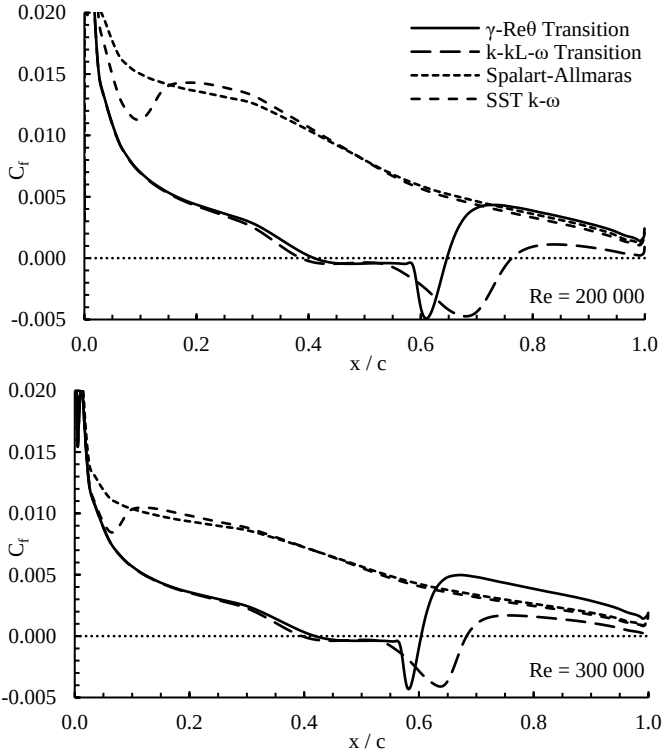

Figure 4.5 – Numerical skin friction coefficient on suction surface of the Eppler 387 ($\alpha = 4º$).

Figure 4.6 compares the numerical separation and reattachment locations with experimental data from LTPT. Both transition-sensitive models correctly predicted the laminar separation point. The only major discrepancy was the reattachment point predicted by the k-k_L-ω model since its values were relatively larger than the reference.

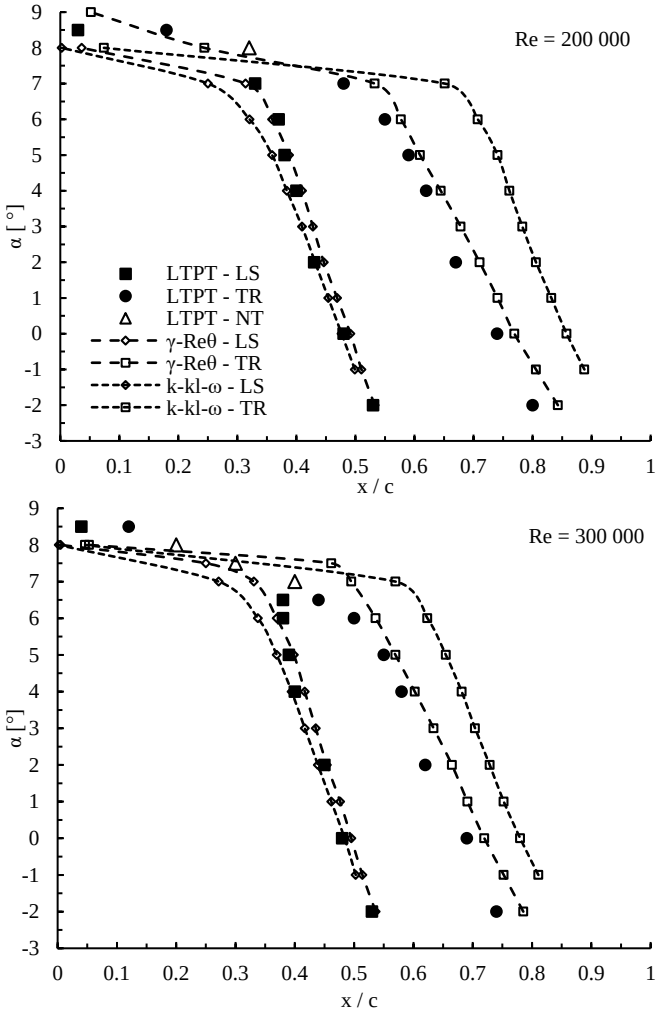

Figure 4.6 – Numerical and experimental separation and reattachment points (LS – Laminar separation; TR – Turbulent reattachment; NT – Natural transition).

Figure 4.6 can also be used to evaluate bubble length by estimating the region between separation and reattachment points. For instance, at $\alpha = 2^{o}$ and with the increase in Reynolds from $2 \cdot 10^5$ to $3 \cdot 10^5$, the laminar separation point given by the γ-Re_θ moved from x/c = 0,45 to x/c = 0,46

and the reattachment point from x/c = 0,71 to x/c = 0,66. This resulted in a decrease in bubble length from 26 % to 20 % chord length. Similar trends were observed for all angles of attack in both transition models.

Figure 4.7 shows the numerical velocity profiles on the suction surface at three chordwise locations (Figure 4.8). At $\alpha = 4°$ and x/c = 0,25, one can clearly see that transition-sensitive models predict a laminar-like boundary layer. The smaller velocity gradient for these models near the wall resulted in lower C_f values as shown in Figure 4.5. Moving to x/c = 0,50, reverse velocity profiles confirm the presence of a separation bubble. Both fully turbulent models were not able to generate laminar profile nor separation bubble. At the x/c = 0,75 location, although all profiles presented a turbulent boundary layer shape, transition-sensitive models showed a distinct velocity pattern. There is a sharp change in the velocity profile as indicated by the arrows. This behavior may be consequence of the presence of a separation bubble upstream since the same does not occur in the fully-turbulent models.

At $\alpha = 8°$, all models showed turbulent velocity profiles suggesting that transition to turbulent may have occurred prior to x/c = 0,25. At this angle, all models presented similar behaviors but with slight differences characterizing their own singularities.

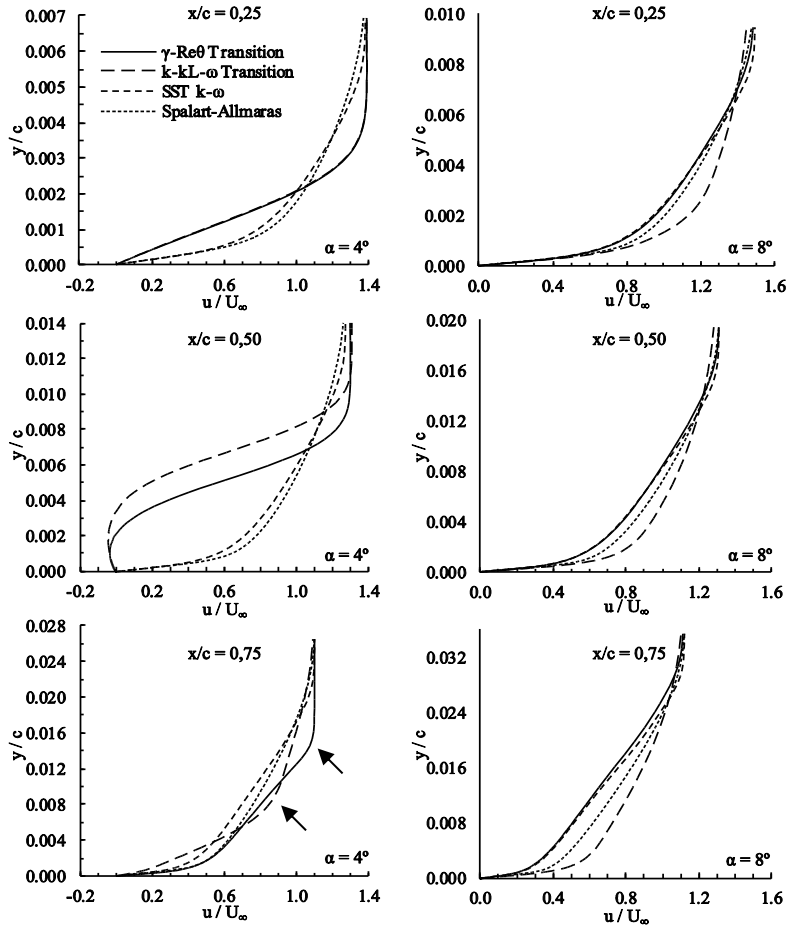

Figure 4.7 – Numerical velocity profiles on the suction surface of the Eppler 387 ($Re = 3 \cdot 10^5$).

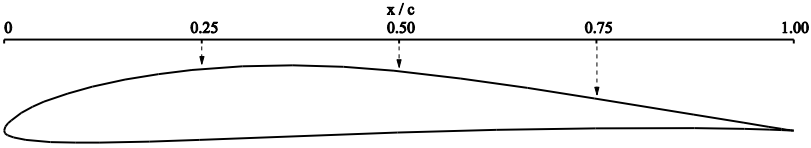

Figure 4.8 – Eppler 387 chordwise locations where velocity profiles were evaluated.

To complete the previous analysis, contours of velocity magnitude and streamlines are shown in Figure 4.9. LSB can be clearly identified for

the cases that used the transition-sensitive models. They are identified by the dark blue region over the upper surface of the airfoil, indicating a region of stagnated flow. As mentioned earlier, the k-k_L-ω implied in a larger bubble than the γ-Re_θ. The separation bubble also contributed by making the fluid flow through a different region than it would if no bubble was formed. The result is an increase in the effective thickness of the airfoil at that portion, which may lead to differences in lift, drag, pressure and friction of the airfoil.

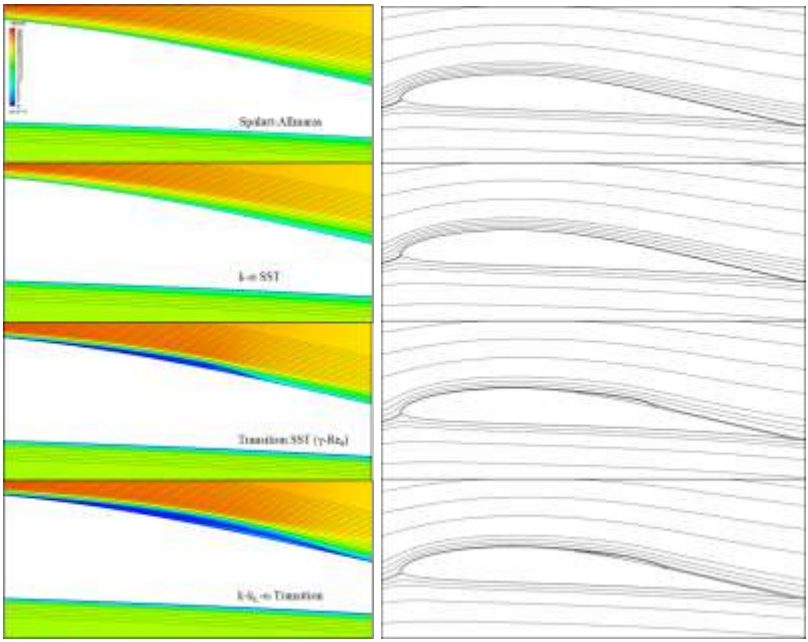

Figure 4.9 – Contours of velocity magnitude and streamlines over the Eppler 387 ($Re = 3 \cdot 10^5$, $\alpha = 4^o$).

It is also interesting to analyze the velocity profiles in connection with friction coefficient C_f (Figure 4.10) and pressure coefficient C_p (Figure 4.11). Flow over the airfoil presents three different patterns: laminar, transitional and turbulent, which can be inferred from the velocity profile shapes. Within the bubble, two main characteristics can be associated: reversed flow which implies in negative or close C_f values and a constant pressure region followed by a sudden jump in C_p values when the flow becomes turbulent.

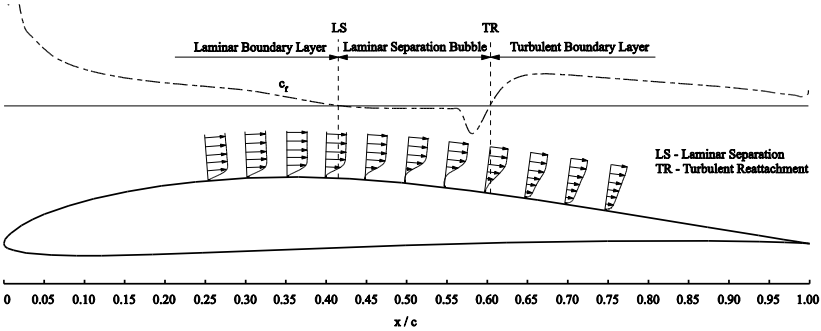

Figure 4.10 – Friction coefficient and velocity profiles on the suction surface of the Eppler 387. (Re = $2 \cdot 10^5$, $\alpha = 4°$, Turbulence model: γ-Re$_\theta$)

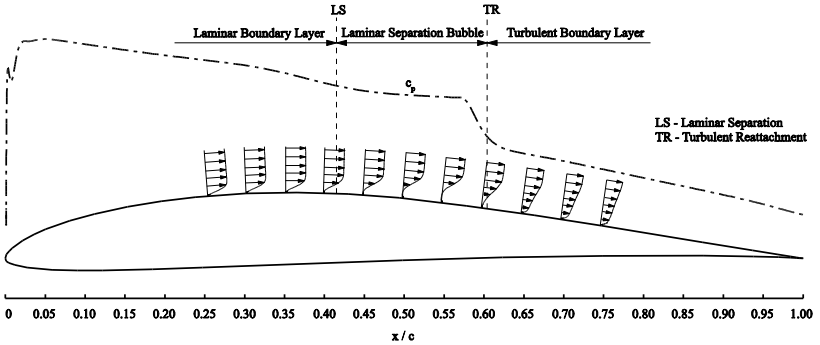

Figure 4.11 – Pressure coefficient and velocity profiles on the suction surface of the Eppler 387. (Re = $2 \cdot 10^5$, $\alpha = 4°$, Turbulence model: γ-Re$_\theta$)

4.1.2 S1223

For this airfoil, the only experimental data found was from the University of Illinois at Urbana-Champaign (UIUC) (Selig, *et al.* 1995). Figure 4.12 and Figure 4.13 show lift and drag coefficients for Re = $2 \cdot 10^5$ and Re = $3 \cdot 10^5$.

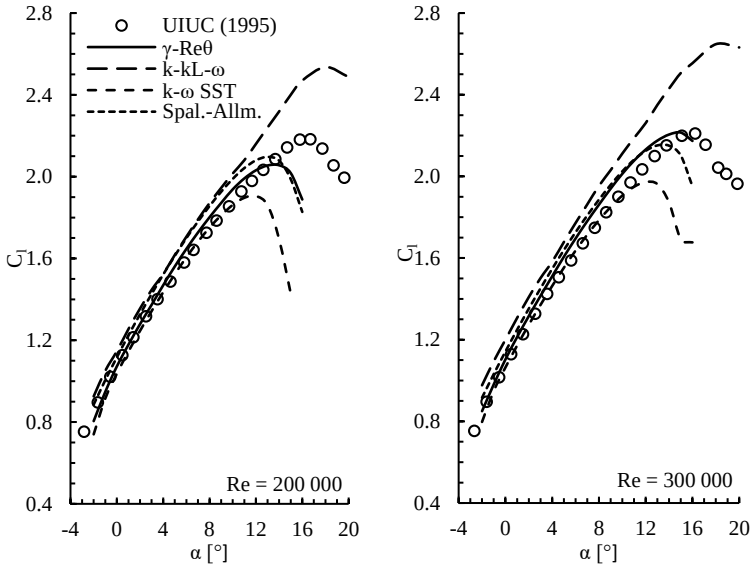

Figure 4.12 – Numerical and experimental lift values for the S1223.

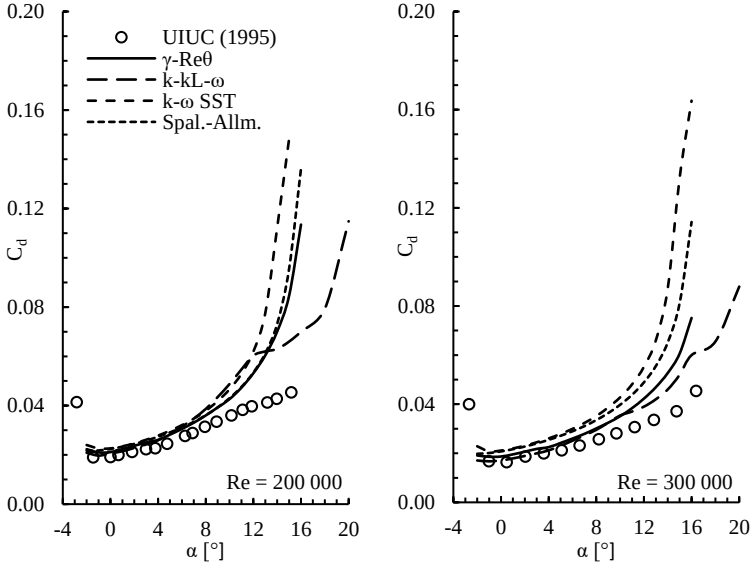

Figure 4.13 – Numerical and experimental drag values for the S1223.

For the lift coefficient results, although all models presented similar trends at angles from -2º to 8º, their values showed minor differences.

At Reynolds of $2 \cdot 10^5$, none of them was able to accurately predict the stall according to the reference. Only the γ-Re_θ showed better stall agreement at a Reynolds number of 300 000. The k-k_L-ω yielded higher values for lift along the entire curve. For this model, convergence could not be achieved for angles higher than 20º. For the fully-turbulent models, the k-ω SST reported lower values for lift and stall angle compared to the others while the Spalart-Allmaras presented similar behavior to the γ-Re_θ. Regarding drag coefficient, at Reynold of $2 \cdot 10^5$, all numerical C_d values were higher than the reference. For Re = $3 \cdot 10^5$, the differences in values obtained by the fully-turbulent models were accentuated, which may be resulted from the high friction drag produced by the turbulent boundary layer. One should note that drag data from the UIUC (1995) was taken by the momentum method instead of a force balance, which consists in measuring the wake generated by the airfoil. At Re = $2 \cdot 10^5$, it showed a linear region at angles from 6º to 15º. This behavior is not common in airfoils approaching stall. Overall, the γ-Re_θ transition-sensitive model seems to perform better than the others when both lift and drag are concerned.

Figure 4.14 and Figure 4.15 show only the numerical pressure coefficient distributions since no experimental C_p data for these cases could be found at that time. At $\alpha = 0°$ and $\alpha = 4°$ one can see a hump on the C_p curve in the portion between x/c = 0.35 to x/c = 0.55 predicted only by the transition-sensitive models. This hump moved towards the leading edge as the the angle of attack increased, shrinked as the Reynolds number increased and was smoother in the k-k_L-ω curves.

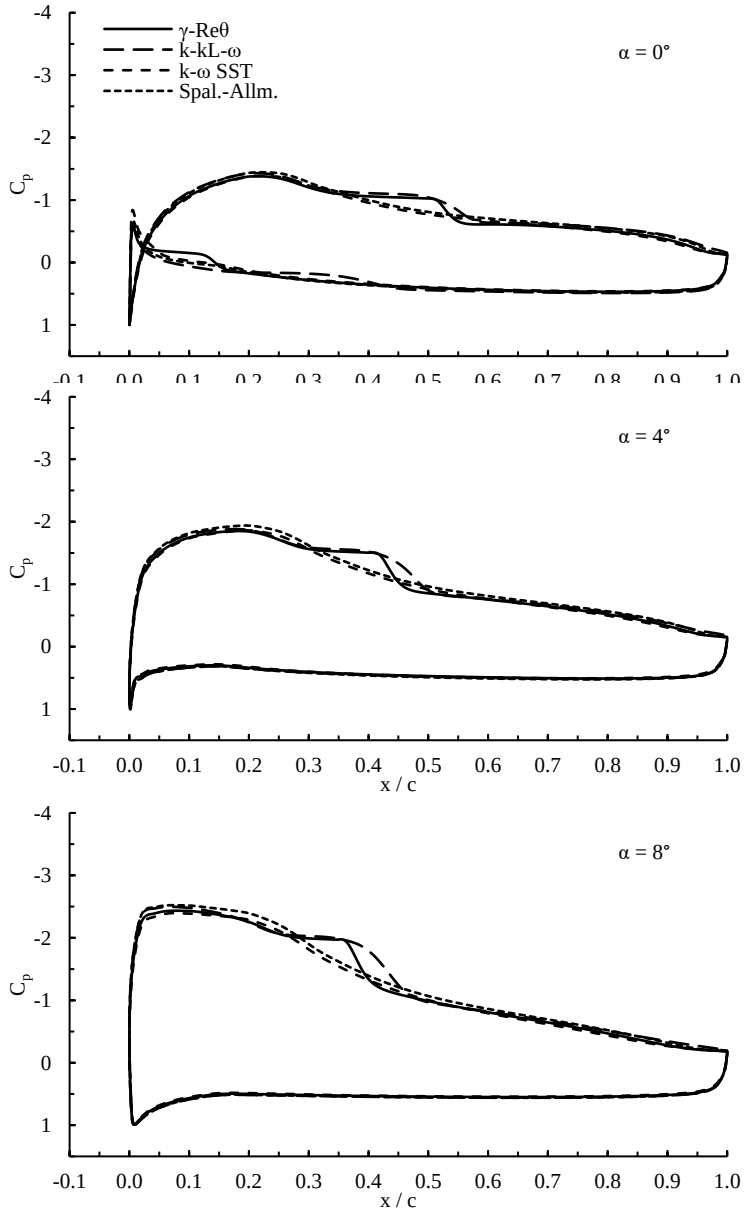
γ-Reθ
k-kL-ω
k-ω SST
Spal.-Allm.
α = 0°
α = 4°
α = 8°
Cp
x / c
-4
-3
-2
-1
0
1
-0.1
0.0
0.1
0.2
0.3
0.4
0.5
0.6
0.7
0.8
0.9
1.0

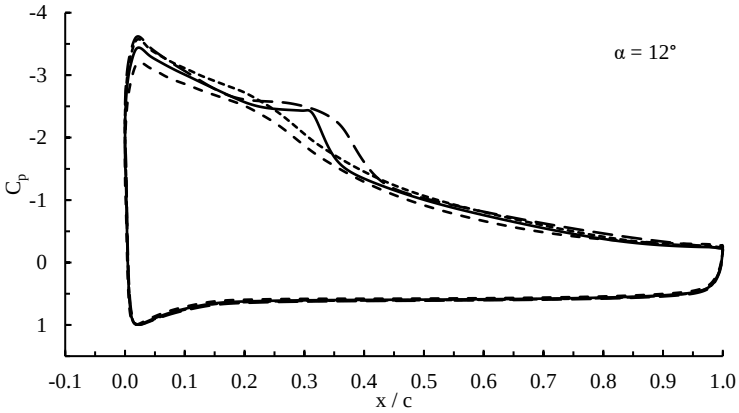

Figure 4.14 – Numerical pressure distribution over the S1223 ($Re = 2 \cdot 10^5$).

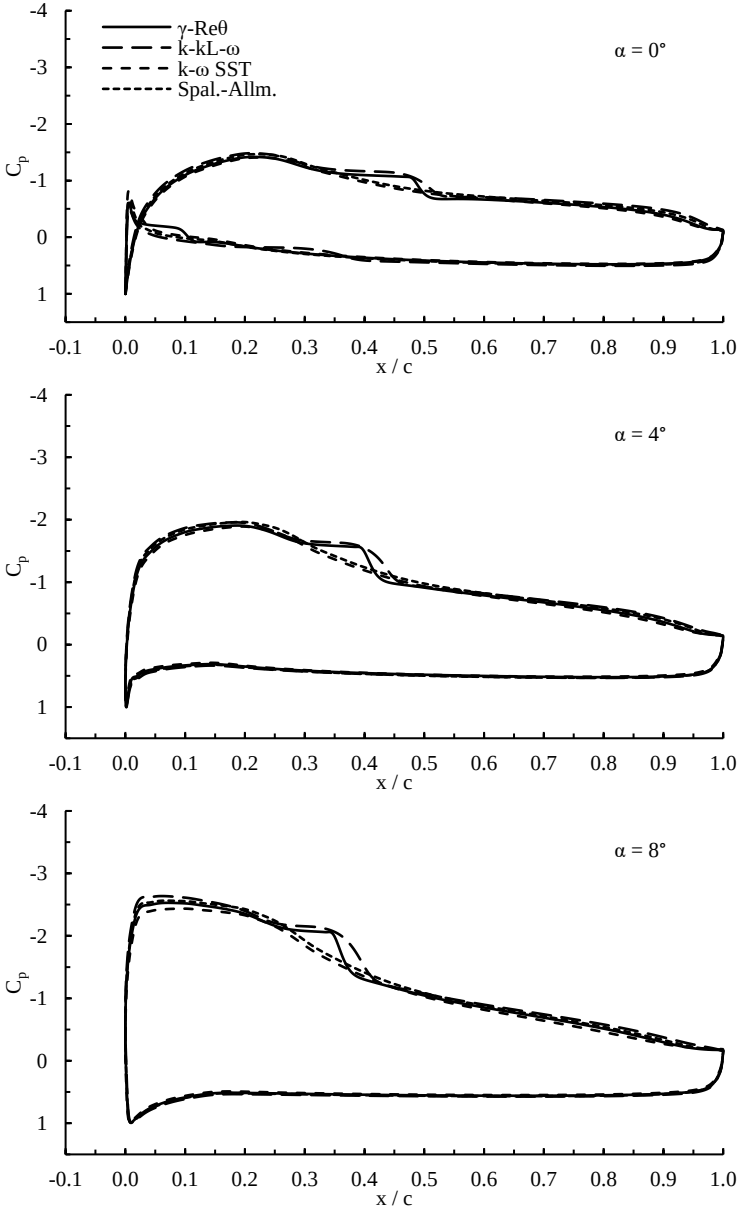
γ-Reθ
k-kL-ω
k-ω SST
Spal.-Allm.
α = 0°
α = 4°
α = 8°
C_p
x / c
-4
-3
-2
-1
0
1
-0.1
0.0
0.1
0.2
0.3
0.4
0.5
0.6
0.7
0.8
0.9
1.0

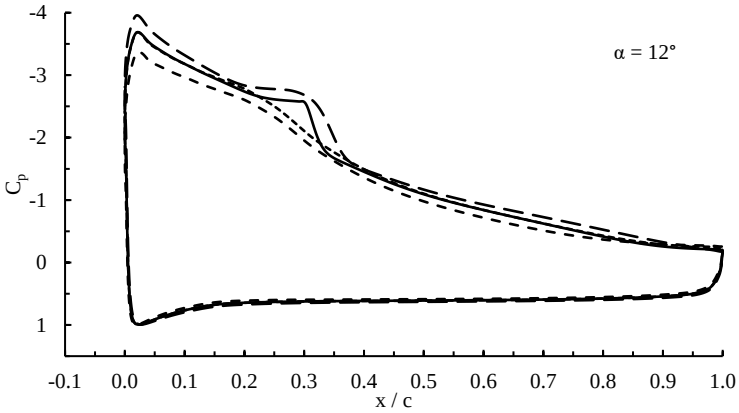

Figure 4.15 – Numerical pressure distribution over the S1223 ($Re = 3 \cdot 10^5$).

Numerical skin friction results on the suction surface at $\alpha = 4°$ are given in Figure 4.16. Negative C_f values point out the separation, location and extent of the bubble. As occurred with E387, transition-sensitive models presented lower C_f values in the first portion of the airfoil indicating the presence of laminar boundary layer. The k-k_L-ω predicted a larger separation bubble than the γ-Re_θ.

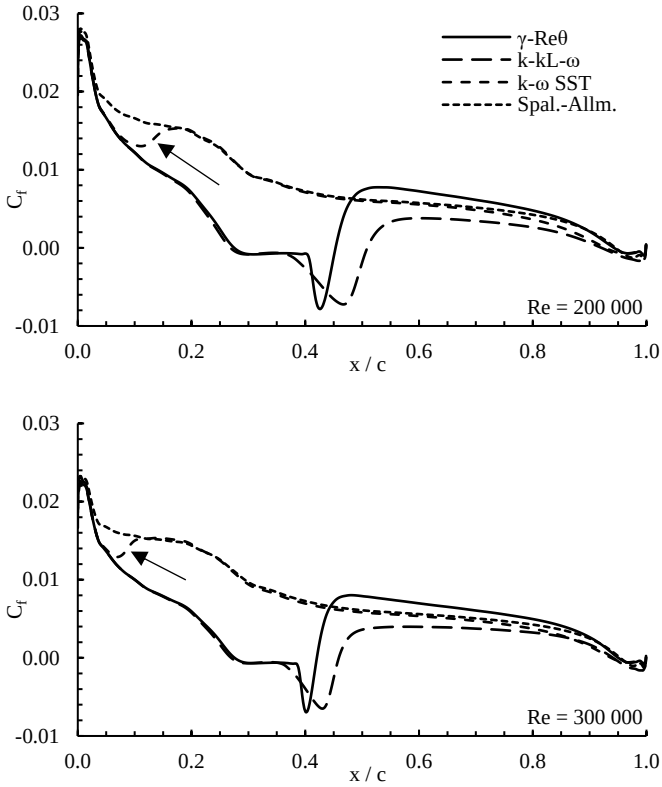

Figure 4.16 – Numerical skin friction coefficient on the suction surface of the S1223. ($\alpha = 4°$)

Indicated by the black arrows in Figure 4.16, one can see that the k-ω SST differed from the Spalart-Allmaras for x/c < 0,15. It seems that the model tried to predict a laminar boundary layer on the region close to the leading edge but rapidly changed to turbulent, matching the curve predicted by the Spalart-Allmaras. Figure 4.17 shows the velocity profiles at this location and proves that the k-ω SST velocity profile matches the one generated by the transition-sensitive models and not the Spalart-Allmaras model.

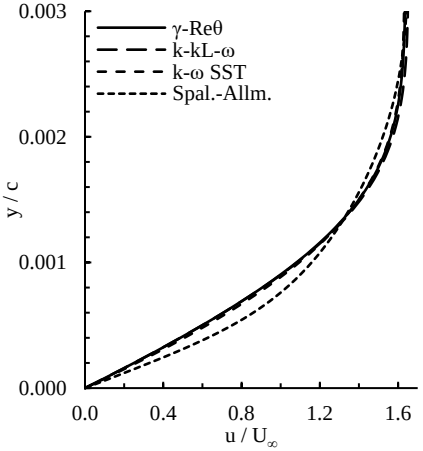

Figure 4.17 – Velocity profile on the suction surface of the S1223 at x/c = 0,09. ($\alpha = 4°$, $Re = 2 \cdot 10^5$).

Figure 4.18 gives numerical separation and reattachment locations for both transition-sensitive models. At $\alpha = -2°$, both models predicted approximately the same values for separation and reattachment locations. As the angle of attack increases, the reattachment point given by the γ-Re_θ moves towards the leading edge more rapidly than the k-k_L-ω. Only at around $\alpha = 13°$ the k-k_L-ω reattachment point changes its behavior and moves quickly towards the leading edge. As expected, bubble length diminished and moved forward as the Reynolds number increased.

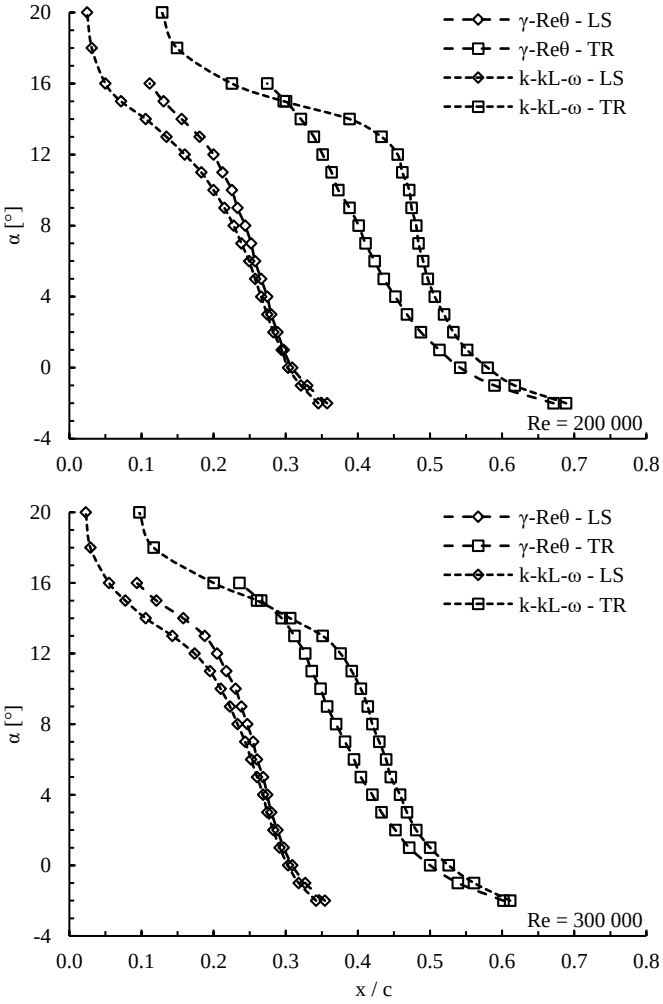

Figure 4.18 – Numerical separation and reattachment points (LS – Laminar separation; TR – Turbulent reattachment).

Figure 4.19 shows numerical velocity profiles on the suction surface at three chordwise locations (Figure 4.20). For angles of 4° and 8° and at x/c = 0,25, one can see that profiles predicted by transition-sensitive models present a much smaller velocity gradient at the wall when compared to the fully-turbulent models. This explains the lower values

for C_f shown in Figure 4.16 for this location. Moving to x/c = 0,50, the k-k_L-ω still predicts negative velocities in the region close to the wall. It presented bigger contrast in comparison to the other models for all analyzed angles and locations. At the x/c = 0,75 location, although all profiles presented a turbulent boundary layer shape, the k-k_L-ω model showed again a distinct velocity pattern. There is a sharp change in the velocity profile as indicated by the arrows. This behavior is possibly a consequence of the length and position of a separation bubble upstream the flow, as mentioned by Tain and Cumpsty (2000). Also at x/c = 0,75 location, the γ-Re_θ and k-ω SST curves were practically identical. These models behave in a similar manner for regions of turbulence which is expected since the γ-Re_θ is derived from the k-ω SST.

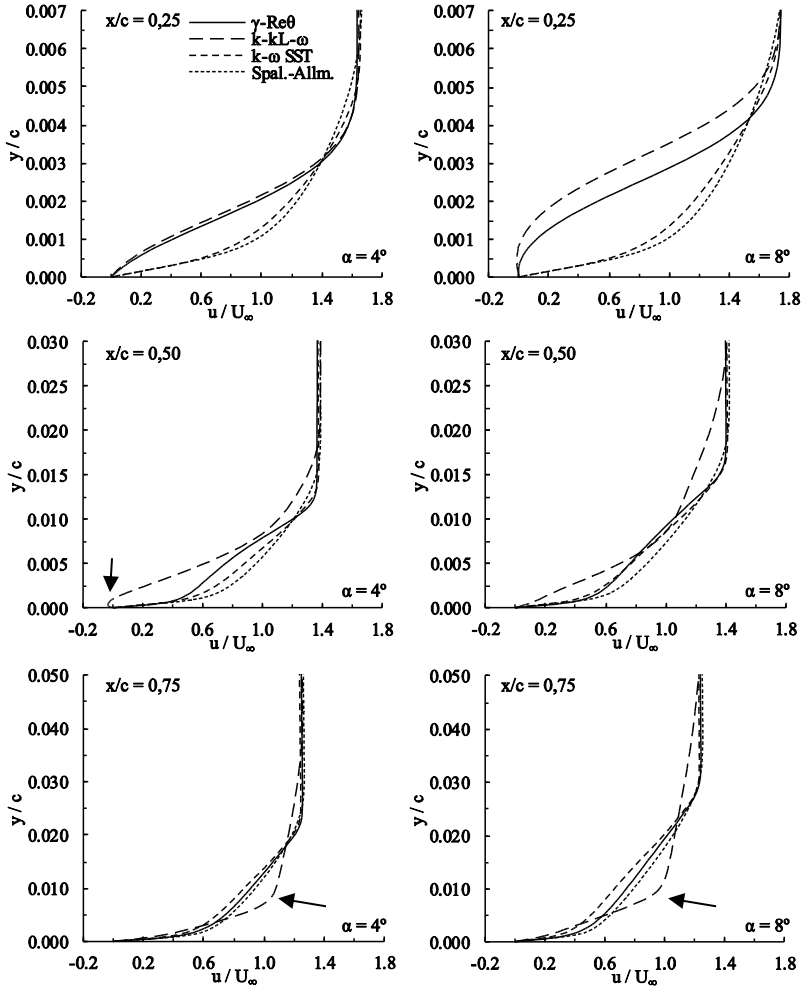

Figure 4.19 – Numerical velocity profiles on the suction surface of the S1223 ($Re = 2 \cdot 10^5$).

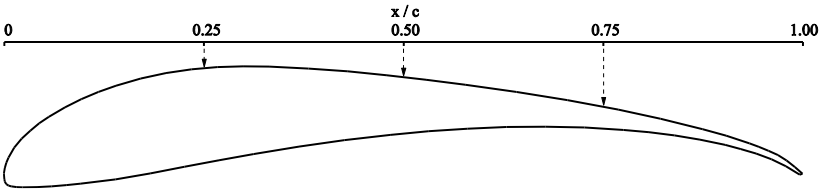

Figure 4.20 – S1223 chordwise locations where velocity profiles were evaluated.

To complete the previous analysis, contours of velocity magnitude and streamlines are shown in Figure 4.21. LSB is visibly larger for the k-k_L-ω than the γ-Re_θ.

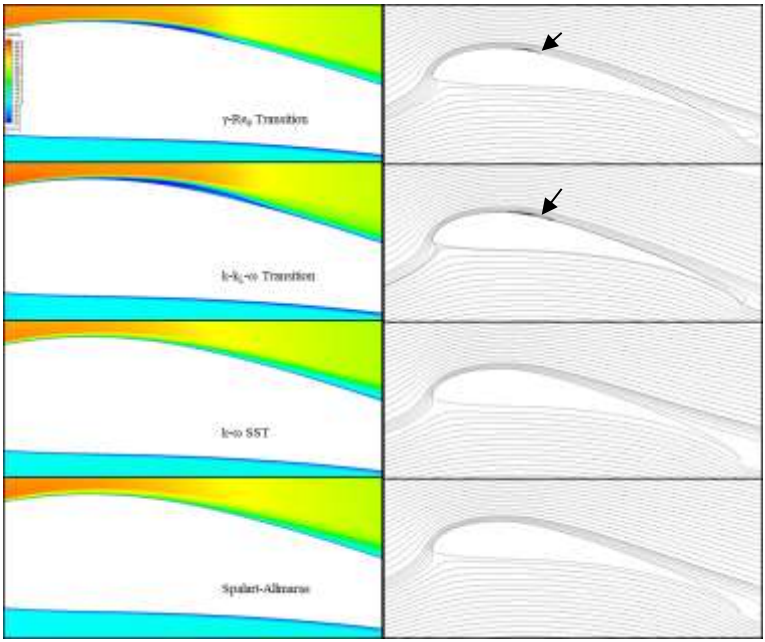

Figure 4.21 – Contours of velocity magnitude and streamlines over the S1223 ($Re = 3 \cdot 10^5$, $\alpha = 12^o$)

From all information that was presented until now, it could be observed some discrepancies between the two transition-sensitive models. These discrepancies can be attributed to the fact that each model uses a particular method to predict transition. While the γ-Re_θ uses empirical correlations, the k-k_L-ω tries to incorporate the physics of transition. To

better illustrate how each model predicts the LSB, Figure 4.22 brings the velocity profiles on different upper surface locations of the S1223.

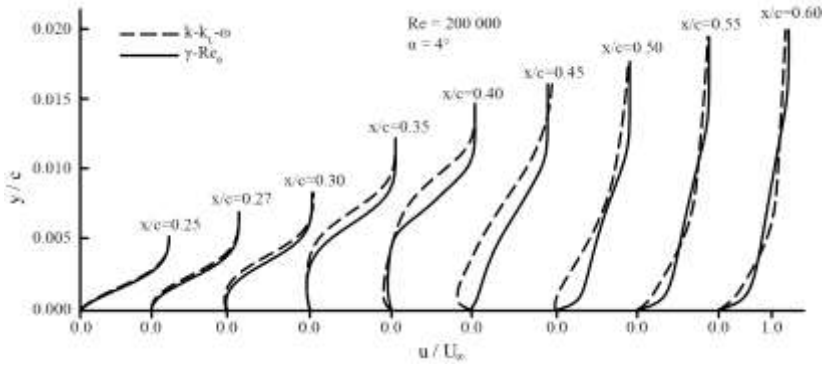

Figure 4.22 – Velocity profiles on the upper surface of the S1223.

At x/c = 0,25 both models practically predict the same laminar boundary layer. As the bubble develops, the velocity profile of the k-k_L-ω quickly starts to move away from the γ-Re_θ. The equations of the k-k_L-ω model predicts a larger and thicker bubble, which delays more to reattach the surface resulting in a thicker boundary. At x/c = 0,50, the γ-Re_θ is already attached to the surface while the k-k_L-ω is not.

It is still not possible to state which of the models predicts a solution close to reality. Thus, experimental data for this airfoil is required.

4.2 Effect of the Reynolds Number

As mentioned before, low Reynolds number airfoil flows are principally distinguished by their associated laminar separation bubbles. In past research, considerable attention has been focused on laminar separation bubbles because they are the leading culprit to the degradation in performance of airfoils at low Reynolds numbers. For the most part, the resulting pressure drag over the region of the laminar separation bubble is responsible for the relatively high drag that can sometimes accompany airfoils at low Reynolds numbers (SELIG, 2003). To illustrate how the Reynolds number affects airfoil performance, Figure 4.23 shows the lift and drag curves for the S1223 at different Reynolds numbers.

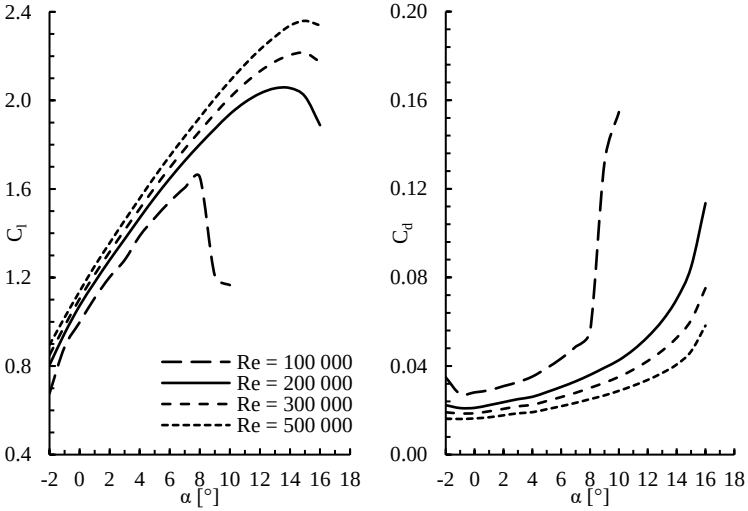

Figure 4.23 – Lift and drag coefficient curves for the S1223 airfoil at different Reynolds number. (Transition model: γ-Re_θ)

As seen in Figure 4.23, the increase in Reynolds number caused an increase in lift and decrease in drag, which is beneficial in terms of performance. In addition, stall occurred earlier and in an abrupt way at Re = $1 \cdot 10^5$, possibly caused by laminar separation bubble burst.

Drag values were higher at low Reynolds numbers. By analyzing Table 4.1, one can see that, although the viscous contribution was the lowest for Re =$1 \cdot 10^5$, pressure drag was the dominant contribution for low Reynolds. It can also be observed in Table 4.1 that pressure contribution decreases as the Reynolds increases. These results can be confirmed by analyzing the C_p curves in Figure 4.24.

Table 4.1 – Pressure and viscous drag contributions of the S1223.
($\alpha = 0°$, $Re = 1 \cdot 10^5$)

Re	Drag coefficient		
	Pressure Contribution	**Viscous Contribution**	**Total**
100 000	74.7%	25.3%	0.0281
200 000	64.5%	35.5%	0.0211
300 000	59.9%	40.1%	0.0187
500 000	55.8%	44.2%	0.0163

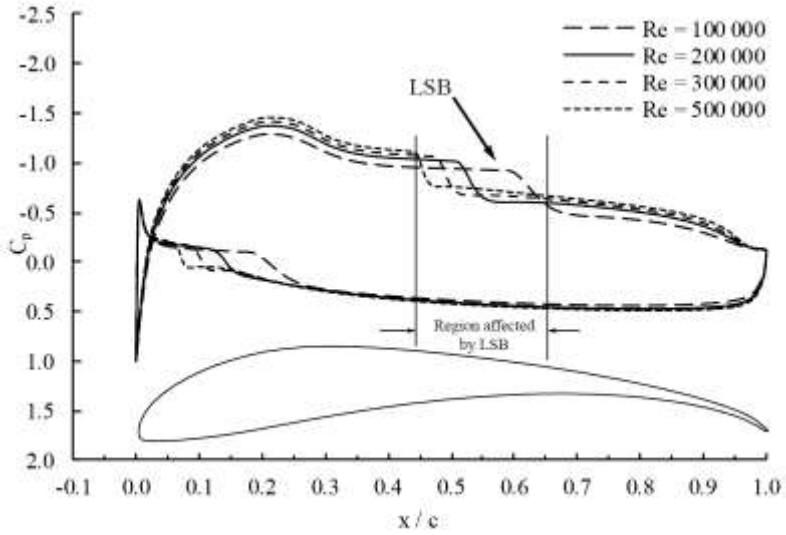

Figure 4.24 – Pressure distribution for different Reynolds numbers. ($\alpha = 0°$)

From Figure 4.24, it is seen that suction peak (low-pressure peak) increases on the upper airfoil surface as the Reynolds number increases. Also, the laminar separation bubble induces a low-pressure zone between x/c = 0,45 and x/c = 0,65 of the airfoil. The resulting pressure force acting on this location has a horizontal component that tends to pull the airfoil backwards, yielding higher values for drag. The larger the bubble length, the lower the pressure acting in this region.

Figure 4.25 shows velocity contours for the S1223 at various Reynolds numbers. It is clear that the lower the Reynolds number, the bigger the LSB. At $\alpha = 12°$ and $Re = 1 \cdot 10^5$, the separated flow may have occurred due to the burst of the LSB. This constitutes a leading-edge stall type which causes an abrupt loss of lift, as illustrated in Figure 4.23. A trailing-edge stall type is shown in Figure 4.26, where the flow reattaches the surface and then separates permanently. In this case, the LSB is not the main cause of stall.

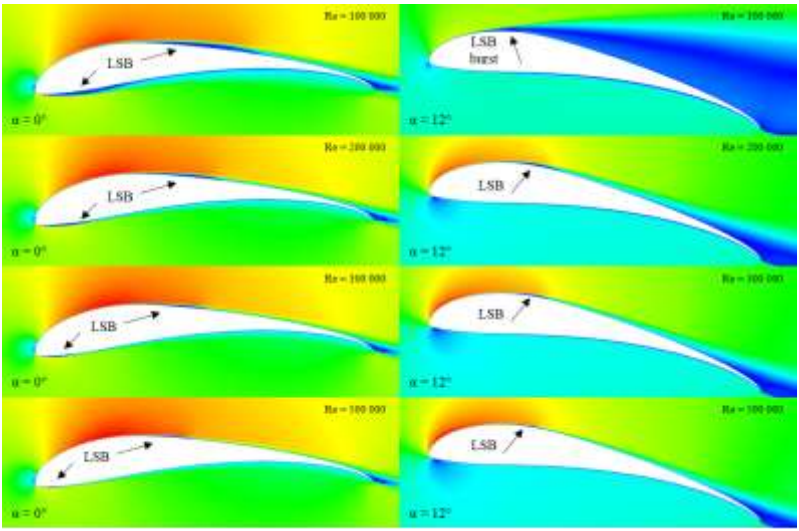

Figure 4.25 – Velocity contours for the S1223 at different Reynolds numbers. ($\alpha = 0°$, Transition model: γ-Re_θ)

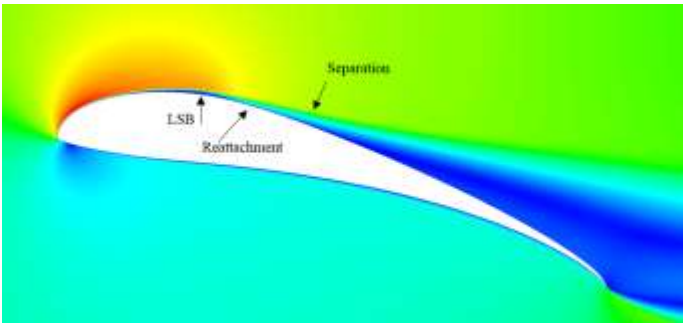

Figure 4.26 – Velocity contours for the S1223 at $\alpha = 16°$ and $Re = 2 \cdot 10^5$.

4.3 Validation of Wind Tunnel Boundary Corrections

This section presents a CFD analysis of the wing models placed inside the wind tunnel and, through the use of the correlations presented in sections 2.4.1 and 2.4.2, compare their results with the freestream ones. It is important to note that this analysis only includes the top and bottom wall of the tunnel. It does not include the effect of the side walls since all cases are two-dimensional ones.

First, the Eppler 387 airfoil will be analyzed, and then, the S1223. All cases were run for Reynolds numbers of $2 \cdot 10^5$ and $3 \cdot 10^5$. Boundary conditions have been previously specified in section 3.4. Turbulence model set for the simulations was the γ-Re_θ.

4.3.1 E387

The comparison of wind tunnel (corrected and uncorrected) and freestream lift coefficient values can be viewed in Figure 4.27. Experimental data from the Langley LTPT (1988) was also added to the graphs for comparison purposes. For angles of attack from 0° to 7°, the corrections seem to match the wind tunnel values to both freestream and LTPT. For angles higher than 8°, little differences can be observed, but they remain much smaller than the uncorrected values.

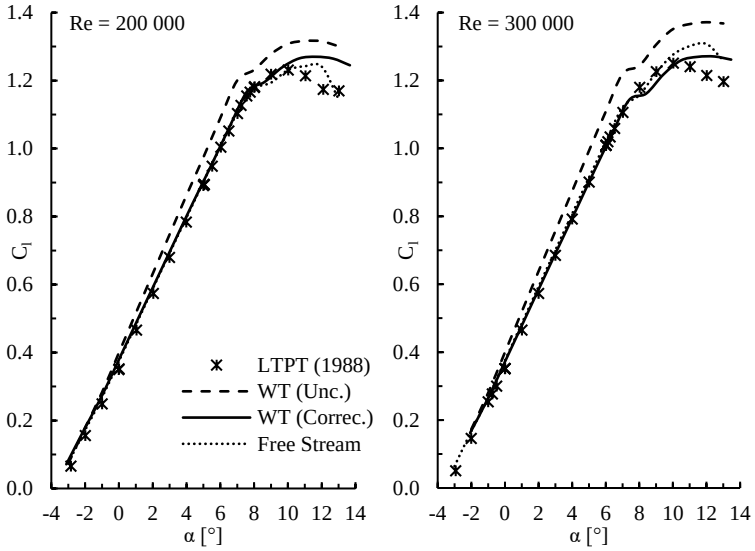

Figure 4.27 – Comparison of wind tunnel and freestream lift data for the E387.

Figure 4.28 shows the application of wind tunnel boundary corrections to the drag coefficient. The corrections moved the uncorrected values closer to the reference, which can be confirmed by performing a quantitative analysis below.

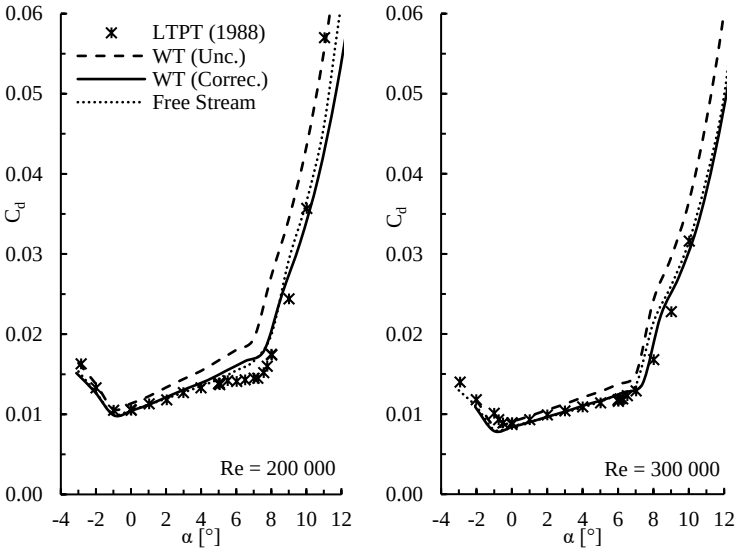

Figure 4.28 – Comparison of wind tunnel and freestream drag data for the E387.

Figure 4.29 and Figure 4.30 show the differences for both corrected and uncorrected wind tunnel results relative to freestream results.

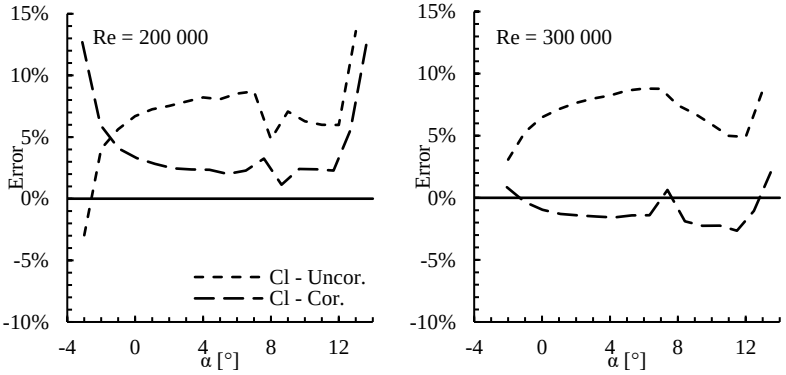

Figure 4.29 – Differences in wind tunnel C_l values relative to freestream values.

The boundary corrections used in the CFD wind tunnel cases seemed to be effective. Figure 4.29 indicates a significant decrease in lift error after the use of boundary correction. For the Re = 200 000 case, the average uncorrected C_l difference of 7% dropped to 2%. The same trend was identified in the $Re = 3 \cdot 10^5$ case.

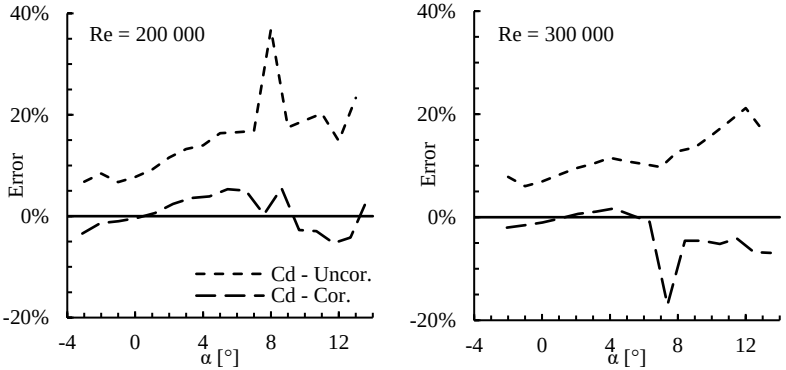

Figure 4.30 – Differences in wind tunnel C_d values relative to freestream values.

The boundary corrections were effective for drag values. The average difference went from 15% to 1% for $Re = 2 \cdot 10^5$ and from 12% to 3% for $Re = 3 \cdot 10^5$.

It can be concluded from the previous results that the boundary corrections were effective for the E387 airfoil. The average lift coefficient difference from freestream results was less than 2% and less than 3% for drag.

4.3.2 S1223

The same analysis of the previous sections was performed in the S1223. Wind tunnel and freestream lift coefficient are given in Figure 4.31. Experimental data from the UIUC (1995) was also plotted in the graphs. For all angles of attack tested, the boundary corrections seemed to be very effective. Practically no discernible differences were identified between the freestream and corrected wind tunnel curves. Only at Re = $3 \cdot 10^5$ and angles from 12° to 16°, minor errors could be observed.

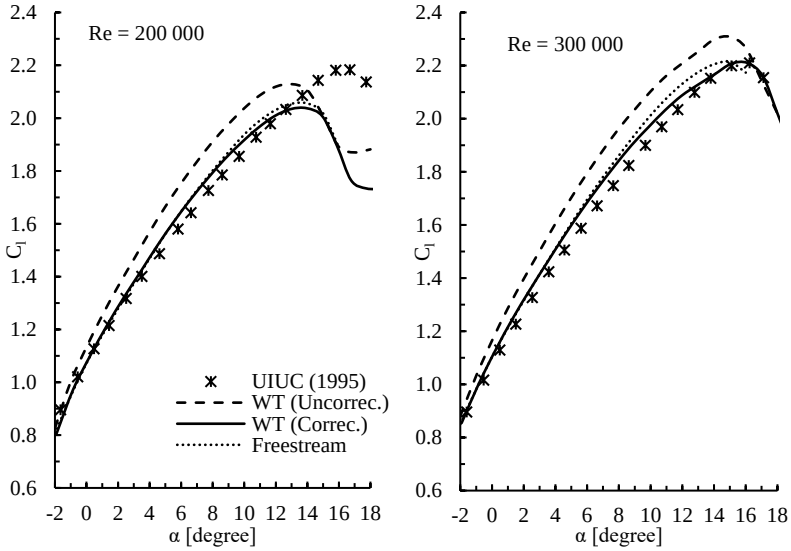

Figure 4.31 – Comparison of wind tunnel and freestream lift data for the S1223.

The same pattern is observed for the drag values, in Figure 4.32. Both freestream and corrected wind tunnel drag curves nearly overlap each other, becoming difficult to identified the errors. Thus, Figure 4.33 and Figure 4.34 show only the wind tunnel error relative to freestream data.

Regarding lift coefficient, Figure 4.33 shows that the maximum error was less than 5 % for the corrected values. The average error dropped from 5 % for the uncorrected curve to less than 1 % for the corrected one in both Reynolds numbers. For the drag values, the average error went from 26 % to 4% for Re = $2 \cdot 10^5$ and from 16 % to 3 %.

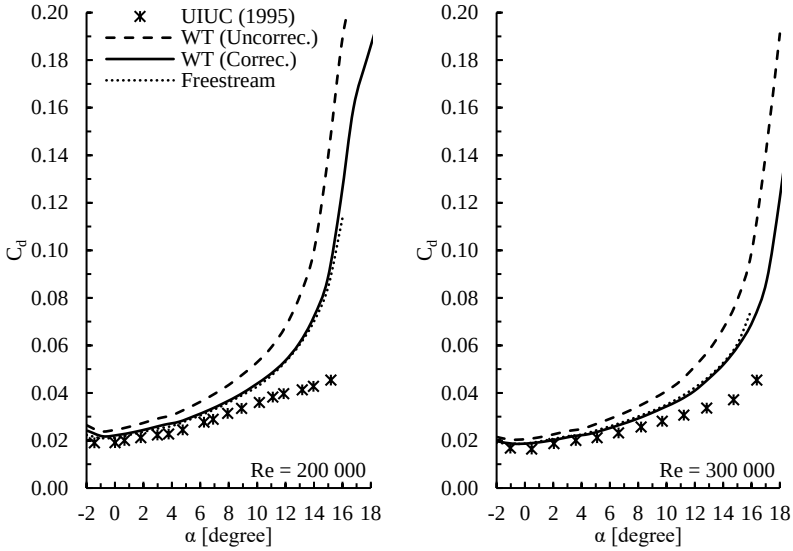

Figure 4.32 – Comparison of wind tunnel and freestream drag data for the S1223.

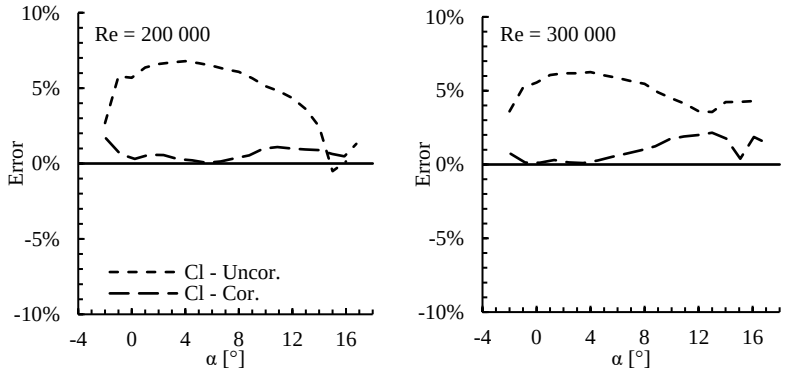

Figure 4.33 – Error in wind tunnel C_l values relative to freestream values.

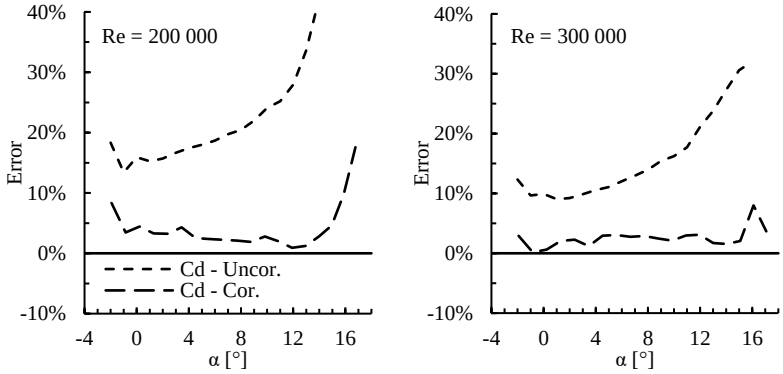

Figure 4.34 – Error in wind tunnel C_d values relative to freestream values.

5 EXPERIMENTAL ANALYSIS

All experiments were performed in the small-scale wind tunnel at the Federal University of Santa Catarina (UFSC). The wind tunnel used was manufactured by Plint & Partners Ltd. and its specifications are listed in section 5.2. This chapter also presents detailed description of the wing model used, lift, drag and pressure measurement techniques, and data acquisition equipment. Data reduction procedures have already been presented in section 2.4.

5.1 Wing Construction

The wind tunnel model must match as close as possible the geometry used for the CFD simulations. The material chosen for this purpose was Medium-Density Fiberboard (MDF) which consists in combining wood fibers with wax and a resin binder to form panels. In addition, it was necessary to select an adequate manufacturing process, which led to Computer Numerical Controlled (CNC) Laser cutting machine as a suitable choice.

Generally, MDF is commonly available in sheets and the Laser cutting machine has a maximum cutting thickness limit for each type of material, hence the best way found to build the wing was cutting many MDF wing sections and assemble them together to create the wing as seen in Figure 5.1.

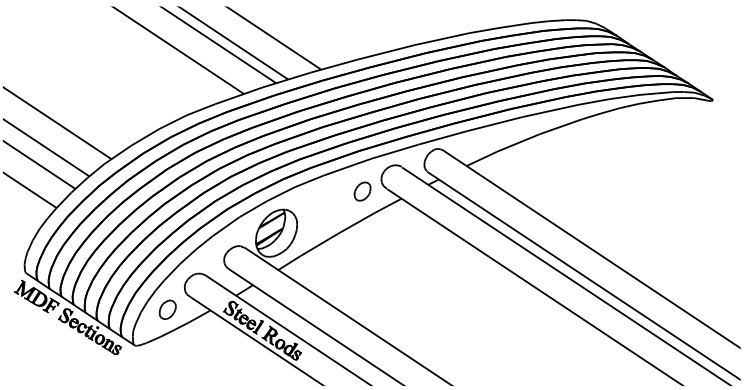

Figure 5.1 – Sketch of MDF wing sections assembled together.

6 mm MDF sheets were selected to compose the model and were joined by 8 mm diameter steel rods. Since the wind tunnel width was

about 450 mm, 75 wing sections were cut. These sections were aligned with the steel rods and glued together with cyanoacrylate. Moreover, an aluminum tube was placed inside the wing to allow its attachment to the scale of the wind tunnel.

The Laser cutting process created minor irregularities on the surface requiring them to be treated. First, a coat of epoxy resin was applied to fill any empty spaces that may have occurred between sections and to smooth the entire wing surface. Second, polyester filler was added to fill low spots on the surface and then sanded flush. To the finishing process, 3 coats of black paint and 2 coats of epoxy resin were applied. After that, the surface was sanded from 120 grit until 1200 grit sand papers. That ensured a surface with very low roughness.

The wing also features a few hollow sections (Figure 5.2) at approximately its mid span, which were added to make room for the pressure measurement hoses. At this location, as shown in Figure 5.3, 21 pressure tapping holes of 0.5 mm in diameter were spread on the surface and conducted through small hoses in the interior of the wing to an external pressure transducer. Figure 5.4 displays a top view schematic of the wing mounted to the wind tunnel.

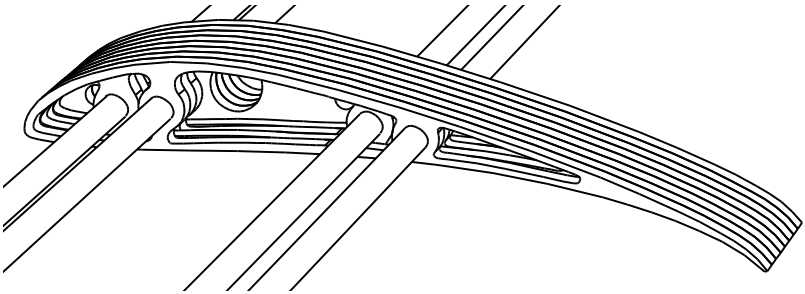

Figure 5.2 – Detail of the hollow wing sections at mid span.

Figure 5.3 – Detail of hoses connected to pressure tapping holes at mid span.

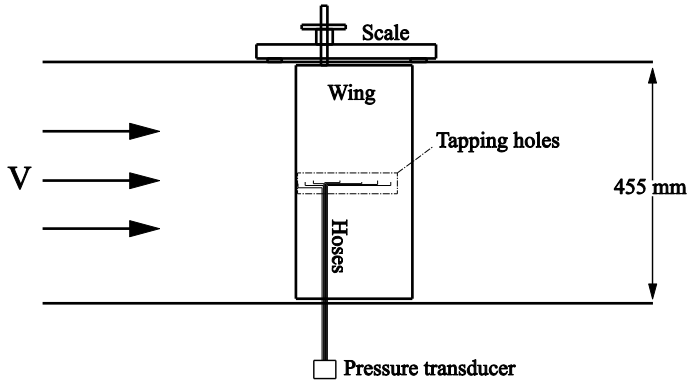

Figure 5.4 – Top view schematic of the wing mounted inside the tunnel.

5.2 Wind Tunnel

The wind tunnel used is an open circuit wind tunnel, i.e., it does not directly re-circulate air. The test section is rectangular with dimensions of 455 mm x 455 mm and length of 1,2 m. Throughout the test section, the area increases gradually in order to compensate the growth of the boundary layer at the walls.

The airflow velocity induced by the radial fan varies from 0 m/s to approximately 25 m/s. A variable frequency drive (VFD) controls the speed of the 18,5 kW motor of the fan that is located between the air inlet and the test section. The air inlet, placed on the side of the tunnel, is kept fully open during tests. Between the fan and the test section, there are five screens to make the velocity profile more uniform and reduce the turbulence intensity in the whole flow field. Figure 5.5 shows the wind tunnel scheme.

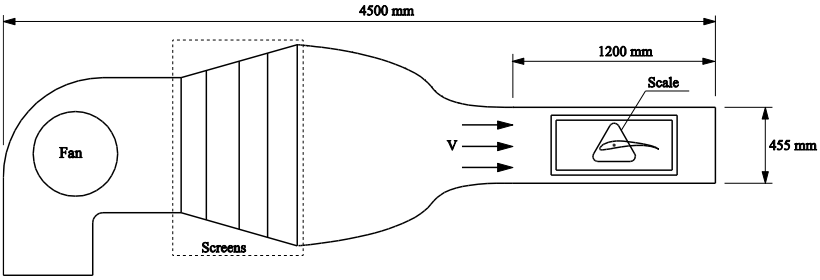

Figure 5.5 – Rendering of the axial cross-section of the wind tunnel.

The tunnel has a scale, placed externally to the test section, to measure aerodynamic forces and moments. It contains a fixed and a movable part. The original scale was modified to operate with strain gauges. There are two strain gauges for vertical forces and one for horizontal forces. These gauges are attached to a thin metallic cantilever plate acting as “springs”, which are located on the fixed part of the scale. The movable part, where the model is attached, links to the fixed part through three thin metal strips. Each strip is connected to the springs transferring the load to the scale by means of traction. The voltage variation registered by the strain gauges measures the deformation of the cantilever plates and varies linearly with the load. The measuring range is 0 to 5 V. The scale also incorporates a spirit level to prevent unwanted moments and vertical and horizontal components. The attachment between the model and the scale is realized through a 12,7 mm diameter and 2 mm thick aluminum tube. The tube is fixed on a tapered bushing. Details of the scale can be seen in Figure 5.6.

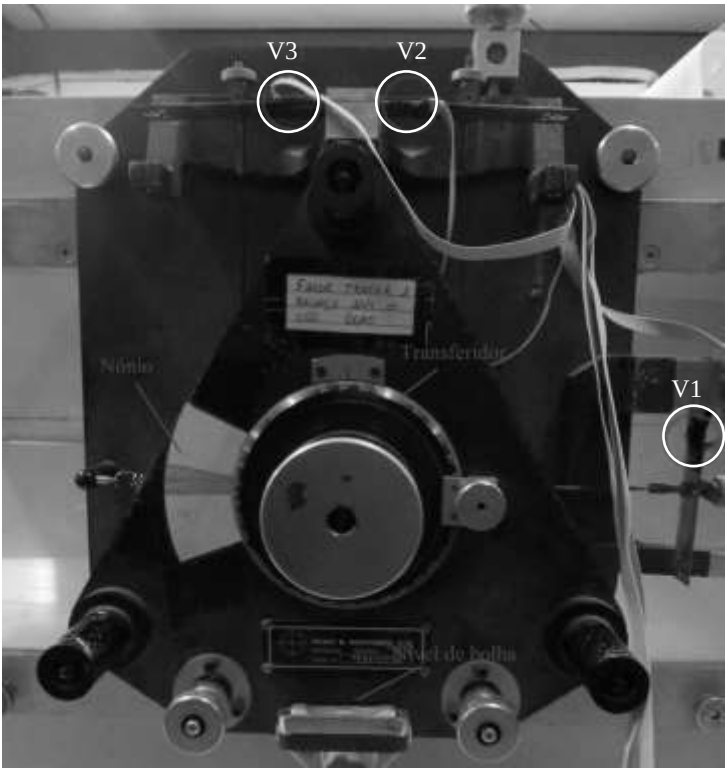

Figure 5.6 – Wind tunnel scale for measurement of forces and moments. V1 is the strain gauge for horizontal forces and V2 and V3 are for vertical forces.

The equipment used in the wind tunnel facility can be seen in Table 5.1.

Table 5.1 – Equipment used.

Equipment	Manufacturer	Model	Serial Number
Wind tunnel	Plint & Partners Ltd.	TE44	2035
Fan	Airscrew-Weyrok Ltd.	2417V8	56944
Motor	Crompton Parkinson Ltd.	0160D	B719R
Variable Frequency Drive	WEG	IGBT Inverter CFW-05	-
Scale	Plint & Partners Ltd.	TE81	2036

5.3 Scale Calibration and Force Measurement

In order to calibrate the wind tunnel scale, known standard masses were applied to the strain gauges V2 and V3 separately: 0 g, 500 g, 1000 g, 1500 g and 2000 g. The masses were on a support above the connection point between the metal strip and the spring. Figure 5.7 shows the load being applied to the scale.

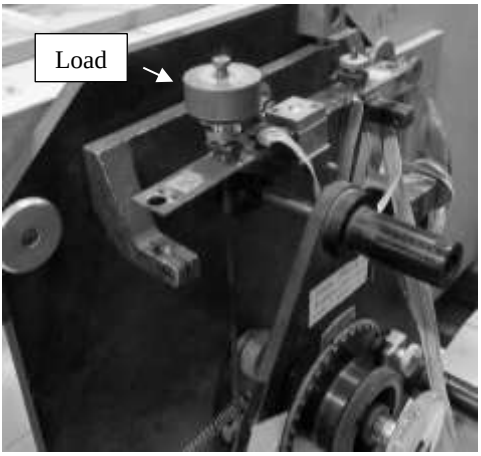

Figure 5.7 – Load being applied on the spring to calibrated strain gauges V2 and V3.

Since V1 is placed perpendicular to V2 and V3, it is impossible for the standard mass to sit on the gauge. Therefore, the drag force is simulated with a pulley system that connects the mass to the gauge, as seen in Figure 5.8. Plus, since aerodynamic drag forces are generally much smaller than lift forces, the masses used for calibration of V1 are not required to be as large as the ones used for V2 and V3. Thus, masses varying from 0 to 500 g were applied on V1.

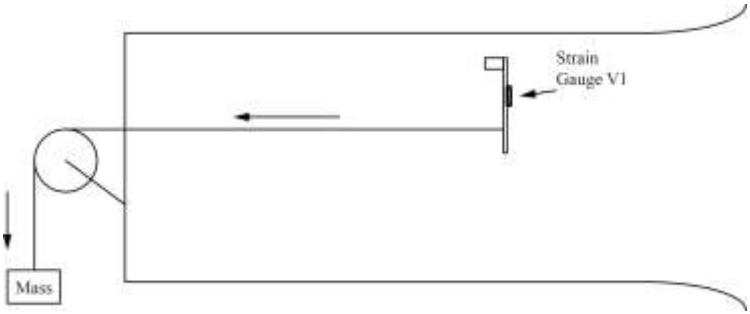

Figure 5.8 – Calibration of V1.

Data acquisition for each load lasted 30 seconds to obtain a reasonable data sample and to avoid oscillations. Then, using the least squares method, a curve is fitted to correlate the applied load with the voltage read on each strain gauge. Figure 5.9 shows an example of the curve fitting

process. As observed, each gauge has a different sensibility for the same load. That explains the importance of obtaining a single curve for each strain gauge. Prior to every wind tunnel test, a new calibration process was performed to obtain new calibration curves.

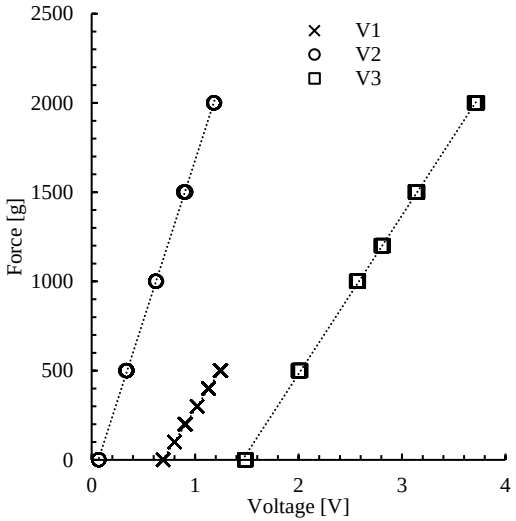

Figure 5.9 – Example of calibration curve.

5.4 Measurement of Aerodynamic Forces

Measurement of lift force was done using the V2 and V3 strain gauges. After calibrating the wind tunnel scale, a single coefficient was obtained for each gauge, which related the voltage measured into force. Prior to each test, the value indicated by each strain gauge was measured. These values were used to reset the scale. They were subtracted from the values measured and the difference was equivalent to the load applied on the model. The resulting lift force is given by

$$L = F_2 + F_3 = \Delta V2 \cdot K_2 + \Delta V3 \cdot K_3 \tag{5.1}$$

where L is the lift force; F_2 and F_3 are the forces measured through the strains gauges V2 and V3; $\Delta V2$ and $\Delta V3$ are the voltage variations of the gauges V2 and V3; and K_2 and K_3 are the coefficients obtained from the calibration process (WERNECK, 2014).

Drag force was measured using the same process of the lift force, differing by the use of only V1 instead of V2 and V3 strain gauges. The resulting drag force is given by

$$D = F_1 = \Delta V1 \cdot K_1 \tag{5.2}$$

where D is the drag force; F_1 is the force measured through the strain gauge V1; $\Delta V1$ is the voltage variation of the gauge V1; and K_1 is the coefficient obtained from the calibration process.

5.5 Pressure Measurement

Pressure measurements were carried out by using a computer-controlled data acquisition system. The pressure was measured by using Honeywell HSCDRRN002NDAA5 differential pressure transducer with a pressure range of ± 500 Pa and a total error band of ± 1.5% FSS (Full Scale Span). The maximum response time of the pressure transducer was about 1 ms and has been previously calibrated by the manufacturer.

The pressure transducer was linked to an Agilent 34401A Digital Multimeter, which was then linked to the PC through the RS-232 interface. Figure 5.10 shows the equipment used for pressure measurement while Figure 5.11 illustrates the circuit schematic diagram for the pressure transducer.

Figure 5.10 – a) Honeywell pressure transducer; b) Agilent 34401A DMM.

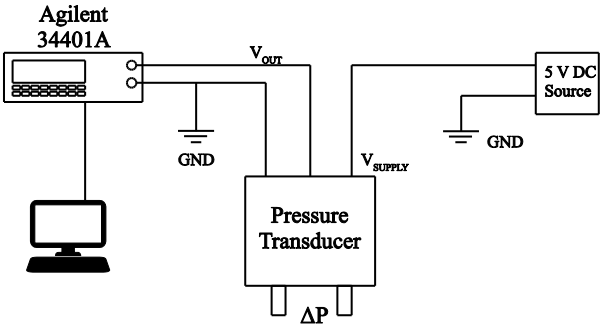

Figure 5.11 – Circuit schematic diagram for the pressure transducer.

Pressure readings were acquired at a rate of 55 Hz, due to interface limitations, and with a resolution of 4½ digits. A MATLAB code was developed in order to operate remotely the 34401A via PC and save the pressure readings to text files. Average and standard deviation values were extracted from pressure data as seen in Figure 5.12.

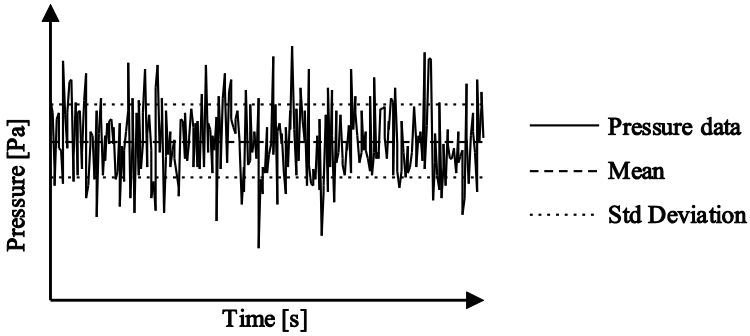

Figure 5.12 – Example of pressure data acquired by the pressure measurement system.

5.6 Wind Tunnel Flow Calibration

When there is no model in a test section, a measuring device, most commonly a pitot-static tube, can be put there to determine the air speed. One cannot, however, insert a pitot-static tube or other measuring device in the test section to measure dynamic pressure or speed along with an object under test because the test object will cause changes (induced flow) in the flow (BARLOW *et al.*, 1999).

The reduction of section area in the tunnel works as a Venturi, creating a pressure difference p_1-p_2 in the presence of air flow. This pressure difference can be correlated with the air speed in the test section as shown by the equations below.

$$Q = v_1 A_1 = v_2 A_2 \tag{5.3}$$

$$Q = A_1 \sqrt{\frac{2}{\rho} \cdot \frac{p_1 - p_2}{\left(\frac{A_1}{A_2}\right)^2 - 1}} = A_2 \sqrt{\frac{2}{\rho} \cdot \frac{p_1 - p_2}{1 - \left(\frac{A_1}{A_2}\right)^2}} \tag{5.4}$$

Figure 5.13 shows the schematic for flow calibration. The pressure outlets p_1 and p_2 were connected to the pressure transducer of section 5.5 and the velocity was measured with a hot-wire anemometer. A Testo 435-2 Multifunction meter attached to the Testo 0635 1535 flow velocity probe was used (Figure 5.14). The velocity probe offers a measuring range of 0 to 20 m/s and has an accuracy of ±(0.03 m/s + 4% of measured value). The multifunction meter was connected to the PC via USB to transfer the velocity readings.

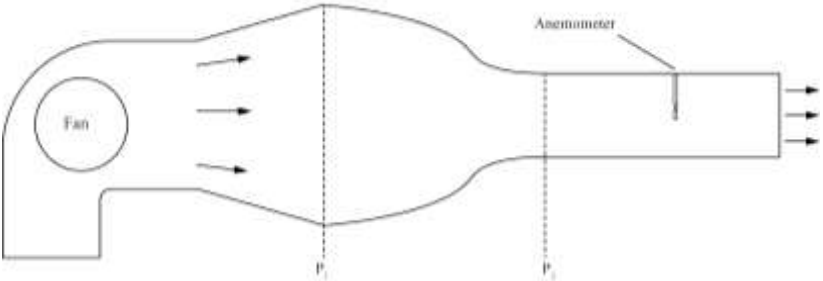

Figure 5.13 – Schematic for wind tunnel flow calibration.

a) b)

Figure 5.14 – a) Testo 435-2 Multifunction meter;
b) Testo 0635 1535 probe (right).

The measurement procedure was accomplished by varying the frequency on the VFD and saving the pressure and velocity values at each frequency. The Measurements were taken for 30 seconds at each frequency set on the drive. Results are displayed in Figure 5.15.

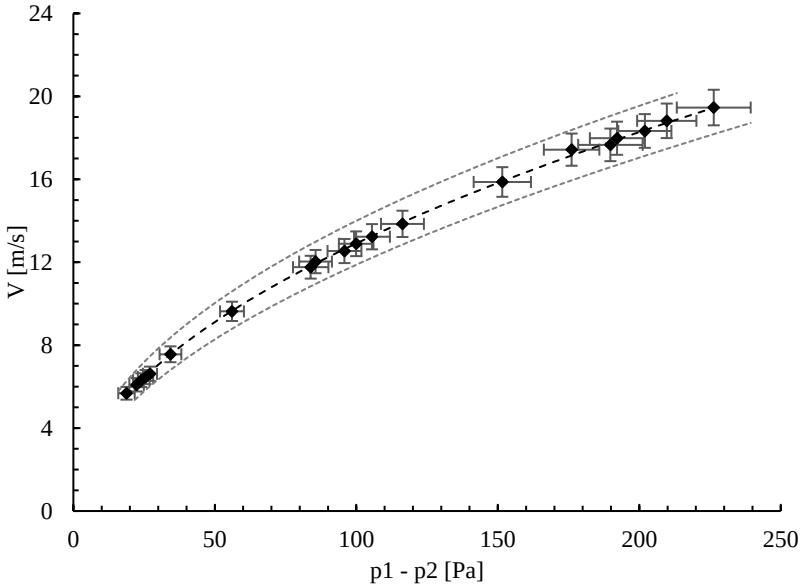

Figure 5.15 – Velocity measurements for different frequencies set on the VFD.

Then data was fit a power regression method which resulted in a R^2 value of 0.9997. The curve equation is displayed below

$$V = 1{,}2803 \cdot (p_1 - p_2)^{0{,}5018} \tag{5.5}$$

A power close to 0,5 was expected since Eq. (5.4) states that $V \sim \sqrt{p_1 - p_2}$.

For proper force and moment measurements, it is important for the freestream velocity to be as uniform as possible in the test section. In ideal conditions, the freestream velocity is the same everywhere in the test section. In reality, there are small variations in the velocity caused by the presence of the tunnel walls and various effects such as flow turning the tight corner at the inlet of the tunnel (SELIG; MCGRANAHAM, 2004).

The variation of velocity in the test section was obtained by measuring the velocity with a pitot-static probe. The measuring plane extended from -20 cm to +20 cm using a grid spacing of 2 cm in the vertical direction y, and -20 cm to 20 cm using a grid spacing of 5 cm in the horizontal direction x. Figure 5.16 shows the velocity profile for $V = 10$ m/s. Each point represents the average velocity of different horizontal locations within the test section. The errors were obtained by evaluating the maximum and minimum velocity values in each horizontal location. It is clear that the profile has good uniformity along the y-direction.

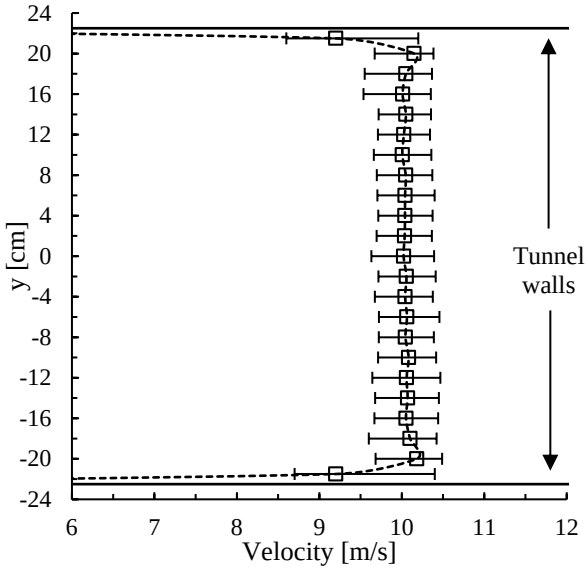

Figure 5.16 – Average velocity profile in the test section.

5.7 Measurement of Angle of Attack

Angles of attack were measured with a digital angle meter or inclinometer model XB-90 (Figure 5.17). The device has an accuracy of ±0,1° and resolution of 0,1°. It is equipped with a magnetic base for use on metal surfaces.

In order to properly align the wing with the tunnel, first the inclinometer is placed on the tunnel wall to reset the device. After that, it is placed on a L-shaped metal bar which is fixed exactly on the chord line, as shows Figure 5.18. Then, the wing is rotated until the inclinometer displays 0,0°, meaning that the wing is parallel to the wind tunnel. Finally, the inclinometer and the metal bar can be removed from the wing, to allow the closure of the test section window, and attached to the scale outside the tunnel (Figure 5.19). Thus, angles of attack can be set directly on the scale and visualized on the inclinometer.

Figure 5.17 – Digital inclinometer XB-90 used in this work.

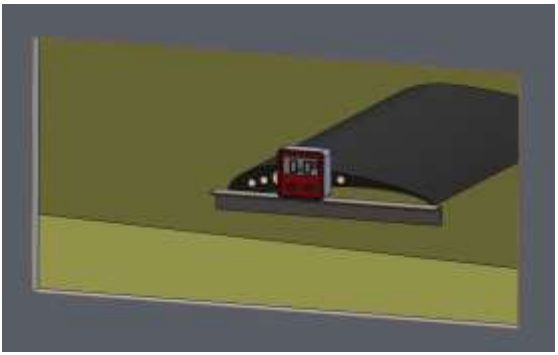

Figure 5.18 – Inclinometer on the wing

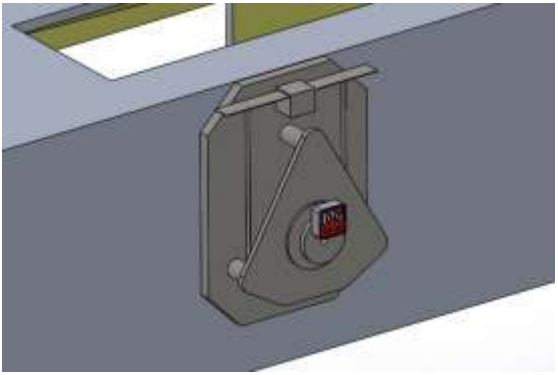

Figure 5.19 – Inclinometer on the scale.

5.8 Measurement Procedure

Once the tunnel scale and the inclinometer have been calibrated and reset, the measurement of lift and drag data can be initiated. With the model installed in the tunnel and fan turned on, an angle of attack is set and its value checked on the inclinometer. Then, the forces measured on the scale are recorded for 1 minute. During this time, tunnel air speed is recorded by measuring the pressure difference $p_1 - p_2$ shown in section 5.6. This process is necessary due to the head loss that the model can cause in the tunnel flow. Also, ambient air temperature and humidity are recorded to calculate the air density. After completion of these procedures, another angle of attack is set to the model and whole process starts again.

For the pressure measurements, the procedure is similar. Wind tunnel speed and air density are also recorded for every angle of attack. The difference is in setting the angle. Since α must be corrected by boundary correlations, it must be set a value on the inclinometer which, after the use of the correlations, will result in the desired angle of attack. For instance, if an angle of attack of 8° is desired at $Re = 2 \cdot 10^5$, the angle on the tunnel should be set on 7,2°, because after the use of the correlations, the 7,2° in the wind tunnel would become 8° in freestream.

The uncertainties of the measurements are explained in Appendix A.

6 WIND TUNNEL RESULTS

This section presents the results acquired in the wind tunnel. First, data from the tunnel is corrected and compared to the CFD results. Then, a leading-edge device is installed on the model and its results are also compared to the previous ones.

6.1 Lift and Drag Data

Figure 6.1, Figure 6.2 and Figure 6.3 show the effect of wind tunnel boundary corrections for Reynolds numbers of $1 \cdot 10^5$, $2 \cdot 10^5$ and $3 \cdot 10^5$, respectively. The UIUC data was used here as a benchmark.

All Reynolds number cases reported lower values for C_l and C_d after corrections were applied. For $Re = 1 \cdot 10^5$, the C_l value at stall point was close to the reference but drag values were way higher than expected, which suggests the prevalence of model flaws. Even with the boundary corrections, the difference between the actual model and the benchmark was as high as 60%.

For $Re = 2 \cdot 10^5$ and $3 \cdot 10^5$, the same pattern was observed. The stall angle was around 4° higher but maximum C_l showed a good agreement. Although lift curves did not match the reference, their shape in the stall region were very similar. This indicates that stall mechanism may have been the same in both sources.

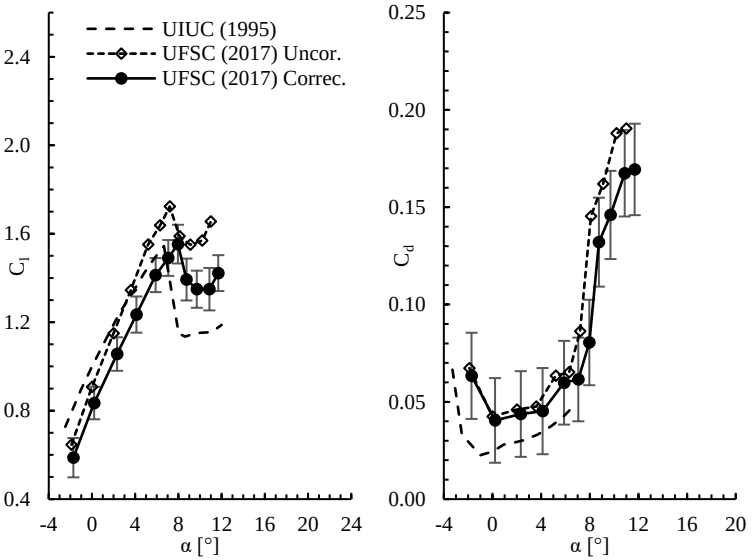

Figure 6.1 – Corrected and uncorrected lift and drag coefficients of the S1223. ($Re = 1 \cdot 10^5$)

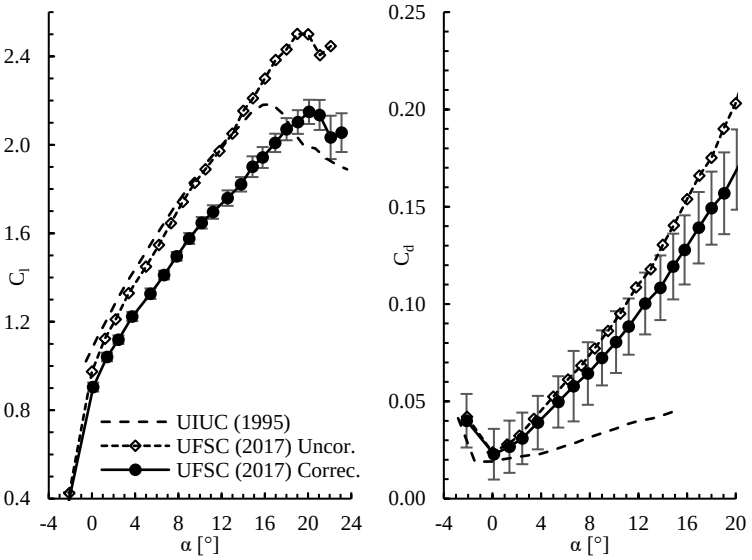

Figure 6.2 – Corrected and uncorrected lift and drag coefficients of the S1223. ($Re = 2 \cdot 10^5$)

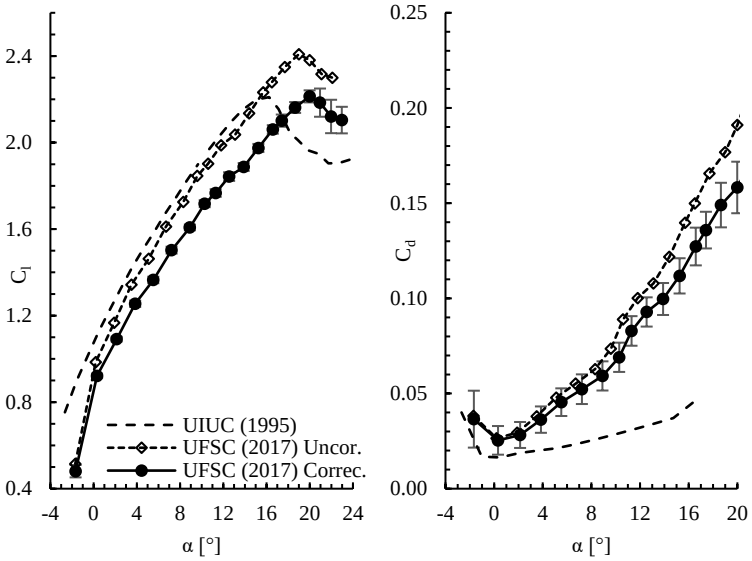

Figure 6.3 – Corrected and uncorrected lift and drag coefficients of the S1223. ($Re = 3 \cdot 10^5$)

There can be many reasons for the observed discrepancies, not least of which is the fact that drag data from UIUC was taken by wake measurements while UFSC data used a scale. Still, the drag difference was too large to be attributed only to the measurement method, which leads to model flaws as the major source of errors.

The comparison between wind tunnel and CFD result is given in Figure 6.4. In the experiments, the stall angle was 8°, 20° and 20° for Re = $1 \cdot 10^5$, Re = $2 \cdot 10^5$ and Re = $3 \cdot 10^5$, respectively. In the numerical results, the prediction of lift gave different results. Although the γ-Re_θ C_l values were closer to the experiments, the k-k_L-ω reported better agreement regarding stall. Drag values again showed large differences. Only at Re = $1 \cdot 10^5$ drag curves showed a better agreement. For the other Reynolds numbers, only at $\alpha = 0°$ the difference in drag values was acceptable. All other angles the error was relatively high.

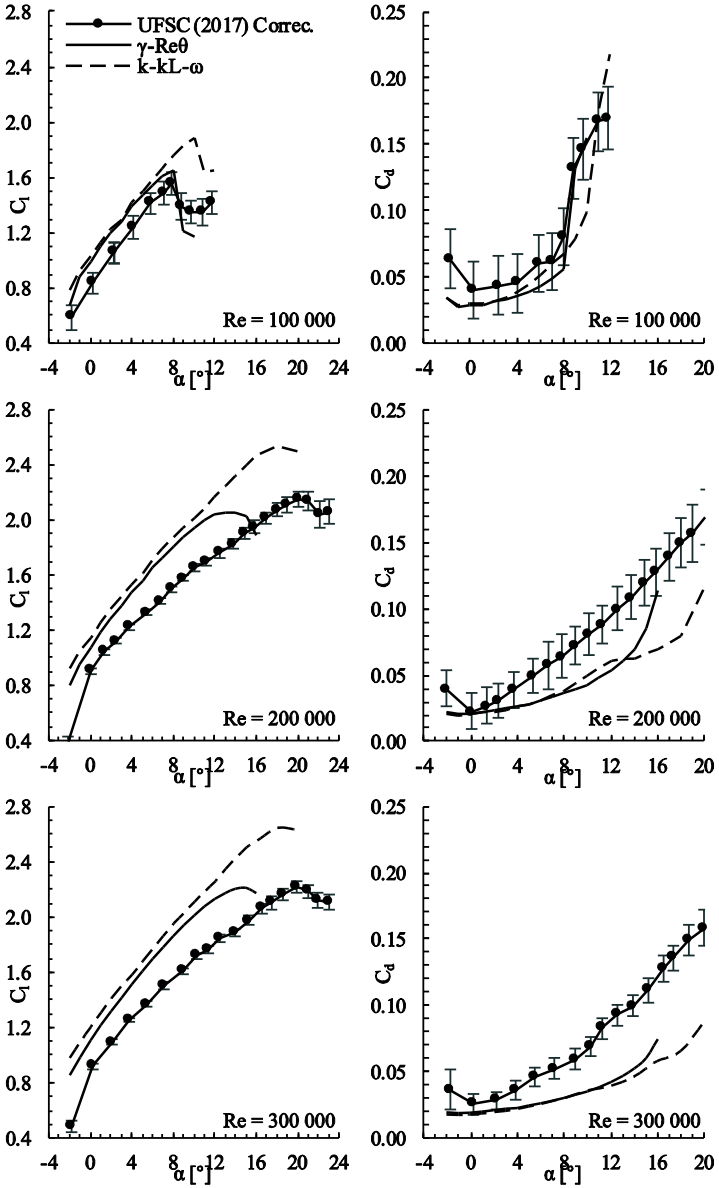

Figure 6.4 – Corrected lift and drag tunnel data in comparison with numerical values.

6.2 Pressure Coefficient Measurements

The pressure distributions measured in the wind tunnel were also taken for $Re = 1 \cdot 10^5$ (Figure 6.5), $Re = 2 \cdot 10^5$ (Figure 6.6) and $Re = 3 \cdot 10^5$ (Figure 6.7). Since no other experimental C_p data for this airfoil were found, results were plotted together with CFD data.

At $Re = 1 \cdot 10^5$, good agreement was achieved for angles from 0° to 6°. Pointed by the arrows, the laminar separation bubble can be distinguished in almost all angles of attack and seems to match better the k-k_L-ω curve. At $\alpha = 0°$, however, the hump in C_p is not clear. In this case, the LSB may be long enough to not cause any visible pattern on the measurement range. At $\alpha = 10°$ the airfoil is stalled.

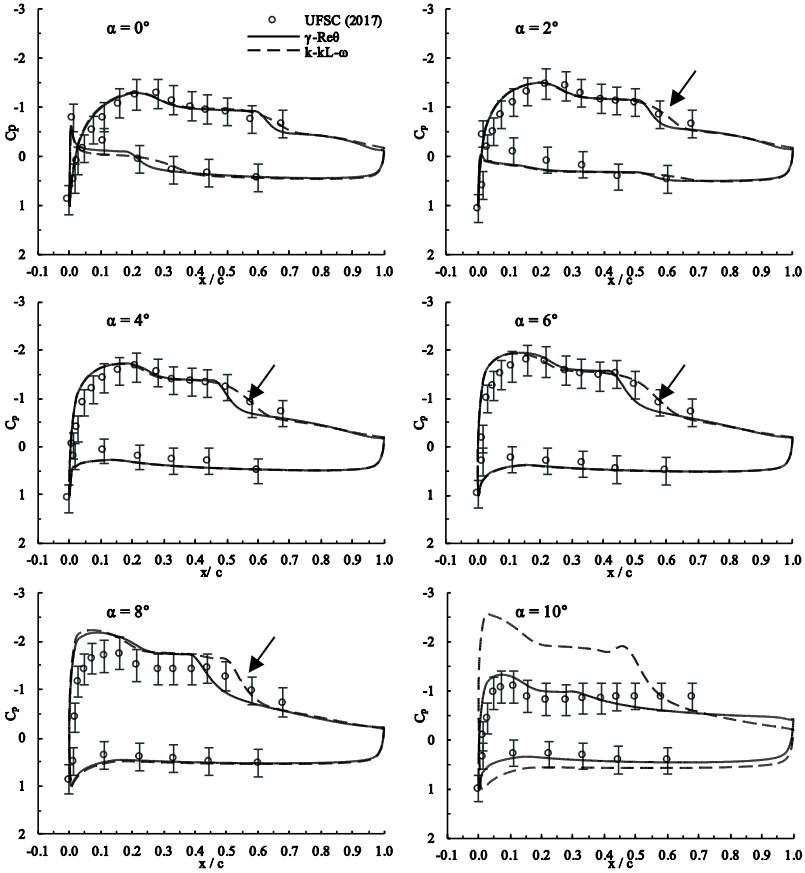

Figure 6.5 – Numerical and experimental C_p for the S1123. ($Re = 1 \cdot 10^5$).

For a Reynolds number of $2 \cdot 10^5$ (Figure 6.6), notable differences were seen in comparison with $Re = 1 \cdot 10^5$. No bubble was detected by the experiment at $\alpha = 0°$ and 2°. Even at $\alpha = 4°$ it is difficult to detect. The increase in tunnel speed to achieve the desired Reynolds number may have led to higher freestream turbulence intensity which suppresses the LSB. However, even with high turbulence one can see the LSB pattern at $\alpha = 6°$ and above. Taking $\alpha = 8°$ for example, the hump is so sharp that, unlike the $Re = 1 \cdot 10^5$ case, the experimental points seem to agree better with the γ-Re_θ model.

Beginning at $\alpha = 10°$, the numerical models predicted a low-pressure peak near the leading edge (black arrow). This peak was not revealed

in the tunnel measurement and may have been suppressed due to high freestream turbulence or, more likely, small differences in the geometry of the manufactured airfoil. The presence of this low-pressure peak has great influence in the development of the boundary layer downstream on the airfoil surface and may affect bubble formation and stall behavior.

Overall, the experiment gave higher values for pressure on the suction surface and lower values on the pressure surface. This explains the lower lift values reported before and also suggests that the wing has geometric errors from the original S1223.

Similar trends were encountered for the $Re = 3 \cdot 10^5$ case (Figure 6.7).

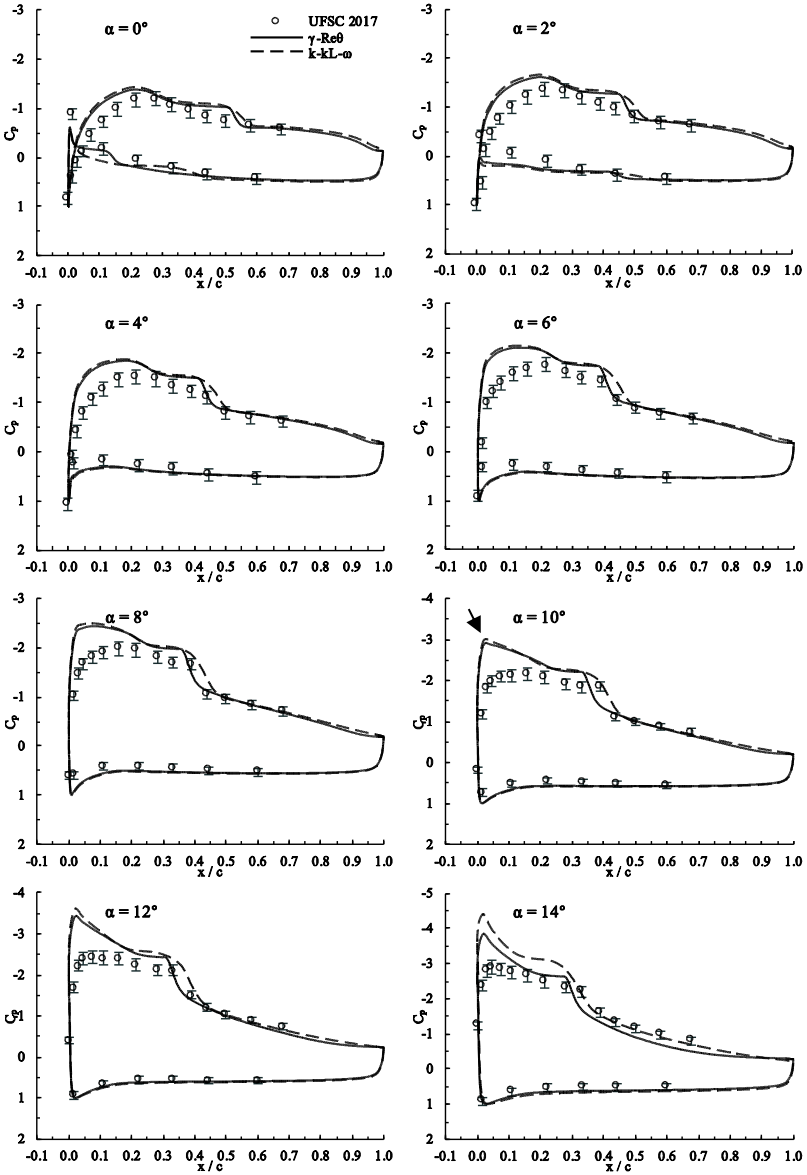

Figure 6.6 – Numerical and experimental Cp for the S1123. (Re = $2 \cdot 10^5$).

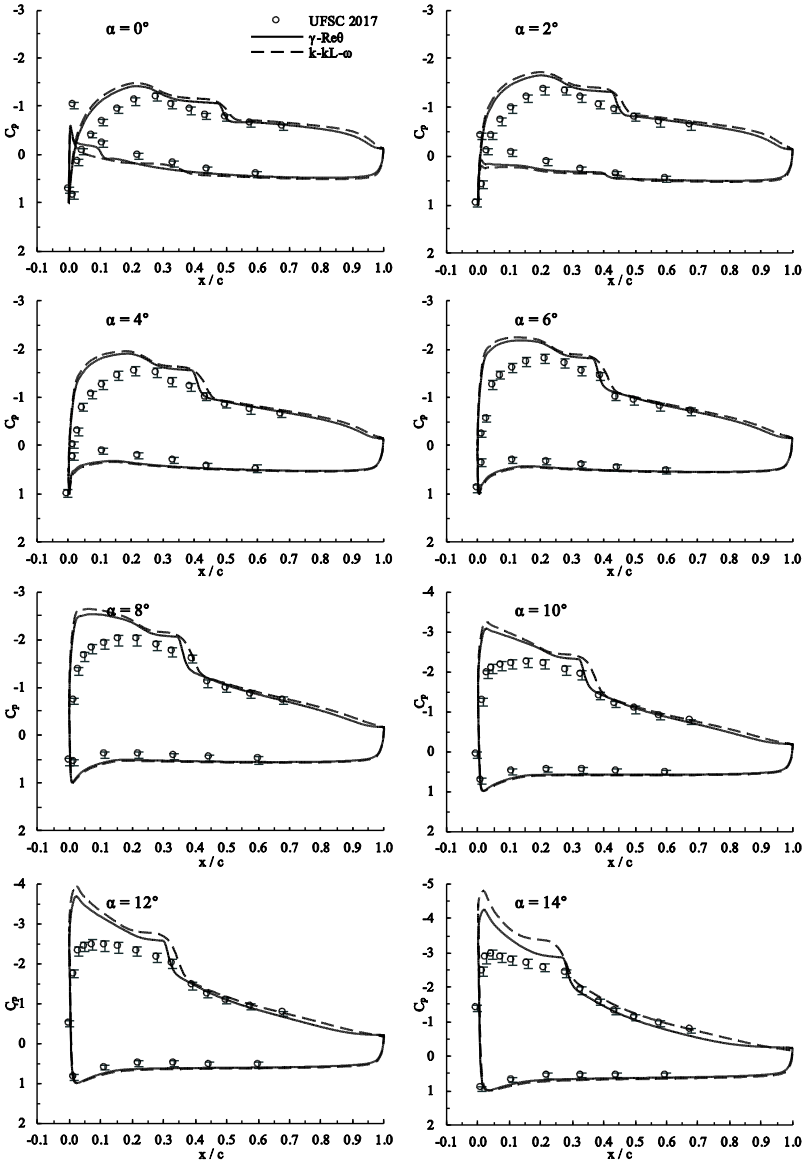

Figure 6.7 – Numerical and experimental C_p for the S1123. ($Re = 3 \cdot 10^5$).

6.3 Surface Oil Flow Measurements

In order to examine the existence of the laminar separation bubble, the surface oil flow technique was used. The mixture contained mineral oil, titanium dioxide and a small amount of oleic acid. The ratio of mineral oil and oleic acid was roughly 20:1 (GENÇ, *et al*., 2012).

Following Selig and McGranaham (2004), Figure 6.8 brings a photograph of the surface oil flow pattern and Figure 6.9 conceptually illustrates the connection between surface oil flow features and skin friction coefficient.

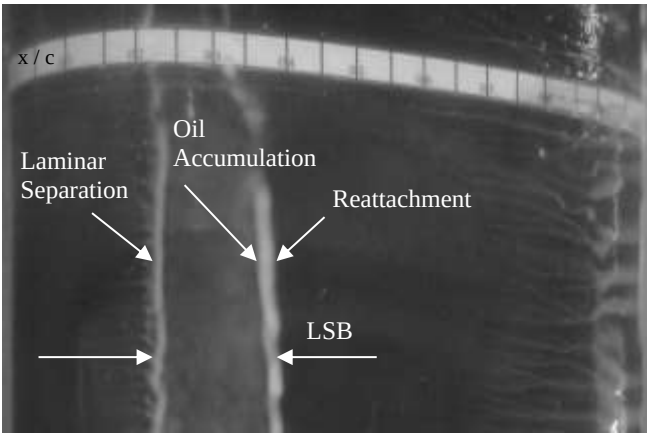

Figure 6.8 – Representative upper surface oil flow visualization on the S1223. ($\alpha = 10°$, $Re = 2 \cdot 10^5$)

Important flow features, such as laminar separation, oil accumulation and reattachment, could be identified and related to the skin friction coefficient. In Figure 6.8, laminar flow can be seen from the leading edge to approximately x/c = 20%. Downstream of the separation point, the oil remained stagnant because of the low friction forces. This stagnant flow was consistent with the behavior of the interior of a LSB.

As seen in Figure 6.8, the reattachment point varied along span but may be taken at x/c = 39%. Three-dimensional effects and model twist may have contributed to the distortion of the reattachment line. Downstream of reattachment, the boundary layer is turbulent. The high skin friction distribution tended to clear away oil more rapidly, making the black surface more visible. In order to illustrate how the oil moves on the surface over time, Figure 6.10 shows the transient state.

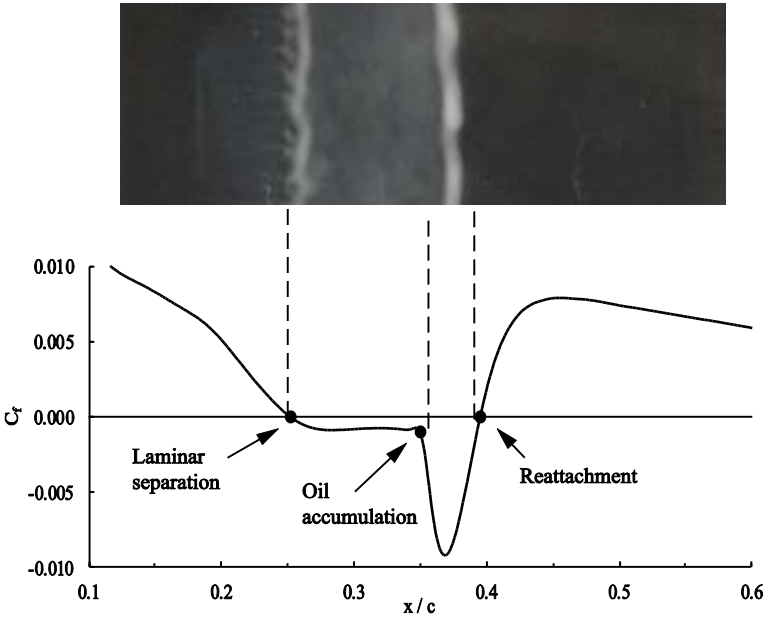

Figure 6.9 – Conceptual illustration of the relationship between the surface oil flow features and skin friction distribution in the region of a laminar separation bubble.

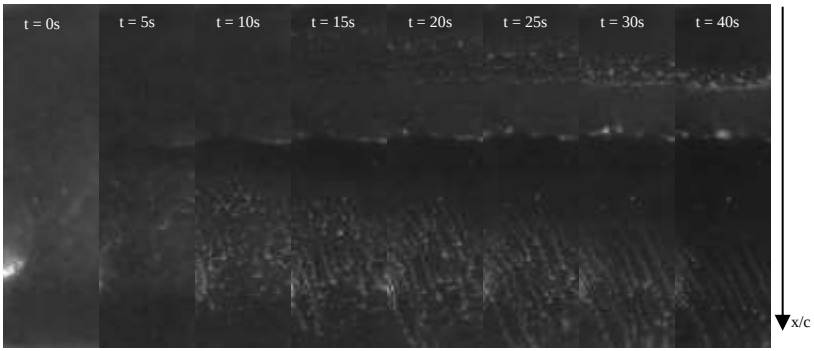

Figure 6.10 – Oil flow visualization for different time instants.
($\alpha = 16°$, $Re = 3 \cdot 10^5$)

The upper-surface oil flow features, as just described, were obtained over a range of angles of attack for Reynolds numbers of $1 \cdot 10^5$,

$2 \cdot 10^5$ and $3 \cdot 10^5$. These are shown in Figure 6.11 and compared with numerical simulation using transition-sensitive models. LS is the abbreviation for laminar separation and TR for turbulent reattachment. Since the separation and reattachment bars varied along span, error bars were added to the experimental points accounting for the minimum and maximum chord location of the line.

In Figure 6.11, as the Reynolds increased, bubble length became smaller since the separation and reattachment lines got closer to each other. This behavior agreed to the numerical predictions but there were some discrepancies.

At a Reynolds number of $1 \cdot 10^5$, laminar separation points were located upstream of the CFD values. Turbulent reattachment points revealed better agreement with the γ-Re_θ predictions. The absence of experimental point for higher angles at this Reynolds number were due to premature stall and the difficulty of identifying the pattern on the airfoil surface.

Moving to a Reynolds number of $2 \cdot 10^5$, the agreement in the laminar separation line between the data sets was mostly within 0 to 3% of x/c except on angles higher than 12°. Again, the reattachment line showed better agreement with the γ-Re_θ model. At these higher angles, the both numerical models tended to rapidly move the bubble towards leading edge, implying in lower values for separation and reattachment points. This pattern was not followed by the experimental case. At Re = $3 \cdot 10^5$, similar trends were observed, but it should be mentioned that bubble length became smaller. The effect of increasing the Reynolds number can be viewed in Figure 6.12.

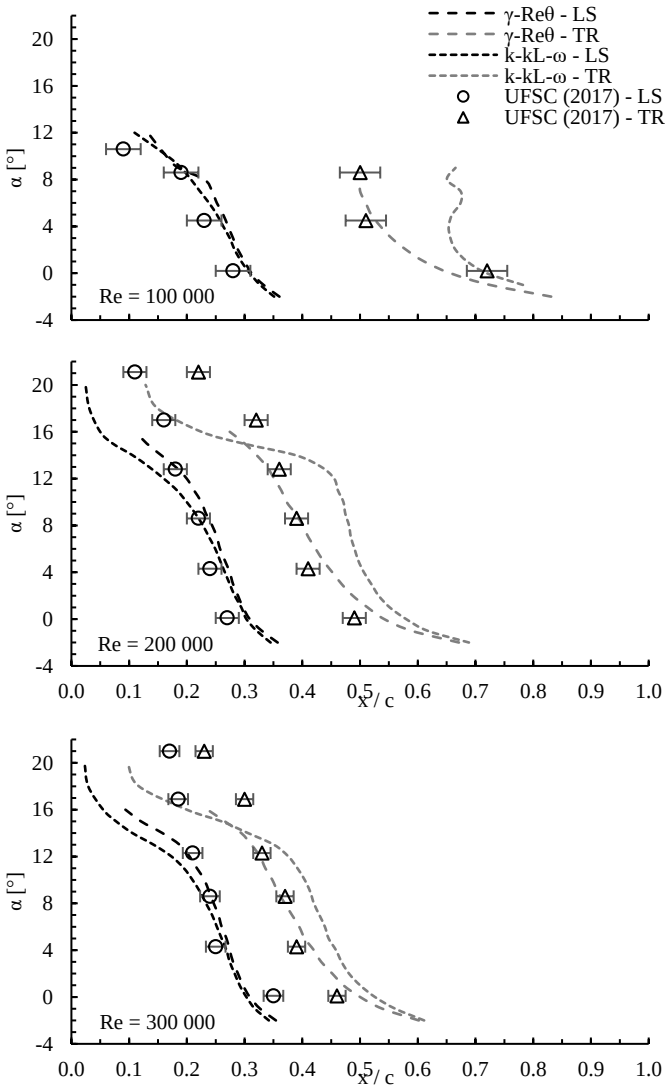

Figure 6.11 – Numerical and experimental comparison of major S1223 upper-surface flow features, i.e. laminar separation (LS) and turbulent reattachment (TR).

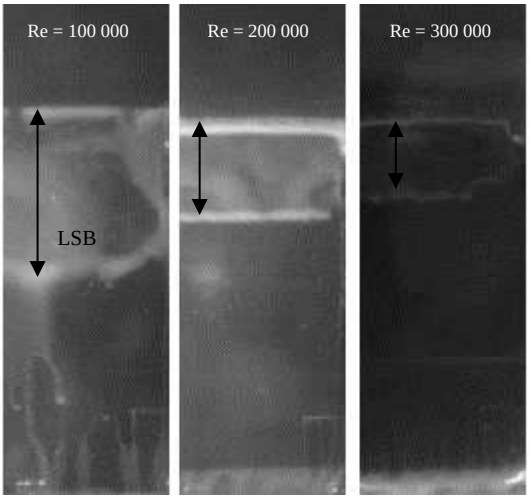

Figure 6.12 – Oil flow visualization for different Reynolds number. ($\alpha = 8°$)

To conclude, although the uncertainties were relatively high, both experimental and numerical analysis produced data that showed good agreement. Experimental points, in general, revealed a better match with the γ-Re_θ model, though the laminar separation predicted by the k-k_L-ω also matched tunnel data for a few angles of attack.

6.4 Leading-Edge Wire

This section provides an analysis of the use of turbulators in an airfoil. A leading-edge wire was chosen as the mechanism to be analyzed due to its simplicity and low cost. A 2 mm diameter full-span carbon fiber tube acting as the wire was mounted 20 mm ahead of the leading edge, as illustrated in Figure 6.13. Thin needles were used to connect the tube to the airfoil (Figure 6.14).

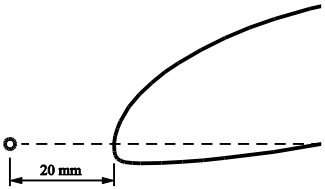

Figure 6.13 – Location of the leading-edge wire

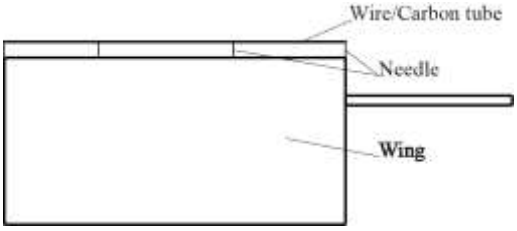

Figure 6.14 – Top view of the wired wing model.

Experimental and numerical lift and drag coefficients are given in Figure 6.15 for the S1223 with leading-edge wire at various Reynolds numbers.

At Re = $1 \cdot 10^5$, the stalling point obtained in the wind tunnel was much higher than the other lift curves. The γ-Re_θ model presented an angle of stall of 8°, followed by 11° for the k-k_L-ω and 21° for the wind tunnel model. It suggests that both transition-sensitive models were unable to predict the increase in C_l at angles higher than 11°. Since stall was delayed in the experimental model, the drag coefficient was lower than the CFD models for angles higher than 11°.

Moving to Re = $2 \cdot 10^5$ and $3 \cdot 10^5$, the leading-edge wire was ineffective to delay the stalling condition. A linear increase in lift at low angles of attack is expected in regular airfoils. However, a minor discrepancy in lift was observed (black arrows). All lift curves at these Re numbers predicted this behavior but at different angles of attack. It is believed that it has some relation to the turbulent air coming from the wire and flowing in a singular manner, for each method, over the airfoil surface. This effect was also reflected on the drag curves as a sudden increase of drag. Regarding drag values, there was good match between the wind tunnel and CFD data at angles lower than 4°.

To complement the discussion above, it is interesting to plot only the wind tunnel data for the plain and wire cases, as seen in Figure 6.16. Since the curves are close to each other, points and error bars have been hidden to aid visualization. As stated before, the increase in C_l and angle of stall at Re = $1 \cdot 10^5$ was very large due to leading-edge wire. Drag coefficient for this configuration was lower for angles higher than 8°. For the higher Reynolds number cases (Re = $2 \cdot 10^5$ and Re = $3 \cdot 10^5$), wired configurations reported lower lift and higher drag for almost all angles of attack. Nevertheless, it should be highlighted that stall on the plain S1223 was steeper than on the one equipped with the leading-edge device. Also, drag coefficient at very low angles of attack ($\alpha < 0°$) was larger on the

plain configuration. These observations may indicate that the leading-edge wire still produces some aerodynamic benefit for the airfoil.

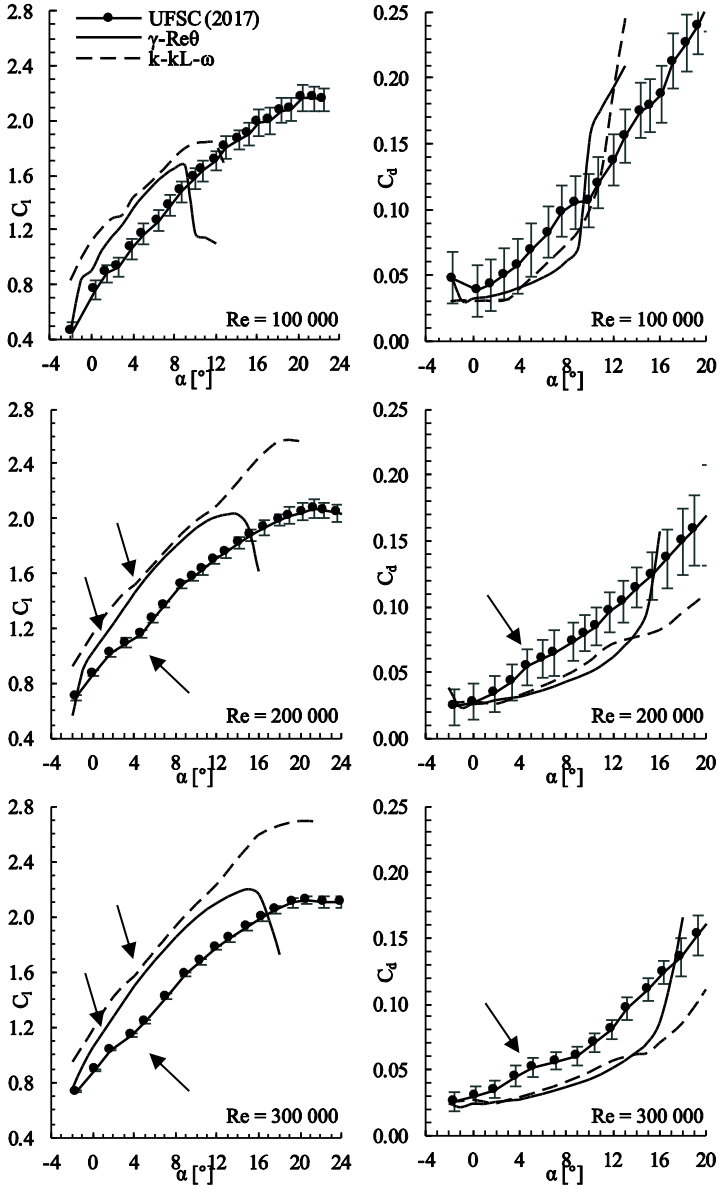

Figure 6.15 – Lift and drag coefficient from both numerical and experimental sources of the modified (leading edge wire) S1223.

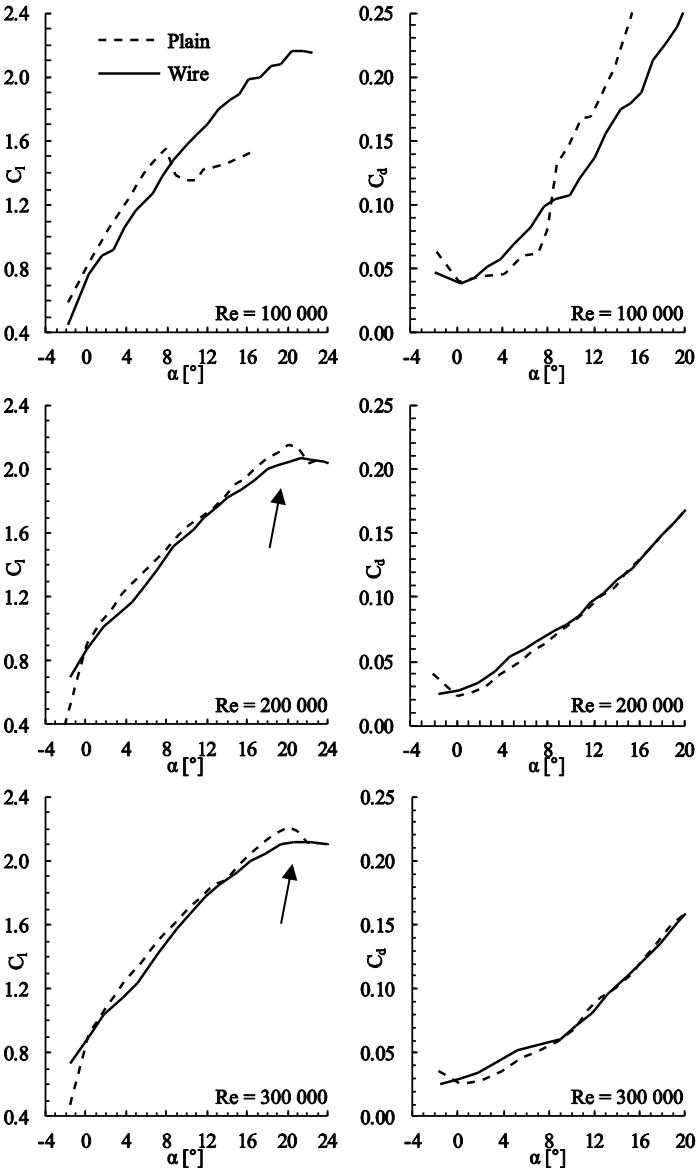

Figure 6.16 – Experimental lift and drag coefficients for the plain and modified (wire) S1223.

Figure 6.17 shows velocity contours for both configuration at α = -2°. For the γ-Re_θ, the device worsened airfoil performance due to the separated flow on the pressure surface, but the same effect was not observed on the k-k_L-ω model, where it actually eliminated the LSB and reduced drag.

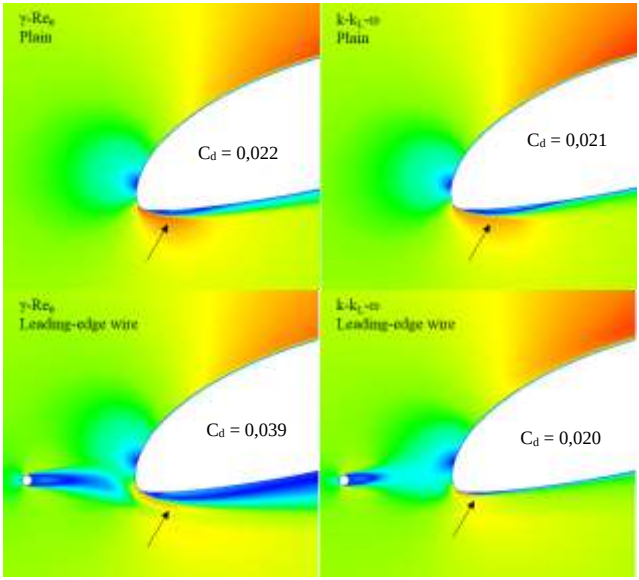

Figure 6.17 – Velocity contours of both configuration at α = -2°. (Re = $2 \cdot 10^5$)

Figure 6.18 shows the pressure distribution of the wing with leading-edge wire for Reynolds number of $1 \cdot 10^5$ and $2 \cdot 10^5$ and Figure 6.19 for Reynolds number of $3 \cdot 10^5$.

As seen in Figure 6.18 at Re = $1 \cdot 10^5$, the experimental points obtained a good agreement with the numerical C_p curves at angles of attack up to 8°. At α = 12°, the difference in C_p values reinforced the fact that numerical models were unable to predict stall properly.

At α = 0°, all methods were successful in not predicting the formation of a laminar separation since no hump on the C_p curve was detected for all Reynolds numbers. At α = 4° however, though computational models did predict a hump on the C_p curve, wind tunnel data did not. This suggests that turbulence generated by the wire, on the transition-sensitive models, was not strong enough to suppress the LSB, when in fact, experimental data show the opposite. In addition, it should be kept

in mind the turbulence in the wind tunnel was unknown and may impact the results.

Increasing the angle of attack to 8°, it is seen again that numerical simulations predicted the LSB while the experiment did not, except for $Re = 1 \cdot 10^5$. At this Reynolds, the wind tunnel achieved a good match with the γ-Re_θ model. At $\alpha = 12°$ and $Re = 2 \cdot 10^5$ and $3 \cdot 10^5$, the laminar separation bubble appears to be damped and did not match with the numerical curves.

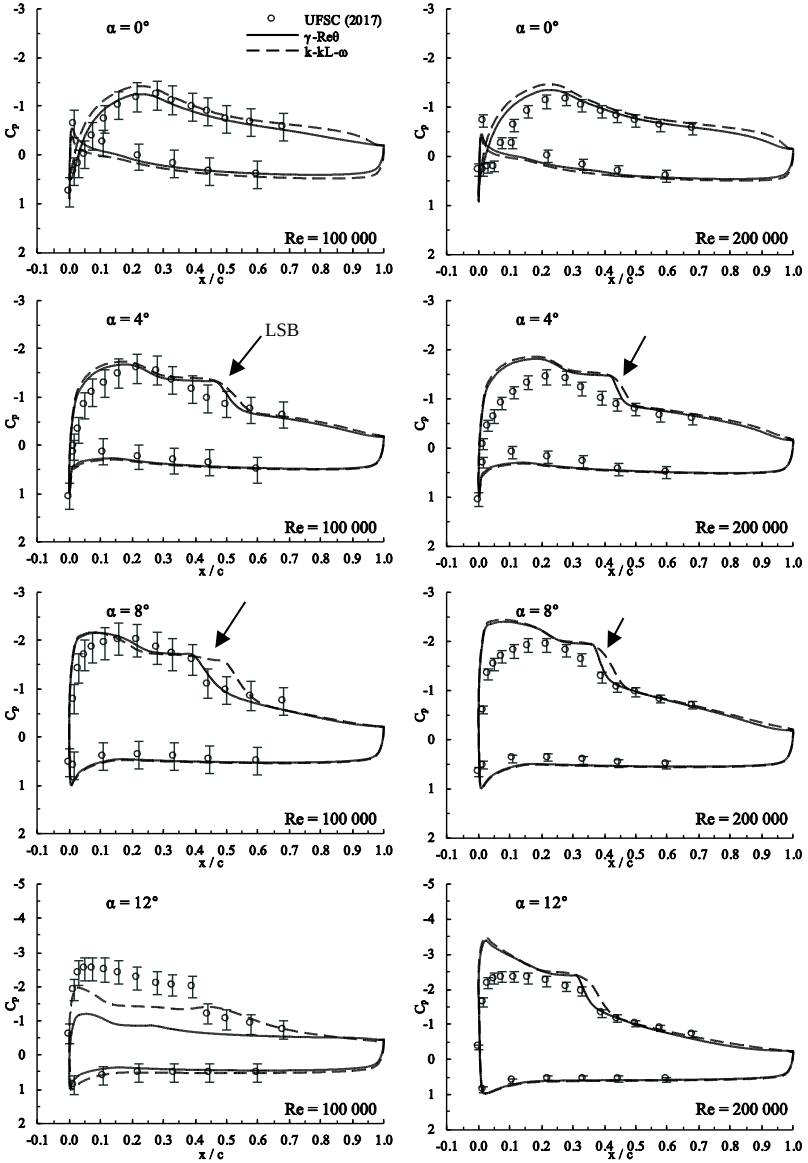

Figure 6.18 – Numerical and experimental C_p values for the S1223 with leading edge wire. (Re = $1 \cdot 10^5$ and Re = $2 \cdot 10^5$)

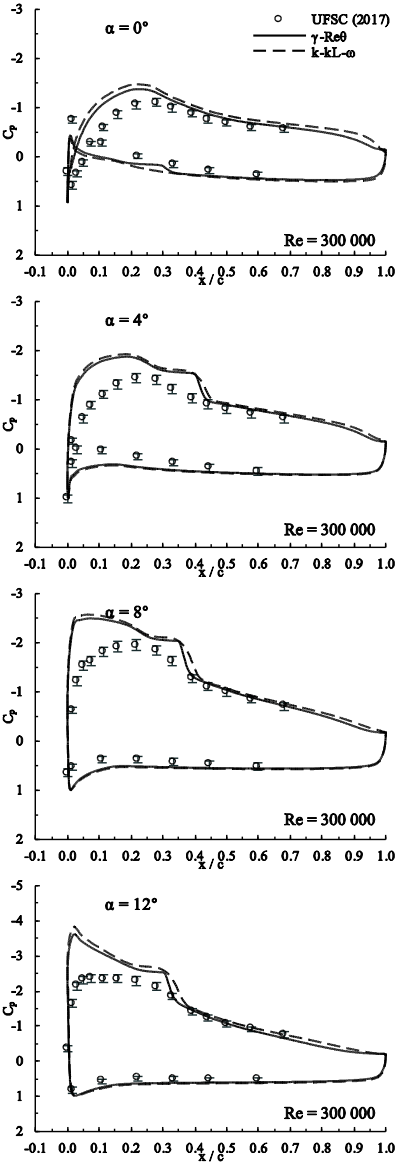

Figure 6.19 – Numerical and experimental C_p values for the S1223 with leading edge wire. ($Re = 3 \cdot 10^5$)

In order to understand how the leading-edge wire acts on the air-foil, oil flow visualization technique was applied in both cases (plain and

wire). Figure 6.20, Figure 6.21 and Figure 6.22 show this comparison for angles of attack of 4°, 8° and 12°, respectively. The dense area of pigment shows where the flow has decelerated, which indicates the laminar separation bubble. Looking at all three angles of attack, it is clear that as the Reynold number increases the bubble length shrinks.

In Figure 6.20 ($\alpha = 4°$), it is evident that the LSB was completely eliminated at $Re = 2 \cdot 10^5$ and $Re = 3 \cdot 10^5$ since no oil accumulation was detected. At $Re = 1 \cdot 10^5$, a denser area of pigment can be seen but not as visible as on the plain airfoil. This may indicate that the bubble still exists but has suffered from the turbulent flow generated by the wire.

Moving to $\alpha = 8°$ (Figure 6.21), the leading-edge wire loses its effectivity since the bubble could not be eliminated, however, bubble length has shortened. The leading-edge device seems to have more impact at low Reynolds numbers given the fact that bubble length presented a larger decrease only at $Re = 1 \cdot 10^5$.

Finally, at $\alpha = 12°$ (Figure 6.22), though laminar separation bubbles can still be seen on the wired configurations, the device prevented the flow to separate the surface at $Re = 1 \cdot 10^5$. At this Reynolds number, the plain version reported only a separation line but no reattachment. The other Reynolds numbers presented similar results to $\alpha = 8°$, but with the LSB shifted towards leading edge.

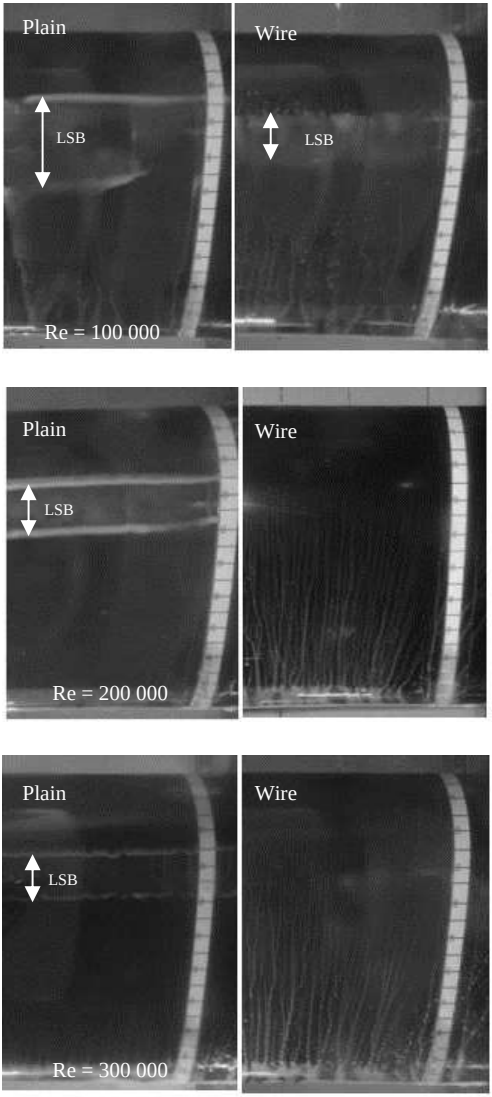

Figure 6.20 – Oil flow visualization of plain and modified S1223 at different Reynolds numbers. ($\alpha = 4°$)

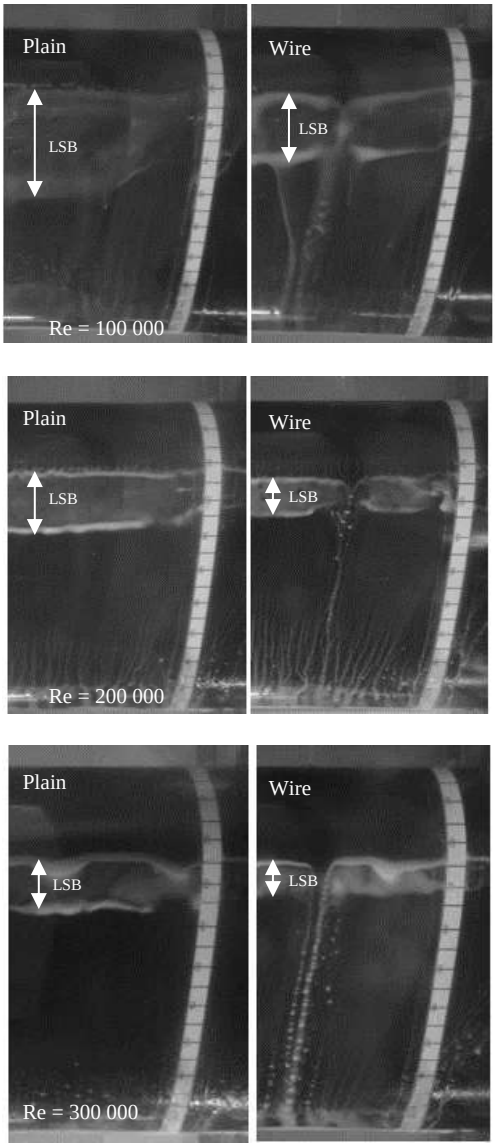

Figure 6.21 – Oil flow visualization of plain and modified S1223 at different Reynolds numbers. ($\alpha = 8°$)

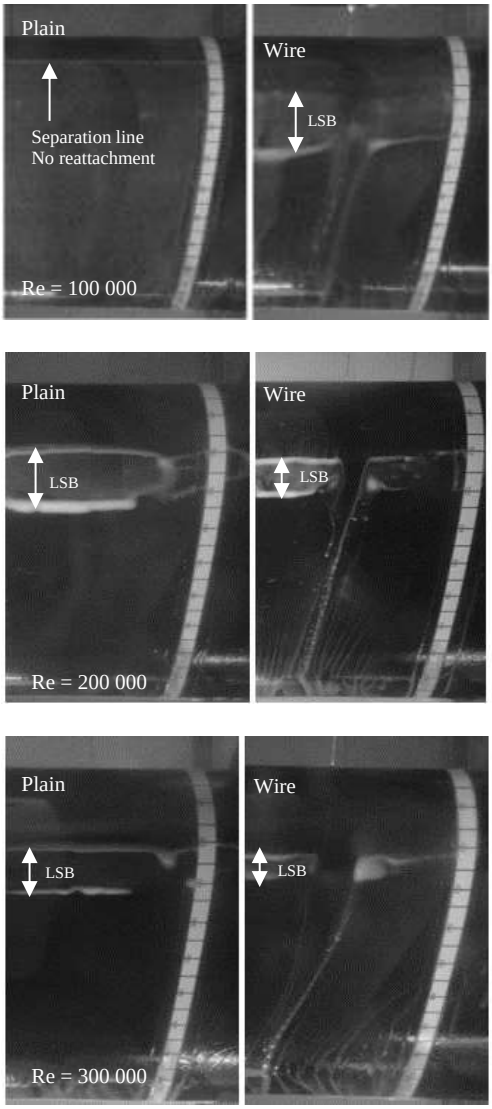

Figure 6.22 – Oil flow visualization of plain modified S1223 at different Reynolds numbers. ($\alpha = 12°$)

To complete the analysis, the measured locations of the laminar separation and turbulent reattachment lines are given in Figure 6.23. The error bars have been suppressed but it should be stated that the error did

not exceed ±0,04 chord length. Missing points indicated that either separation or reattachment could not be visualized.

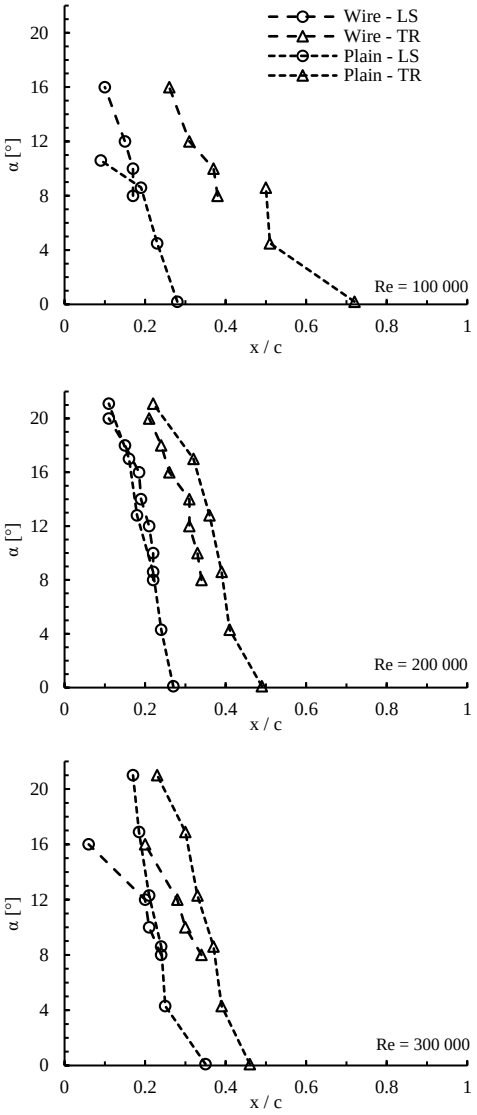

Figure 6.23 – Experimental comparison of the major flow features for both configurations at different Reynolds numbers. (LS – Laminar Separation, TR – Turbulent Reattachment)

Figure 6.23 reveals that the leading-edge device impacts differently the airfoil depending on the Reynolds number. At Re = $1 \cdot 10^5$, the device prevented stall at $\alpha = 11°$ and allowed airfoil to achieve higher angles of attack accompanied with the bubble. At Re = $2 \cdot 10^5$, bubble length decreased and separation line was slightly delayed. Finally, for a Reynolds number of $3 \cdot 10^5$, the bubble length also shrank, but for $\alpha > 12°$, the bubble suddenly moved towards the leading edge of the airfoil. It should be mentioned that the absence of points for angles higher than 16° does not indicate stall, but it may indicate that flow was completely turbulent since it did not leave any pattern on the oil.

7 CONCLUSIONS

7.1 General Remarks

The main goal of this research was to analyze the impact of laminar separation bubbles in airfoil performance using both numerical and experimental methods, as well as, to study the effect of placement of a leading-edge device to avoid or reduce the formation of laminar boundary layer separation bubble.

In the numerical analysis, the performance of transition-sensitive and fully-turbulent models was evaluated for predicting low Reynolds number flows including LSB. Freestream cases were first performed for the Eppler 387 airfoil at two Reynolds numbers. Transition-sensitive models (γ-Re_θ and k-k_L-ω) successfully predicted the LSB and obtained best agreement with drag data, due to the fact that laminar boundary layer exerts less friction to airfoil surface. The effect of increasing the Reynolds number from $2 \cdot 10^5$ to $3 \cdot 10^5$ decreases the bubble size, which in turn decreases pressure drag. For the Eppler 387, the γ-Re_θ revealed the best agreement with the experimental lift, drag and pressure data from LTPT (MCGHEE *et al.*, 1988). The bubble length predicted by this model also showed better match to the experiments than the k-k_L-ω model.

Switching to the S1223 airfoil, again the γ-Re_θ model provided the best results. At $Re = 3 \cdot 10^5$, it accurately predicted the angle of stall. For the pressure distribution, the γ-Re_θ model predicted smaller LSB than the k-k_L-ω did, and the fully-turbulent models could not predict the bubbles. It seems that the transition process takes longer to occur in the k-k_L-ω model, resulting in larger bubble length. Since the bubble size affects the flow downstream of its location, stall behavior can be affected. This characteristic may explain the difference in the angle of stall predicted by the models. By simulating this airfoil at $Re = 1 \cdot 10^5$, the premature stall indicates that this Reynolds number has achieved a critical value for the S1223.

Then, both airfoils were simulated in a wind tunnel domain, in order to analyze the influence of the tunnel walls over the measured quantities. As expected, the measured lift, drag and pressure in these cases were more accentuated than the freestream ones. Nevertheless, the use of the boundary correlations pushed the uncorrected values to match the freestream data. The relative errors drastically reduced in both airfoil cases, meaning that the correlations are suitable for this application and should be used in wind tunnels.

The S1223 wing was manufactured and tested in a wind tunnel. Tests occurred at Reynolds numbers of $1 \cdot 10^5$, $2 \cdot 10^5$ and $3 \cdot 10^5$ and showed that the value of $1 \cdot 10^5$ is critical for this wing. Corrected and uncorrected values were compared to the data provided by the UIUC (SELIG *et al.* 1995). In general, lift values were lower and drag values were higher than the reference. These discrepancies may have occurred due to errors in model geometry during the manufacturing process. In addition, the impossibility to measure the wind tunnel turbulent intensity may have affected, since this has great influence over the airfoil flow.

The pressure distributions measured on the wing revealed the presence of LSB. Depending on the angle of attack and Reynolds number, the C_p points demonstrated good agreement with both transition models. However, as the angle increased, the experiments could not reproduce the negative pressure spike predicted by all turbulence models near the leading edge. The difficulty to reproduce the exact leading edge geometry in a wind tunnel model may have been the cause of these discrepancies. Regarding bubble length and location, the experiments showed better agreement with the γ-Re_θ model at angles lower than 12°.

The addition of a leading-edge wire on the wing did not show any benefits at $Re = 2 \cdot 10^5$ and $3 \cdot 10^5$, but made a big difference at $Re = 1 \cdot 10^5$. The angle of stall increased from 8° to 20°. By analyzing C_p graphs, the characteristic hump present on the C_p curve was diminished, indicating that bubble formation was affected. This result was confirmed in the oil visualization analysis. At low angles of attack, the bubble was completely suppressed. At higher angles, the bubble was not eliminated but had its size reduced.

Overall, the main objective of this work is considered achieved. A complete numerical and experimental analysis of laminar separation bubbles in airfoils was given. Results demonstrated agreement with the references and the major error source is attributed to model imperfections and the impossibility of measuring the freestream turbulence intensity in the wind tunnel.

7.2 Future Work

The following is suggested for future work:

- Rebuild the wing model using a more accurate manufacturing process. Then, it is recommended to measure the shape of the model using an accurate process such as an optical measurement system, in order to assess the reproduction of the desired airfoil shape.

- To perform a 3D numerical simulation accounting for the wind tunnel side wall. That would provide an evaluation of the effects of the side walls on the measurements. The author believes that these walls affect the effective area of the wing, especially in high-lift airfoils, where pressure difference from the lower to the upper region of the wing is larger.
- To build other wing tunnel models with pressure tapping holes using different airfoils. The evaluation of the pressure distribution over the wing is an essential part to analyze their features.
- To perform detailed measurements of flow velocity near laminar separation bubble in order to verify the accuracy of the numerical models in prediction of the separation and reattachment points. This could be achieved with Laser Doppler Velocimetry – LDV and Particle Image Velocimetry – PIV methods. Thus, velocity profiles within the bubble could be obtained and used to validate the numerical models.
- To assess the effects of other methods to suppress the formation and effects of the laminar separation bubbles, such as the use of active surfaces and reconfigurable wings.

REFERENCES

ABBOTT, I. H.; DOENHOFF, A. E. **Theory of Wing Sections**. Dover Publications, Inc., New York, 1959.

ANDERSON, J. D. **Fundamentals of Aerodynamics**. Third Edition, McGraw-Hill, 2001.

BARLOW, J. B.; RAE, W. H.; POPE, A. **Low-Speed Wind Tunnel Testing**. John Wiley & Sons. New York. 1999.

COLEMAN, G. N.; SANDBERG, R. D. **A Primer on Direct Numerical Simulation of Turbulence – Methods, Procedures and Guidelines**. University of South Hampton. South Hampton, pp. 21, 2010.

DAVIDSON, P. A. **Turbulence: An Introduction for Scientists and Engineers**. Oxford University Press, New York, 2004.

GAD-EL-HAK, M. Micro-Air-Vehicles: Can They be Controlled Better?. **J. of Aircraft**, v. 38, n. 3, pp. 419-429, May 2001.

GENÇ, M. S.; KARASU, I.; AÇIKEL, H. H. An experimental study on aerodynamics of NACA 2415 aerofoil at low Re numbers. **Experimental Thermal and Fluid Science** 39, pp. 252-264, 2012.

GENÇ, M. S.; KAYNAK, U.; YAPICI, H. Performance of transition model for predicting low *Re* aerofoil flows without/with single and simultaneous blowing and suction. **European Journal of Mechanics B/Fluids** 30, pp. 218-235, 2011.

GHASEMI, E. et al. Effects of adverse and favorable pressure gradients on entropy generation in a transitional boundary layer region under the influence of freestream turbulence. **International Journal of Heat and Mass Transfer**, v. 77, pp. 475-488, October 2014.

GENÇ, M. S. **Low Reynolds Number Aerodynamics and Transition**. [S.l.]: InTech Europe, 2012.

HÜBBE, G. B. B. **Analysis of Fixed Slot in a NACA Profile at Low Reynolds Number**. Trabalho de Curso, Universidade Federal de Santa Catarina. Florianópolis. 2014.

JONES, A. R.; BAKHTIAN, N. M.; BABINSKY H. **Low Reynolds Number Aerodynamics of Leading Edge Flaps**. University of Cambridge. Cambridge. 2007.

KAYNAK, Ü.; ÇAKMAKÇIOGLU, S.; GENÇ, M. S. Transition at Low-Re Numbers for some Airfoils at High Subsonic Mach Numbers. In:

LANGTRY, R. B. **A Correlation-Based Transition Model using Local Variables for Unstructured Parallelized CFD codes**. Doctor Thesis - University of Stuttgart. [S.l.], 2006.

LOUREIRO, J.; RANGARAJAN, R.; TOVAR, E. **XDense: A Dense Grid Sensor Network for Distributed Feature Extraction**. XXXIII Simpósio Brasileiro de Redes de Computadores e Sistemas Distribuídos. April 2015.

MALISKA, C. R. **Transferência de Calor e Mecânica dos Fluidos Computacional**. 2nd ed. [S.l.]: LTC, 2004.

MALKIEL, E.; MAYLE, R. E. Transition in a Separation. **J. Turbomach**, 118, pp. 752-759. October 1996.

MASKELL, E. C. **A Theory of the Blockage Effects on Bluff Bodies and Stalled Wings in a Closed Wind Tunnel**. Aeronautical Research Council. London. November 1965.

MAYLE, R. E. The Role of Laminar-Turbulent Transition in Gas Turbine Engines. **J. Turbomach**, 113, pp. 509-536. October 1991.

MAYLE, R. E.; SCHULZ, A. The Path to Predicting Bypass Transition. **J. Turbomach**, 119, pp. 405-411. July 1997.

MCGHEE, R. J.; WALKER, B. S.; MILLARD, B. F. **Experimental Results for the Eppler 387 Airfoil at Low Reynolds Numbers in the Langley Low-Turbulence Pressure Tunnel**. Langley Research Center, Hampton, Virginia, 1988.

MCMASTERS, J. H.; HENDERSON, M. L. **Low Speed Single Element Airfoil Synthesis**. Technical Soaring, v. 6, pp. 1-21, 1980.

MENTER, F. R. **Two-Equation Eddy-Viscosity Turbulence Models for Engineering Applications**. AIAA Journal, v. 32, n. 8, pp. 1598-1605, August 1994.

MENTER, F. R.; KUNTZ, M.; LANGTRY, R. **Ten Years of Industrial Experience with the SST Turbulence Model**. In: HARJALIC, K.; NAGANO, Y.; TIMMERS, M. Turbulence, Heat and Mass Transfer: Begell House, 2003.

NASA. 2D NACA 0012 Airfoil Validation Case. **NASA Langley Research Center**, 2014.

PIOMELLI, U. Large-eddy simulation: achievements and challenges. **Progress in Aerospace Sciences**, 35, n. 4, May 1999.

POPE, S. B. **Turbulent Flows**. illustrated. ed.: Cambridge University Press, 2000.

RICCI, R.; MONTELPARE, S. A. Qualitative IR thermographic method to study the laminar separation bubble phenomenon. **International Journal of Thermal Science.** v. 44, pp. 709-719, 2005.

ROSKAM, J.; LAN, C. E. **Airplane Aerodynamics and Performance**. DAR corporation, Kansas, USA, 1997. ISBN: 1-884885-44-6.

SCHLICHTING, H.; GERSTEN, K. **Boundary-Layer Theory**. Ninth Edition, Springer-Verlag, Berlin, 2017. ISBN: 978-3-52919-5.

SCHUMANN, U. **A Procedure for the Direct Numerical Simulation of Turbulent Flows in Plate and Annular Channels and its Application in the Development of Turbulence Models**. NASA. Washington, pp. 321. 1974.

SELIG, M.S. **Low Reynolds Number Airfoil Design Lecture Notes**. VKI Lecture Series, November 2003.

SELIG, M. S. et al. **Summary of Low-Speed Airfoil Data**. Virginia Beach: SoarTech Publications, v. 1, 1995.

SELIG, M. S.; MCGRANAHAN, B. D. **Wind Tunnel Aerodynamic Tests of Six Airfoils for Use on Small Wind Turbines**. National Renewable Energy Laboratory. Golden. 2004.

SILVA FREIRE, A. P.; MENUT, P. P. M.; SU, J. **Turbulência:** Anais da I Escola de Primavera em Transição e Turbulência. Rio de Janeiro: ABCM, v. 1, 292 p. 1998.

SPALART, P. R.; ALLMARAS, S. R. **A one-equation turbulence model for aerodynamic flows**. AIAA 30th Aerospace Sciences Meeting and Exhibit, Nevada, 1992.

SPALART, P. R.; RUMSEY, C. L. Effective Inflow Conditions for Turbulence Models in Aerodynamic Calculations. **AIAA Journal**, v. 45, n. 10, pp. 2544-2553, October 2007.

TAIN, L.; CUMPSTY, N. A. Compressor Blade Leading Edges in Subsonic Compressible Flow. **J. Mech Eng Science**, v. 214, pp. 221-242. 2000.

THOM, A. **Blockage Corrections in a High Speed Wind Tunnel**. Aeronautical Research Council. London. 1943.

WALRAEVENS, R. E.; CUMPSTY, W. A. Leading Edge Separation Bubbles on Turbomachine Blades. **J. Turbomach**. 125, pp. 115-125. January 1995.

WALTERS, D. K.; COKLJAT, D. A Three-Equation Eddy-Viscosity Model for Reynolds-Averaged Navier-Stokes Simulations of Transitional Flow, **J. Fluids Eng** 130(12). October 2008.

WALTERS, D. K.; LEYLEK, J. H. A new model for boundary layer transition using a single-point RANS approach, **J. Turbomach**. 126 pp. 193-202. 2004.

WERNECK, D. A. **Estudo Experimental sobre o Uso de Geradores de Vórtices em um Perfil Aerodinâmico de Alta Sustentação em Baixo Número de Reynolds**. Trabalho de Curso. Universidade Federal de Santa Catarina. Florianópolis. 2014.

WHITE, F. M. **Viscous Fluid Flow**. Third Edition. Singapore: McGraw-Hill, 2005. ISBN: 978-0072402315.

WILCOX, D. C. **Turbulence Modeling for CFD**. 3rd. ed.: D C W Industries, 2006.

APPENDIX A – UNCERTAINTY ANALYSIS

This section presents an analysis of the uncertainty of the measurements performed. It was based on the method presented by Albertazzi and Sousa (2008).

The standard uncertainty, or standard deviation, of a sample is the intensity of the random component of a measurement:

$$u(x) = \sqrt{\sum_{i=1}^{n} \frac{(x_i - \bar{x})^2}{n-1}} \tag{A.1}$$

where $u(x)$ is the standard uncertainty, n is number of data, x_i is ith datum of a sample, and $\bar{x}$ is the average of the data sample.

The relative uncertainty is the ratio between the standard uncertainty and the average of the data:

$$u_r(x) = \frac{u(x)}{\bar{x}} \tag{A.2}$$

When the uncertainty of a result is obtained from a combination of uncertainties measured separately, it is called combined uncertainty. If the uncertainties are not correlated to each other, the combined uncertainty can be calculated as

$$u_c^2(Y) = \sum_{i=1}^{N} \left(\frac{\partial Y}{\partial X_i}\right)^2 u^2(X_i) \tag{A.3}$$

where X_i are the input quantities which will result in Y.

The expanded uncertainty is given by

$$U(x) = k \cdot u_c(x) \tag{A.4}$$

where k is the coverage factor and usually assumes a value of 2 for a confidence level of 95 %.

Finally, the final result of a measurement can be given as follows:

$$x = \bar{x} \pm U(x) \tag{A.5}$$

An example of the calculation of the uncertainties for $C_p = \frac{p-p_\infty}{1/2\rho V^2}$ is shown below. By using Eq. (A.3), it can be shown that

$$u_c^2(C_p) = \left(\frac{1}{\frac{1}{2}\rho V^2}\right)^2 u^2(p) + \left(\frac{-1}{\frac{1}{2}\rho V^2}\right)^2 u^2(p_\infty) + \left(\frac{-(p-p_\infty)}{\frac{1}{2}\rho^2 V^2}\right)^2 u^2(\rho) + \left(\frac{4(p-p_\infty)}{\rho V^3}\right)^2 u^2(V)$$

Table A.1 – Example of values and their uncertainties to calculate the pressure coefficient.

Quantity	**Standard Uncertainty**	$\frac{\partial Y}{\partial X}\boldsymbol{u(X)}$
$\bar{p} = -120\ Pa$	$u(p) = 4\ Pa$	0,038
$\bar{p}_\infty = -2\ Pa$	$u(p_\infty) = 3\ Pa$	0,028
$\bar{\rho} = 1{,}165\ kg/m^3$	$u(\rho) = 0{,}02\ kg/m^3$	0,019
$\bar{V} = 13{,}4\ m/s$	$u(V) = 0{,}4\ m/s$	0,067

Using Eqs. (A.3), (A.4) and (A.5), and the values presented in Table A.1, it can be shown that

$$C_p = -1{,}13 \pm 0{,}17$$

The same process was used to calculate the combined uncertainties for the lift and drag coefficients.

APPENDIX B – EXPERIMENTAL DATA

This section presents the experimental data obtained in the wind tunnel.

B.1 – Pressure Coefficient

Table B.2 – C_p for the S1223 clean. ($Re = 1 \cdot 10^5$)

	x / c	α = 0°	α = 2°	α = 4°	α = 6°	α = 8°	α = 10°
Pressure Surface	0.60	0.42	0.46	0.51	0.51	0.52	0.42
	0.44	0.33	0.41	0.31	0.47	0.48	0.41
	0.33	0.26	0.17	0.29	0.36	0.44	0.32
	0.22	0.05	0.07	0.23	0.30	0.38	0.29
	0.11	-0.31	-0.10	0.10	0.27	0.37	0.26
	0.02	-0.79	-0.46	-0.02	0.32	0.49	0.33
Suction Surface	0.00	0.88	1.06	1.08	0.99	0.86	0.99
	0.02	0.45	0.59	0.22	-0.17	-0.42	-0.09
	0.03	0.09	-0.19	-0.37	-1.00	-1.17	-0.45
	0.05	-0.16	-0.52	-0.90	-1.26	-1.42	-0.97
	0.07	-0.53	-0.86	-1.19	-1.49	-1.64	-1.08
	0.11	-0.80	-1.11	-1.41	-1.65	-1.69	-1.09
	0.16	-1.07	-1.33	-1.56	-1.79	-1.74	-0.89
	0.22	-1.26	-1.48	-1.64	-1.76	-1.51	-0.83
	0.28	-1.28	-1.45	-1.53	-1.57	-1.41	-0.82
	0.33	-1.14	-1.30	-1.37	-1.50	-1.41	-0.84
	0.39	-1.02	-1.18	-1.33	-1.45	-1.41	-0.85
	0.44	-0.96	-1.14	-1.30	-1.50	-1.44	-0.87
	0.50	-0.90	-1.10	-1.22	-1.27	-1.27	-0.89
	0.58	-0.77	-0.86	-0.89	-0.91	-0.97	-0.87
	0.68	-0.65	-0.67	-0.69	-0.70	-0.73	-0.88

Table B.3 – C_p for the S1223 clean. ($Re = 2 \cdot 10^5$)

	x / c	α = 0°	α = 2°	α = 4°	α = 6°	α = 8°	α = 10°	α = 12°	α = 14°	α = 16°
Pressure Surface	0.60	0.43	0.47	0.54	0.52	0.53	0.54	0.59	0.51	0.54
	0.44	0.34	0.39	0.47	0.45	0.50	0.51	0.59	0.52	0.57
	0.33	0.21	0.28	0.35	0.39	0.44	0.48	0.55	0.51	0.56
	0.22	0.05	0.11	0.28	0.32	0.41	0.46	0.56	0.54	0.59
	0.11	-0.18	-0.06	0.17	0.27	0.42	0.51	0.66	0.65	0.74
	0.02	-0.88	-0.40	0.09	0.32	0.58	0.73	0.93	0.92	0.96
Suction Surface	0.00	0.83	0.99	1.07	0.90	0.60	0.18	-0.39	-1.23	-2.04
	0.02	0.39	0.55	0.24	-0.18	-1.03	-1.18	-1.70	-2.36	-2.95
	0.03	0.09	-0.11	-0.42	-0.99	-1.46	-1.81	-2.22	-2.77	-3.19
	0.05	-0.12	-0.45	-0.79	-1.21	-1.66	-1.98	-2.40	-2.90	-3.24
	0.07	-0.47	-0.76	-1.07	-1.39	-1.80	-2.09	-2.43	-2.83	-3.13
	0.11	-0.73	-1.00	-1.27	-1.58	-1.90	-2.11	-2.42	-2.75	-2.93
	0.16	-0.98	-1.21	-1.47	-1.68	-1.98	-2.14	-2.38	-2.65	-2.78
	0.22	-1.17	-1.36	-1.52	-1.77	-1.95	-2.07	-2.25	-2.47	-2.57
	0.28	-1.19	-1.33	-1.47	-1.63	-1.81	-1.91	-2.12	-2.31	-2.48
	0.33	-1.07	-1.19	-1.33	-1.50	-1.69	-1.84	-2.10	-2.19	-1.99
	0.39	-0.95	-1.07	-1.23	-1.43	-1.65	-1.85	-1.51	-1.59	-1.56
	0.44	-0.85	-0.98	-1.10	-1.06	-1.05	-1.11	-1.21	-1.32	-1.32
	0.50	-0.75	-0.81	-0.79	-0.88	-0.96	-0.99	-1.03	-1.14	-1.14
	0.58	-0.66	-0.68	-0.69	-0.77	-0.84	-0.87	-0.89	-0.97	-0.96
	0.68	-0.57	-0.61	-0.61	-0.67	-0.71	-0.73	-0.73	-0.80	-0.78

Table B.4 – C_p for the S1223 clean. ($Re = 3 \cdot 10^5$)

	x / c	α = 0°	α = 2°	α = 4°	α = 6°	α = 8°	α = 10°	α = 12°	α = 14°	α = 16°
Pressure Surface	0.60	0.41	0.47	0.48	0.52	0.53	0.54	0.55	0.56	0.57
	0.44	0.32	0.39	0.42	0.47	0.49	0.52	0.54	0.56	0.58
	0.33	0.19	0.28	0.30	0.40	0.45	0.49	0.52	0.56	0.59
	0.22	0.03	0.14	0.22	0.34	0.41	0.47	0.52	0.58	0.62
	0.11	-0.22	-0.05	0.11	0.30	0.42	0.52	0.61	0.70	0.76
	0.02	-1.00	-0.40	-0.02	0.35	0.57	0.74	0.85	0.95	0.97
Suction Surface	0.00	0.74	0.97	1.00	0.88	0.56	0.08	-0.48	-1.40	-2.20
	0.02	0.85	0.59	0.23	-0.24	-0.71	-1.24	-1.74	-2.47	-2.93
	0.03	0.16	-0.08	-0.29	-0.55	-1.34	-1.93	-2.29	-2.83	-3.16
	0.05	-0.06	-0.40	-0.79	-1.25	-1.64	-2.06	-2.42	-2.93	-3.16
	0.07	-0.39	-0.71	-1.06	-1.46	-1.80	-2.15	-2.47	-2.86	-3.04
	0.11	-0.67	-0.96	-1.26	-1.62	-1.89	-2.18	-2.44	-2.78	-2.97
	0.16	-0.93	-1.19	-1.44	-1.74	-1.98	-2.22	-2.40	-2.69	-2.87
	0.22	-1.10	-1.34	-1.54	-1.81	-1.98	-2.17	-2.29	-2.57	-2.73
	0.28	-1.18	-1.33	-1.50	-1.71	-1.86	-2.02	-2.15	-2.39	-2.48
	0.33	-1.03	-1.18	-1.33	-1.54	-1.73	-1.91	-2.00	-1.91	-1.94
	0.39	-0.90	-1.05	-1.22	-1.43	-1.58	-1.38	-1.45	-1.55	-1.59
	0.44	-0.80	-0.95	-1.00	-1.01	-1.09	-1.18	-1.23	-1.31	-1.33
	0.50	-0.75	-0.80	-0.84	-0.92	-0.97	-1.04	-1.07	-1.13	-1.13
	0.58	-0.64	-0.68	-0.74	-0.80	-0.85	-0.89	-0.91	-0.94	-0.93
	0.68	-0.56	-0.61	-0.65	-0.70	-0.72	-0.74	-0.74	-0.75	-0.71

Table B.5 – C_p for the S1223 with leading-edge wire. ($Re = 1 \cdot 10^5$)

	x / c	α = 0°	α = 4°	α = 8°	α = 10°	α = 12°	α = 14°	α = 16°
Pressure Surface	0.60	0.42	0.51	0.50	0.53	0.53	0.54	0.57
	0.44	0.34	0.36	0.46	0.53	0.52	0.55	0.61
	0.33	0.19	0.32	0.42	0.49	0.52	0.56	0.63
	0.22	0.04	0.24	0.38	0.47	0.52	0.57	0.65
	0.11	-0.24	0.13	0.41	0.54	0.61	0.70	0.80
	0.02	-0.63	0.03	0.59	0.77	0.88	0.97	1.02
Suction Surface	0.00	0.76	1.06	0.53	0.08	-0.62	-1.41	-2.32
	0.02	0.35	0.16	-0.78	-1.26	-1.90	-2.52	-3.17
	0.03	0.18	-0.32	-1.42	-1.81	-2.39	-2.89	-3.39
	0.05	0.01	-0.82	-1.70	-2.06	-2.51	-2.95	-3.36
	0.07	-0.39	-1.09	-1.85	-2.15	-2.51	-2.86	-3.20
	0.11	-0.73	-1.28	-1.94	-2.18	-2.49	-2.74	-3.02
	0.16	-1.01	-1.49	-2.02	-2.19	-2.41	-2.61	-2.79
	0.22	-1.18	-1.59	-2.00	-2.11	-2.24	-2.42	-2.60
	0.28	-1.23	-1.54	-1.84	-1.93	-2.10	-2.28	-2.49
	0.33	-1.12	-1.34	-1.71	-1.84	-2.04	-2.26	-2.42
	0.39	-0.99	-1.16	-1.60	-1.82	-1.99	-1.74	-1.50
	0.44	-0.89	-0.97	-1.10	-1.14	-1.20	-1.22	-1.26
	0.50	-0.74	-0.84	-0.96	-0.96	-1.03	-1.07	-1.09
	0.58	-0.65	-0.73	-0.85	-0.85	-0.89	-0.92	-0.92
	0.68	-0.56	-0.62	-0.74	-0.72	-0.74	-0.75	-0.77

Table B.6 – C_p for the S1223 with leading-edge wire. ($Re = 2 \cdot 10^5$)

	x / c	α = 0°	α = 4°	α = 8°	α = 12°	α = 16°	α = 20°
Pressure Surface	0.60	0.40	0.50	0.51	0.57	0.54	0.53
	0.44	0.30	0.44	0.48	0.57	0.56	0.58
	0.33	0.18	0.29	0.42	0.54	0.57	0.60
	0.22	0.01	0.20	0.37	0.54	0.59	0.65
	0.11	-0.26	0.0 9	0.38	0.63	0.73	0.81
	0.02	-0.71	-0.07	0.53	0.89	0.97	0.95
Suction Surface	0.00	0.29	1.06	0.67	-0.34	-1.84	-3.56
	0.02	0.28	0.30	-0.60	-1.63	-2.78	-3.87
	0.03	0.23	-0.45	-1.33	-2.18	-3.17	-3.92
	0.05	0.21	-0.64	-1.52	-2.31	-3.09	-3.75
	0.07	-0.26	-0.91	-1.69	-2.34	-2.97	-3.49
	0.11	-0.62	-1.12	-1.80	-2.34	-2.84	-3.24
	0.16	-0.91	-1.32	-1.91	-2.32	-2.72	-3.02
	0.22	-1.11	-1.44	-1.93	-2.23	-2.56	-2.75
	0.28	-1.16	-1.41	-1.82	-2.08	-2.39	-2.34
	0.33	-1.03	-1.21	-1.62	-1.95	-1.87	-1.85
	0.39	-0.91	-1.01	-1.27	-1.31	-1.49	-1.49
	0.44	-0.81	-0.88	-1.07	-1.16	-1.27	-1.24
	0.50	-0.71	-0.78	-0.96	-1.02	-1.10	-1.05
	0.58	-0.61	-0.67	-0.83	-0.87	-0.93	-0.86
	0.68	-0.55	-0.58	-0.70	-0.72	-0.78	-0.72

Table B.7 – C_p for the S1223 with leading-edge wire. ($Re = 3 \cdot 10^5$)

	x / c	α = 0°	α = 4°	α = 8°	α = 12°	α = 16°	α = 20°
Pressure Surface	0.60	0.38	0.46	0.52	0.53	0.55	0.55
	0.44	0.28	0.39	0.48	0.53	0.57	0.59
	0.33	0.15	0.28	0.43	0.50	0.57	0.63
	0.22	-0.01	0.15	0.38	0.49	0.60	0.67
	0.11	-0.28	0.03	0.38	0.58	0.73	0.83
	0.02	-0.75	-0.16	0.53	0.83	0.97	0.96
Suction Surface	0.00	0.30	1.01	0.65	-0.36	-1.89	-3.59
	0.02	0.59	0.29	-0.62	-1.64	-2.78	-3.88
	0.03	0.34	0.01	-1.22	-2.14	-2.98	-3.79
	0.05	0.14	-0.62	-1.54	-2.31	-3.01	-3.68
	0.07	-0.26	-0.89	-1.62	-2.35	-2.89	-3.42
	0.11	-0.58	-1.10	-1.82	-2.35	-2.79	-3.19
	0.16	-0.86	-1.30	-1.91	-2.35	-2.76	-2.95
	0.22	-1.05	-1.43	-1.94	-2.28	-2.61	-2.75
	0.28	-1.11	-1.41	-1.84	-2.13	-2.38	-2.37
	0.33	-0.99	-1.21	-1.62	-1.85	-1.86	-1.88
	0.39	-0.87	-1.03	-1.27	-1.41	-1.53	-1.51
	0.44	-0.76	-0.90	-1.10	-1.22	-1.30	-1.24
	0.50	-0.68	-0.81	-0.99	-1.07	-1.12	-1.05
	0.58	-0.60	-0.70	-0.84	-0.91	-0.93	-0.85
	0.68	-0.55	-0.61	-0.71	-0.75	-0.75	-0.68

B.2 – Lift and Drag Coefficient

Table B.8 – Lift and drag coefficient for the S1223 clean.

$Re = 1 \cdot 10^5$			$Re = 2 \cdot 10^5$			$Re = 3 \cdot 10^5$		
α [°]	**C_l**	**C_d**	**α [°]**	**C_l**	**C_d**	**α [°]**	**C_l**	**C_d**
-1.7	0.59	0.063	-2.1	0.39	0.040	-1.7	0.48	0.037
0.2	0.83	0.040	0.1	0.90	0.023	0.3	0.92	0.025
2.3	1.06	0.044	1.4	1.04	0.027	2.1	1.09	0.028
4.1	1.23	0.045	2.4	1.12	0.031	3.8	1.25	0.036
5.9	1.41	0.060	3.7	1.22	0.039	5.5	1.36	0.045
7.1	1.49	0.061	5.4	1.33	0.050	7.2	1.50	0.052
8.0	1.55	0.080	6.7	1.41	0.058	8.9	1.61	0.059
8.7	1.39	0.132	7.8	1.50	0.064	10.3	1.72	0.069
9.7	1.35	0.146	9.0	1.58	0.072	11.3	1.77	0.083
10.9	1.35	0.167	10.2	1.65	0.080	12.5	1.84	0.093
11.7	1.42	0.169	11.2	1.70	0.088	13.9	1.89	0.100
12.6	1.43	0.184	12.6	1.76	0.100	15.2	1.98	0.112
13.9	1.46	0.209	13.8	1.82	0.108	16.6	2.06	0.127
15.1	1.50	0.244	14.9	1.90	0.119	17.4	2.10	0.136
16.3	1.53	0.274	15.8	1.94	0.128	18.6	2.16	0.149
			17.0	2.01	0.139	20.0	2.21	0.158
			18.0	2.07	0.149	21.0	2.18	0.170
			19.1	2.10	0.157	22.0	2.12	0.186
			20.1	2.15	0.169	23.0	2.10	0.190
			21.1	2.13	0.180			
			22.1	2.03	0.198			
			23.1	2.06	0.209			

Table B.9 – Lift and drag coefficient for the S1223 with leading-edge wire.

Re = 1·10^5			**Re = 2·10^5**			**Re = 3·10^5**		
α [°]	**C_l**	**C_d**	**α [°]**	**C_l**	**C_d**	**α [°]**	**C_l**	**C_d**
-1.8	0.45	0.048	-1.6	0.70	0.024	-1.6	0.74	0.026
0.3	0.76	0.038	0.1	0.87	0.028	0.2	0.89	0.030
1.5	0.88	0.043	1.8	1.02	0.034	1.8	1.04	0.035
2.7	0.93	0.051	3.3	1.10	0.043	3.7	1.14	0.045
3.9	1.06	0.057	4.6	1.16	0.054	5.2	1.24	0.052
5.0	1.17	0.069	5.9	1.27	0.060	7.1	1.42	0.057
6.5	1.27	0.083	7.0	1.37	0.065	9.0	1.58	0.060
7.6	1.38	0.098	8.7	1.52	0.074	10.4	1.68	0.071
8.7	1.48	0.105	9.6	1.57	0.079	11.9	1.78	0.081
10.0	1.58	0.107	10.7	1.63	0.085	13.2	1.84	0.097
10.8	1.63	0.120	11.7	1.70	0.096	15.0	1.93	0.111
12.1	1.71	0.137	12.9	1.75	0.104	16.4	2.00	0.124
13.0	1.80	0.156	14.1	1.83	0.114	17.8	2.05	0.135
14.3	1.85	0.175	15.4	1.87	0.123	19.3	2.11	0.152
15.1	1.90	0.179	16.7	1.93	0.136	20.7	2.12	0.166
16.2	1.98	0.188	18.0	2.00	0.149	22.3	2.11	0.198
17.2	2.00	0.212	19.0	2.02	0.158	24.0	2.11	0.222
18.3	2.07	0.227	20.2	2.05	0.170	25.3	2.14	0.242
19.3	2.08	0.239	21.3	2.07	0.183			
20.3	2.17	0.260	22.3	2.06	0.197			
21.5	2.16	0.278	23.7	2.04	0.209			
22.4	2.15	0.297	24.7	2.02	0.234			
			26.3	1.94	0.327			